Dissertation

submitted to the
Combined Faculties of the Natural Sciences and Mathematics
of the Ruperto-Carola-University of Heidelberg, Germany
for the degree of
Doctor of Natural Sciences

Put forward by

Hendrik Bekker MSc.

born in: Groningen, the Netherlands

Oral examination: 18-05-2016

Optical and EUV spectroscopy of highly charged ions near the $4f$–$5s$ level crossing

Referees: PD Dr. José R. Crespo López-Urrutia

PD Dr. Wolfgang Quint

Optical and EUV spectroscopy of highly charged ions near the $4f$–$5s$ level crossing

In recent years, various highly charged ions (HCI) with optical transitions have been proposed for metrology and searches of a possible variation of the fine-structure constant α. Optical transitions in HCI are uncommon due to the scaling of energy levels with atomic number Z^2. At the $4f$–$5s$ level crossing, three configurations are nearly degenerate, and thus many optical transitions can exist. The complex many-electron couplings reduce the accuracy of current calculations. Moreover, experimental data to benchmark the predictions is lacking. Spectra in the optical and extreme-ultraviolet (EUV) range of several ion species near the $4f$–$5s$ level crossing were measured at the Heidelberg electron beam ion trap. A collisional-radiative model was employed for the interpretation of the EUV data, resulting in the first identification of the long sought-after $5s$–$5p$ transitions in Pm-like Re^{14+}, Os^{15+}, Ir^{16+}, and Pt^{17+}. The characteristic line shapes of optical transitions in Ir^{17+} were studied, with the aim of identifying transitions with a high sensitivity to α-variation. Previously suggested candidates could be excluded and new candidates were proposed. This data provides a stringent benchmark for state-of-the-art precision atomic theory.

Optische und EUV Spektroskopie hochgeladener Ionen in der Umgebung der $4f$–$5s$-Niveaukreuzung

In den letzten Jahren wurden verschiedene hochgeladene Ionen (HCI) mit optischen Übergängen sowohl für die Metrologie als auch für die Suche nach einer möglichen Zeitabhängigkeit der Feinstrukturkonstanten α vorgeschlagen. Solche Übergänge treten wegen der Skalierung der Energienniveaus mit der Atomzahl Z^2 bei HCI selten auf. Jedoch sind bei der $4f$–$5s$ Kreuzung drei unterschiedliche elektronische Konfigurationen energetisch nahezu entartet, wodurch eine Vielzahl optischer Übergänge zwischen ihnen stattfinden kann. Die komplexen Kopplungen der Elektronen vermindern die Genauigkeit aktueller Stukturrechnungen. Zudem existieren kaum experimentelle Daten, um jene zu überprüfen. Es wurden Spektren sowohl im optischen als auch im extremen-ultravioletten (EUV) Bereich mittels der Heidelberger Electron Beam Ion Trap aufgenommen. Mit Hilfe eines kollisionellen-radiativen Modells wurden die EUV-Daten analysiert, wobei die erste Identifizierung der langgesuchten Übergänge $5s$–$5p$ in Pm-artigen Re^{14+}, Os^{15+}, Ir^{16+} und Pt^{17+} gelang. Die charakteristischen Linienprofile der optischen Übergänge in Ir^{17+} wurden zur Identifizierung von Linien mit hoher Empfindlichkeit für eine α-Variation untersucht. Es konnten dabei frühere Vorschläge ausgeschlossen und neue Kandidaten ausgemacht werden. Die gewonnenen Daten stellen akkurate Prüfsteine für moderne Präzisionsrechnungen der Atomtheorie dar.

Table of contents

Chapter 1

Introduction and motivation

Ceaseless change is the only constant thing in nature.

John Candee Dean [1]

Since the dawn of our existence humankind has developed increasingly intricate models to understand, explain, and control nature. And yet, with every advancement in our understanding, new questions arise. At the forefront of our current understanding of particle physics is the Standard Model. It describes the properties and the possible interactions of 17 fundamental particles, refer to Fig. 1.1 for a schematic overview. Over the years, minor adjustments had to be made to the Standard Model, most prominently the addition of the Higgs boson [2, 3]. Nonetheless, the Standard Model has proven to be highly successful at predicting and describing nature [4]. Despite these successes, there are questions that the Standard Model provokes. One of these questions has to do with the way fundamental particles interact with each other. Mathematically this is fully described in the Standard Model. Determining for the actual strengths of the interactions are the coupling constants. These, together with the masses of the fundamental particles, form approximately 20 free parameters of the Standard Model. Their actual values have been found by measurements. However, one can ask: why do they have the values they have? Could these be predicted from first principles? And also, are the constants truly constant in time? After all, if there is anything that our observations of the universe have taught us, it is that change is ceaseless.

The possibility of varying constants was already considered by notable physicists such as Dirac, Teller, and Gamow [5–7]. The original idea of Dirac that the gravitational constant varies with time was disproved by Teller and Gamov. However, the latter suggested that the fine-structure constant could vary with time. Till this day, the possible variation of constants remains a widely discussed topic in physics. For example, many current theories beyond the Standard Model introduce extra spatial dimensions in addition to the three familiar ones. The

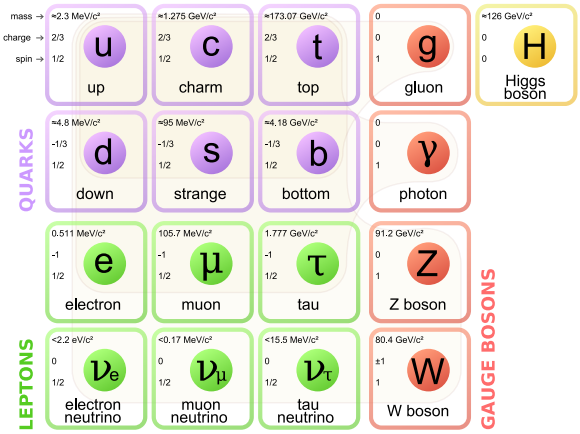

Fig. 1.1 Illustration of the fundamental particles and their classification in the Standard Model [11].

true constants of nature are then part of the higher dimensional space, and we observe mere projections of those true ones. Any changes in the scales of the additional dimensions can subsequently cause a variation of the constants we observe [8–10].

1.1 Searches for variation of fundamental constants

Current searches for variations of constants mainly focus on the dimensionless values of both the fine-structure constant α and the proton-to-electron mass ratio $\mu = m_p/m_e$. Both constants can be probed using techniques from experimental atomic physics. These techniques have been refined over decades, and are currently employed in some of the most precise measurements and tests of Standard Model physics. This work concerns, among other subjects, a system with a high sensitivity to the variation of α. This constant determines the coupling strength between electrically charged particles and the electromagnetic field, the most important interaction in atoms. Sommerfeld introduced α to explain the fine structure of spectral lines that had been observed for hydrogen [12]. In modern quantum mechanics, it is defined through a combination of several physical constants as

$$\begin{aligned} \alpha &= \frac{e^2}{4\pi\varepsilon_0\hbar c} \\ &= 7.2973525664(17)\cdot 10^{-3}. \end{aligned} \tag{1.1}$$

Here, e is the elementary charge, ε_0 the permittivity of free space, $\hbar$ the reduced Planck constant, and c the speed of light in vacuum. The second line shows the numerical value as

recommended by CODATA [13]. Two methods to determine the variation of α are discussed next.

The first method exploits techniques and advances from the science of measurement, i.e. metrology. Current state of the art frequency standards developed at metrology institutes such as NIST[1], NPL[2], and the PTB[3] reach extremely small fractional uncertainties, the current record being at the level of 10^{-18} [14–16]. The unprecedented precision achieved by these can be used to determine upper limits for the variations of α and μ. In a modern frequency standard (clock), a laser is locked to an optical transition of an ion. Simultaneously, the frequency ν of the laser light can be compared to another clock, for example by means of a frequency comb. Assuming the transition energy of the ion does not change over time, the laser frequency will not change. However, the transition energy of the ion depends on the value of the fine-structure constant. Thus if α changes, the initial clock frequency at time t_i will have shifted to

$$\nu(t_f) = \nu(t_i) + 2q\frac{1}{\alpha}\frac{d\alpha}{dt} \tag{1.2}$$

at time t_f. The sensitivity factor q is introduced here to parametrize the sensitivity to the variation of α. By comparing two clocks with different sensitivity factors to each other while time evolves, it is possible to determine the variation of α. The most successful measurement of this kind was performed by comparing a transition of Al^+ with a transition of Hg^+ several times over the course of approximately a year [17]. In this case, the q factor of the Al^+ transition is essentially zero, while the q factor of the Hg^+ transition is approximately -52 200 cm^{-1} [18]. An overview of results obtained by experiments around the world is shown in Fig. 1.2. The simultaneous sensitivity to the variation of μ of some of the measurements is due to comparisons with hyperfine transitions. The transition energies of these directly depend on the proton-to-electron mass ratio. By combining the data sets, the currently most stringent limits to the variations were determined to be [15]

$$\frac{1}{\alpha}\frac{d\alpha}{dt} = -2.0(2.0)\cdot 10^{-17}/\mathrm{yr} \tag{1.3}$$

$$\frac{1}{\mu}\frac{\mu}{dt} = 5(16)\cdot 10^{-17}/\mathrm{yr}. \tag{1.4}$$

Thus, at the current level of precision, the results are consistent with no variation.

[1] National Institute of Standards and Technology, United States
[2] National Physical Laboratory, United Kingdom
[3] Physikalisch-Technische Bundesanstalt, Germany

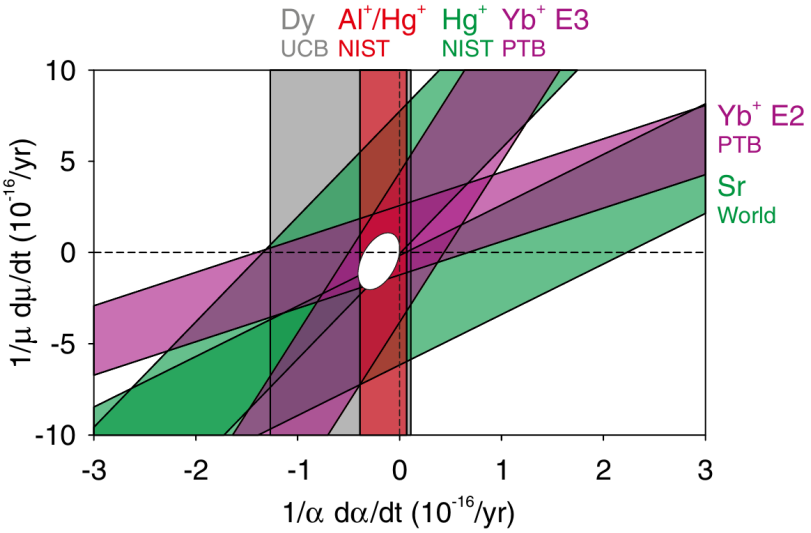

Fig. 1.2 Overview of upper limits for the variation of α and μ as measured by several groups [15, 17, 19–22]. The stripes indicate the 1-σ uncertainties on individual measurements, the white ellipse shows the 1-σ uncertainty for the combined data. Figure by Huntemann *et al.*, reused with permission [15].

The second method to search for variation of constants described here exploits the immense age and size of the universe. By investigating spectra that originate from extraterrestrial sources, fundamental constants can be probed over large space-time intervals. Webb *et al.* have been especially prolific in using this method to search for a variation of α [23–26]. They studied 295 so-called quasar-absorption spectra that were obtained with the Very Large Telescope (VLT) and the Keck telescopes. These can be observed when broadband light emitted by distant quasars travels through interstellar clouds. At characteristic wavelengths the light is absorbed by atoms, ions, and molecules that constitute the interstellar cloud. The investigated spectra originated from sources at redshifts z in the range of approximately $0.2 < z < 4.4$ and from both the northern and southern hemisphere. Thus a space-time interval of maximally approximately 20 Gyr could be studied. After each spectrum was corrected for its redshift, some wavelengths of absorption lines still showed deviations from their expected values. Systematic effects could have caused a common shift of the lines. However, since different lines were shifted by different amounts, this was excluded. As mentioned before, the sensitivity to a variation of α is not the same for all transitions. Hence, a variation of α over space-time could explain the observed effect. Webb *et al.* determined that the observed effect fits to a dipole-like variation of α with a statistical significance of 4.2 σ [25]. As our solar system moves relative to this dipole field over time, the variation of α on Earth is predicted to be at the level of $\Delta\alpha/\alpha \approx 10^{-18}$–$10^{-19}$ per year [27].

Due to the complexity associated with the interpretation of the quasar-absorption spectra, the results are controversial. Webb *et al.* themselves indicate that although significant efforts were made to exclude systematic effects, more measurements with other telescopes are required to constrain systematic effects further [25]. Moreover, Whitmore and Murphy pointed out systematic errors of the wavelength scales of the employed spectrometers at the VLT and Keck telescopes [28]. Currently, new measurements of quasar-absorption spectra specifically aimed at the search for α variation are being performed. Recently, an analysis including some of the new data was published [29]. The results support the dipole model. However, the amplitude of the dipole was found to be slightly smaller. When variation of a fundamental constant is claimed, compelling evidence from multiple sources is required to make such a profound statement plausible. Several other methods to search for variation of the fine-structure constant and other constants have been proposed and applied. An overview of such searches can be found for example in the work by Uzan [30]. The aforementioned method based on frequency standards has the advantage that the experimental parameters are potential well under control.

1.2 Highly charged ions as frequency standards

Currently, the second is defined as "9 192 631 770 periods of the radiation corresponding to the transition between the two hyperfine levels of the ground state of the caesium 133 atom" [31]. Proposed novel frequency standards use transitions with much shorter periods. Now, the radiation is in the optical regime, instead of the microwave regime of the cesium transition. This makes the fractional uncertainty

$$\sigma = \frac{\Delta\nu}{\nu_0} \tag{1.5}$$

much smaller. Assuming identical frequency uncertainties $\Delta\nu$, the fractional uncertainty for an optical transition centered at a frequency ν_0 can theoretically be a factor of 10^5 smaller [32]. This level of improvement has not yet been achieved due to the challenges associated with reducing $\Delta\nu$. The precision with which optical frequencies can be measurement has dramatically improved over the last decades, among others, due to the development of femtosecond frequency combs [33]. Additionally, by choosing transitions with line widths of 1 Hz or less, the central frequency ν_0 can be determined with extremely high precision. However, the uncertainty is not only due to statistical errors, but also due to uncertainties that systematic effects introduce [16].

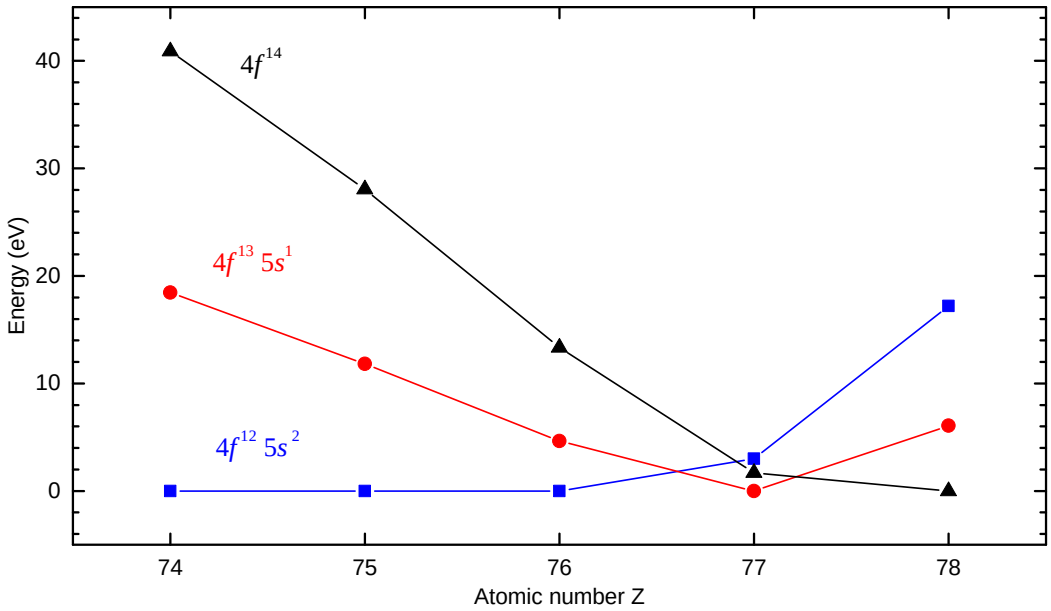

Fig. 1.3 Energy separation between the three lowest energy configurations of the Nd-like systems with atomic numbers $Z = 74 - 78$. The energies are based on Fock-space coupled cluster calculations [34].

The perfect frequency standard would not be perturbed by its environment. Unfortunately, the energy of atomic levels can be shifted by external electric and magnetic fields. For an in-depth discussion of these shifts refer to the publications by Gill [32] and of Ludlow *et al.* [16], selected sources of shifts are shortly introduced here. Typically, the investigated ions are trapped in a Paul trap which operates by virtue of an AC electric field applied by a set of electrodes. The micromotion of an ion in the electric field causes it to experience a non-vanishing root-mean-square (RMS) electric field that causes a quadratic Stark shift of the energy levels. Additional sources of non-vanishing RMS electric fields arise due to blackbody radiation from the environment and due to the laser fields that are employed to interrogate the ions. Due to imperfections on the surface of the electrodes, a non-vanishing electric field gradient can exist that couples to the electric quadrupole momenta for certain states ($J > 1/2$), which leads to quadrupole shifts of the energy levels. Significant efforts are made to reduce the uncertainty of these systematic effects by precision engineering and control of the setup. However, the systematic shifts are still the largest source of uncertainty. For example, in the Hg^{+} clock one of the largest uncertainties is due to the quadrupole shift, which causes a fractional uncertainty of 10^{-17} [17].

The susceptibility of highly charged ions (HCI) to external perturbations is much lower than that of the singly charged ions that are employed in current and proposed frequency standards [35–38]. This is mainly due to the small spatial spread of the electron wave

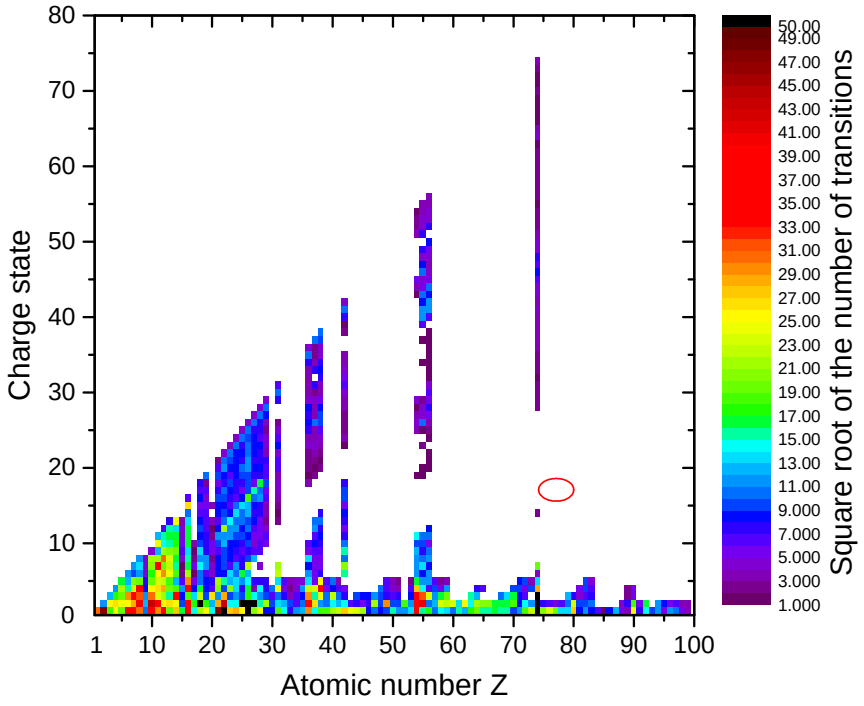

Fig. 1.4 Overview of the amount of electronic transitions that have been measured for the ions with atomic number $Z < 100$. The data was obtained from the NIST atomic spectra database [39]. For the white area no transitions were found in the database. The red circle indicates the part of the 'spectral desert' that is investigated in this work.

functions of HCI, caused by the strong attractive Coulomb field of their nuclei. To be able to exploit the previously described metrology techniques, the transitions under study have to be in the optical range. Many transitions in HCI do not meet this requirement due to the quadratic scaling with the atomic number Z^2 of the energy splitting between electronic configurations. However, for some HCI, two or more configurations can be nearly degenerate. The cause for such degeneracies relates to the fact that in a neutral atom, the ordering with energy of the configurations approximately follows the Madelung principle, whereas in the hydrogen-like limit the succession of levels approaches the Coulomb ordering. A level crossing can occur when, due to the removal of electrons from a neutral atom, the ordering of configurations transitions between the two types [18]. Due to the near degeneracy of configurations at level crossings, many optical ground-state transitions can exist in HCI. The systems investigated in this work include the Nd-like system Ir^{17+} ($Z = 77$), for which the relevant configurations are shown in Fig. 1.3 [27]. The properties of Ir^{17+} , and the type of available optical transitions in Ir^{17+} are discussed further in section 1.3.

Since the proposal by Berengut *et al.* to investigate HCI with optical ground-state transitions due to level crossings, abundant similar proposals have been made. Examples

include ions such as Sm^{14+}, Sm^{13+}, Pr^{10+}, Nd^{10+} [36], and Ho^{14+}, Cf^{15+}, Es^{17+}, Es^{16+} [40]. All these HCI have one or more near ground-state optical transitions with a line width of 1 Hz or less. Most of those clock transitions also have a high sensitive to the variation of α. However, all the proposed HCI have a common problem that currently prevents direct precision laser spectroscopy of the clock transitions. Due to a lack of experimental data, the complex electronic structure of the proposed HCI is not understood very well. An illustration of how severe the lack of experimental data is can be seen in Fig 1.4. Furthermore, the precision of predictions from theory is not good enough for laser spectroscopy. Electronic configurations with partially filled nd and nf subshells are extremely complex, since the number of possible spin and orbit couplings becomes very large. Calculations of the energy levels are hampered by the intricate electron correlations that are inherent to a level crossing. Even for systems that were specifically selected for their relatively simple electronic structure, the uncertainties on the predicted optical transition wavelengths are a few nm at best [36]. This is many orders of magnitude away from what would be needed. To overcome these problems, experimental spectral data on HCI near a level crossing are essential: first, to serve as a benchmark to test and improve predictions; second, to determine the wavelengths of the clock transitions with sufficient precision so that laser spectroscopy can be performed.

1.3 Ir^{17+} as a highly sensitive detector of variation of the fine-structure constant

The sensitivity of a transition to the variation of α was previously parametrized by the factor q. Equivalently to equation (1.2), for the energy of a fine-structure level the sensitivity can be defined. For the energy of electrons above closed shells, it can be shown that [41, 42]

$$q \approx -I_n \frac{(Z\alpha)^2}{n_e(j+1/2)}. \tag{1.6}$$

Here, $I_n = Z_e^2/2n_e^2$ is the ionization energy of the electron, Z_e is the effective nuclear charge that the electron experiences, n_e the associated effective principle quantum number, and j the total angular momentum quantum number. In shells that are nearly full, the screening of the nuclear charge Z is less effective. For those type of systems, the contribution of the ionization energy to the q factor is enhanced, so that $q \propto I_n^{3/2}$ [27]. Hence, systems with a large nuclear charge and with configurations with nearly filled shells provide the highest sensitivity to the variation of α. Guided by this, and by the restriction that the transitions have to be in the optical range, Berengut *et al.* proposed Ir^{17+} among other systems [27].

Table 1.1 Overview of the fine-structure states of the three configurations with the lowest energy in Ir^{17+} . The superscript ^{o} indicates that the parity of the state is odd. The values for the energies are based on measurements and Fock-space coupled cluster (FSCC) calculations, the units are eV [34]. The q factors, given in units of cm^{-1}, were determined in the work by Berengut *et al.* [27].

Configuration	Level	Energy	q
$4f^{13}5s^1$	$^3F_4^o$	0	0
$4f^{13}5s^1$	$^3F_3^o$	0.578	2065
$4f^{13}5s^1$	$^3F_2^o$	3.146	24 183
$4f^{13}5s^1$	$^1F_3^o$	3.764	25 052
$4f^{14}$	$^1S_0$	1.686	367 161
$4f^{12}5s^2$	$^3H_6$	3.004	-385 367
$4f^{12}5s^2$	$^3F_4$	4.128	-387 086
$4f^{12}5s^2$	$^3H_5$	5.935	-362 127
$4f^{12}5s^2$	$^3F_2$	6.767	-378 554
$4f^{12}5s^2$	$^1G_4$	6.973	-360 678
$4f^{12}5s^2$	$^3F_3$	7.291	-362 313
$4f^{12}5s^2$	$^3H_4$	9.754	-339 253
$4f^{12}5s^2$	$^1D_2$	10.163	-363 983
$4f^{12}5s^2$	$^1J_6$	11.639	-364 732
$4f^{12}5s^2$	$^3P_0$	11.566	-372 570
$4f^{12}5s^2$	$^3P_1$	12.236	-362 937
$4f^{12}5s^2$	$^3P_2$	13.237	
$4f^{12}5s^2$	$^1S_0$	21.594	

As was shown in Fig. 1.3, Ir^{17+} has three configurations that are nearly degenerate, two of the configurations have nearly closed $4f$ shells. The q factors of the fine-structure levels are listed in table 1.1. Due to the large differences between the q factors of the configurations, Ir^{17+} has several transitions that are suited for searches of α variation. Dipole-forbidden transitions are preferable because of their reduced line widths. Two examples are the $4f^{14}\ ^1S_0 - 4f^{13}5s^1\ ^3F_3^o$ and $4f^{12}5s^2\ ^3H_6 - 4f^{13}5s^1\ ^3F_4^o$ transitions, which have a combined $q = 750\,463\ cm^{-1}$. This order of magnitude enhancement over the Al^+/Hg^+ clocks, together with the reduced sensitivity of HCI to external perturbations, suggests that Ir^{17+} can be used to reduce the current limit on α variation by at least an order of magnitude.

Soon after the proposal in 2011 to use Ir^{17+} as a system to search for variation of the fine-structure constant, an experimental investigation of this ion was started at the Max Planck Institute for Nuclear Physics in Heidelberg. The Heidelberg electron beam ion trap (HD-EBIT) was employed to produce and trap the Ir^{17+} ions. Emission spectra of Ir^{17+} and other ions in the Nd-like sequence ($Z = 74$–78) were measured using a grating spectrometer that was sensitive in the optical range. Due to the large number of measured spectral lines and the uncertainties associated with the predictions, a direct identification of lines was not possible. However, due to the availability of spectra from multiple Nd-like systems and by employing several analysis techniques, a number of transitions taking place within configurations could be identified. An overview of them is shown in Fig. 1.5. Moreover, some yet unidentified lines were found to form, within the measurement uncertainty, closed optical cycles. Two of those closed cycles include candidates for transitions between the configurations. Since the two cycles (named case 1 and case 2) were mutually exclusive, no definitive conclusion regarding the energy splitting between the $4f^{13}5s^1$ and $4f^{12}5s^2$ configurations could be drawn. Therefore, the sought-after wavelengths of the ${}^3H_6 - {}^3F_4^o$ and ${}^1S_0 - {}^3F_3^o$ transitions could not be ultimately determined. In this work the electronic structure of Ir^{17+} is investigated through measurements of emission spectra in the EUV range. Furthermore, spectra with increased precision compared to previous measurements were taken of several lines belonging to case 1 and 2.

1.4 Alkali-like systems near the $4f$–$5s$ level crossing

The elements in the alkali group of the periodic table have been subject to extensive study because of their relatively simple electronic structure with a single ns electron outside closed shells. For the same reason, singly charged ions of the alkaline earth metals are the main subject of many experiments in atomic physics. In the realm of highly charged ions (HCI) too there is considerable interest in alkali-like ions, for example, the $2s$ - $2p$ transitions in Li-like Pr were studied recently as a means to access nuclear properties through the level splittings induced by the nuclear magnetic field [43]. A wide range of Na-like ions was investigated in the extensive work of Gillapsy and co-workers $3s$ - $3p$ [44]. The next iso-electronic sequence that has been investigated for its $4s$ - $4p$ transitions is not so much the K-like sequence but the Cu-like sequence, because a level crossing of the $4s$ and $3d$ configurations brings a single $4s$ electron above a closed $3d^{10}$ shell [45]. Similarly, level crossings make that the Pm-like iso-electronic sequence has a single $5s$ electron above a closed $4f^{14}$ shell. Curtis and Ellis were the first to publish on their theoretical investigation of Pm-like HCI [46].

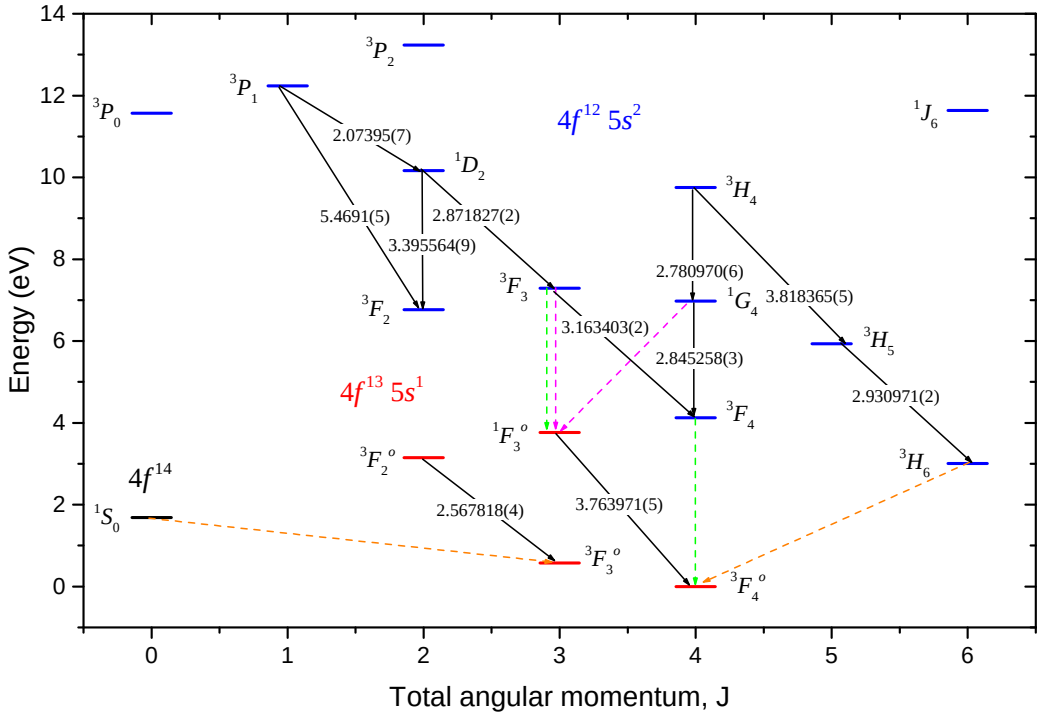

Fig. 1.5 Grotrian level diagram of Ir^{17+} showing the understanding of the energy levels obtained in out group during previous work [34]. The black solid arrows indicate identified transitions; their measured transition energy is given in units of eV. The dashed orange arrows indicate transitions with extremely narrow line widths and high values of q. The dashed green and magenta arrows respectively show "case 1" and "case 2" transitions that were possibly identified. The energy splitting between the configurations as shown here is based on FSCC calculations.

Chapter 2

Theory

> One, two, many.
>
> — Counting system of primitive tribes such as the Pirahã

A detailed treatise of atomic physics will not be given here, as that can be found in many textbooks (refer to citations throughout this chapter). Nonetheless, important equations and scaling laws necessary for a better understanding of the contents of this work will be introduced and discussed. Attention is given to important processes taking place in an EBIT. Subsequently, an introduction to the computational methods and tools employed to interpret the measurements made in the course of this work are given.

2.1 Basics of Atomic Physics

For a proper description of the properties of an atom, the theory of quantum physics is required [47–49]. In quantum physics, the system under study is completely described by a wave function $\Psi(t)$. To find the wave function the Schrödinger equation must be solved,

$$i\hbar\frac{\partial}{\partial t}\Psi(t) = H\Psi(t). \tag{2.1}$$

The Hamiltonian H, which acts on the wave function, needs to include all the interactions taking place in the system for a proper description. Solving the Schrödinger equation for a specific system is analogous to using Newton's second law of motion to determine the dynamics of a classical system. The values that observables can take are given by acting on the wave function with the appropriate operator. For example, the Hamiltonian operator

gives the energies E_i that the system can have as

$$H\Psi(t) = E_i\Psi(t). \tag{2.2}$$

2.1.1 Hydrogen-like systems

One of the simplest atomic systems is the hydrogen-like system, i.e. a nucleus of charge Ze with a single bound electron. The Hamiltonian for such a system is given by

$$H_{\text{Bohr}} = \frac{-\hbar^2}{2m_e}\nabla^2 - \frac{Ze^2}{4\pi\varepsilon_0 r}. \tag{2.3}$$

The first term takes into account the kinematics of the system based on the theory of Bohr. The second term accounts for the Coulomb interaction between the electron and the nucleus of charge Ze. Due to the spherical symmetry of the system it is convenient to work in spherical coordinates when solving the Schrödinger equation. The wave function is then split into a radial and an angular component as $\Psi(r) = R(r)\Upsilon(\theta,\phi)$. Solutions of the Schrödinger equation with H_{Bohr} predict the gross structure of the energy levels to be

$$E(n) = -\frac{m_e Z^2 e^4}{32(\pi\varepsilon_0)^2 n^2}, \quad n = 0,1,2,... \tag{2.4}$$

The principal quantum number n represents the quantization of the radial part of the system. Physicists in the 1920's employed perturbation theory to apply several small corrections to H_{Bohr}. These corrections account for the quantization of the orbital angular momentum and leading relativistic effects. The energy levels are then predicted to be

$$E(n,l) \approx -E(n)\left[1 + \frac{Z^2\alpha^2}{n^2}\left(\frac{n}{l+\frac{1}{2}} - \frac{3}{4}\right)\right] \tag{2.5}$$

to a good approximation. The quantum number l is associated with the orbital angular momentum. This lifts the degeneracy of levels with the same principal quantum number n into $l < n$ sublevels. The added structure is known as the fine structure. From equation (2.5) it follows that the size of the fine-structure splitting scales with Z^4, so in highly charged ions (HCI) the splitting can easily be in the keV range. But under certain conditions, as discussed in chapter 1, near level crossings the energy difference between fine-structure levels can be in the eV range.

The main problem with the Hamiltonian introduced in equation (2.3) is that it is intrinsically not relativistic [50]. This can be seen for example by the fact that the second derivative

with respect to spatial coordinates is taken, while in the Schrödinger equation only the first order derivative of the time coordinate is taken. Dirac solved this problem by introducing the following Hamiltonian [51],

$$H_{\text{Dirac}} = \boldsymbol{\beta} m_e c^2 + c\boldsymbol{\alpha}\left(-i\hbar\nabla - \frac{e}{c}\mathbf{A}\right) + e\Phi. \tag{2.6}$$

A full description of this Hamiltonian is beyond the scope of this work. However, it is apparent that this Hamiltonian, when substituted in the Schrödinger equation, treats the spatial and temporal coordinates alike. The resulting equation is generally known as the Dirac equation. The wave functions that are found when solving the Dirac equation are constructed from Dirac spinors $\varphi_{n,j,m}$ [50].

In the Dirac Hamiltonian the electromagnetic interaction is included in relativistic form by the electric potential ϕ and the vector potential $\boldsymbol{A}$. Moreover, it describes the spin of electrons with the Dirac matrices $\boldsymbol{\alpha}$ and $\boldsymbol{\beta}$. The spin of an electron behaves mathematically similarly as the orbital angular momentum of the electron. Each angular momentum observable has its own quantum number, l for orbital angular momentum and $s = 1/2$ for spin angular momentum. These couple to a total angular momentum of $j = |l-s|...|l+s|$ which can be substituted for l in equation (2.5) to obtain the approximate energy levels. It is customary to write the state of the system in term notation,

$$^{2s+1}l_j. \tag{2.7}$$

Here for l the spectroscopic notation $s = 1$, $p = 2$, $d = 3$, et cetera is used.

Further refinements to the energy levels of hydrogen-like systems can be made by considering quantum electrodynamic (QED) effects. An example is the interaction of the electron with virtual particle anti-particle pairs created by vacuum polarization. In strong electromagnetic fields the probability to create these virtual particle pairs is increased. The electric field that the electron in a hydrogen-like system experiences scales with Z^3, so for heavy HCI these effects start to play an important role. However, the systems investigated in this work are not charged highly enough to have an appreciable effect on the measurements.

2.1.2 Many-electron systems

Solving the Schrödinger equation for systems with more than one electron is not analytically possible anymore. The electrons interact not only with the nucleus, but also with each other,

so that the Hamiltonian turns into

$$H_{MB} = \sum_i H_{\text{Dirac},i} + \sum_{i<j} \frac{e^2}{|\boldsymbol{r}_i - \boldsymbol{r}_j|}. \tag{2.8}$$

Here, the sums are understood to be taken over all the electrons in the system. Computational methods to calculate the energy levels and to obtain the wave function of the system are discussed in section 2.3. Here general principles regarding the electronic structure of many-electron systems are discussed.

Since electrons have half integer spin (i.e. they are fermions) they obey the Pauli exclusion principle. Therefore, each electron has to be in a state with distinct quantum numbers n, j, m_j (m_j is the z-component of the angular momentum). Electrons with the same principal quantum number n are said to be in the same shell. A shell can consist of several subshells, which are defined by the angular momentum quantum number j. Many-electron systems can have multiple shells that are fully or partially filled with electrons. The notation for the electronic configuration of an atom is a sequence of nl^x, where x is the number of electrons in the subshell. For example, neutral boron in the ground state has the electron configuration $1s^2 2s^2 2p^1$. Note that when $x = 1$ it is sometimes omitted.

The angular momenta of the electrons can couple in two different ways. The Russell-Saunders regime is where the coupling between the orbital l and spin s angular momenta of individual electrons is weak compared to the coupling between the orbital angular momenta and the electron spins. The individual l's can then couple to form the total orbital angular momentum $L = \sum_i l_i$, similarly for the total spin $S = \sum_i s_i$. Those couple to form the total angular momentum $J = L + S$. Again, the state of the system is usually given in the term notation which was introduced in equation 2.7. Enhanced relativistic effects increase the strength of the spin-orbit coupling in high Z atoms. In that case the orbital l and spin s angular momenta of individual electrons couple to form the total angular momentum of a single electron j. These individual total angular momenta couple to form the total angular momentum $J = \sum_i j_i$. Thus, the total angular momenta L and S are not good quantum numbers anymore. In both cases, the total angular momentum J is a good quantum number that is important for a lot of the properties of the electronic structure. Additionally, the selection rules for transitions are governed in part by the J's of the involved states, more on that in section 2.1.5. Therefore, the Grotrian level diagrams in this work are often shown to have the values for the total angular momentum on the x-axis.

The nucleus can also have spin which interacts with the electrons, this gives rise to a hyperfine structure of the fine-structure levels. Since this effect scales with $\alpha^2 Z^3/n^3$ the hyperfine transitions can be in the optical range for HCI, such as for example in hydrogen-like

rhenium [52]. In Ti-like Re^{53+} however the hyperfine splitting is in the order of 1 meV due to the n^3 dependence and the screening of the nucleus [53]. The two naturally occurring isotopes of iridium ^{191}Ir and ^{193}Ir both have a nuclear spin $I = 3/2$ with nuclear magnetic momenta of respectively 0.1461 μ_N and 0.1591 μ_N [54]. This is approximately 20 times lower than that of ^{185}Re and ^{187}Re. Moreover, the valence electrons in Ir^{17+} have a higher principal quantum number and are more strongly screened by the closed shells. Hence the hyperfine splitting in Ir^{17+} is negligible compared to other effects, such as the Zeeman splitting which is discussed next.

2.1.3 The Wigner-Eckart theorem

When working with angular momentum eigenstates, the Wigner-Eckart theorem is a powerful tool to calculate expectation values of other operators [47]. In the next section this theorem is necessary to calculate the relative intensities of transitions. The theorem applies to systems with eigenstates $|jm\rangle$. In such a basis the expectation value of a general spherical tensor operator T^k of rank k is

$$\langle j'm'|T^k_q|jm\rangle = \langle jmkq|j'm'\rangle\langle j'||T^k||j\rangle. \tag{2.9}$$

Here q denotes the component of the operator. $\langle j'm'kq|jm\rangle$ is the Clebsch-Gordan coefficient for coupling j with k to get j', its value can be looked up in for example the Review of Particle Physics [55]. $\langle j'||T^k||j\rangle$ is the reduced matrix element, which does not depend on m, m', and q.

A specialized form of the Wigner-Eckart theorem called the projection theorem is introduced here too. It is valid for rank 1 spherical tensor operators $\mathbf{V}$ defined by their commutation relation

$$[V^i, J_j] = i\varepsilon_{ijk}J_k. \tag{2.10}$$

The projection theorem states that the expectation value of vector operators is proportional to the expectation value of $\mathbf{J}$.

$$\langle jm'|\mathbf{V}|jm\rangle = \frac{\langle jm'|\mathbf{V}\cdot\mathbf{J}|jm\rangle}{j(j+1)}\langle jm'|\mathbf{J}|jm\rangle. \tag{2.11}$$

2.1.4 Zeeman splitting

Even before the theory of quantum mechanics started to be developed, many quantum effects were observed experimentally. An example is the Zeeman effect, reported in 1897 by the

Dutch physicist Pieter Zeeman [56]. He observed that spectral lines are split into multiple components when the emitting medium is exposed to an external magnetic field. Since the ions investigated in this work were exposed to the strong magnetic field of the EBIT, the Zeeman effect needs to be taken into account.

Neglecting nuclear spin effects, which are a factor $m_p/m_e \backsimeq 1836$ smaller, the atomic magnetic moment is given by

$$\boldsymbol{\mu} = -\mu_B \mathbf{L} - g_s \mu_B \mathbf{S}. \tag{2.12}$$

Here $\mu_B = e\hbar/2m_e$ is the Bohr magneton, for which the CODATA recommended value $\mu_B = 5.788\,381\,801\,2(26) \cdot 10^{-5}$ eV /T was taken [13]. The Hamiltonian for a magnetic moment in an external magnetic field $\mathbf{B} = B_z \hat{\mathbf{e}}_z$ is given by

$$\mathbf{H}_{\mathrm{ZE}} = -\boldsymbol{\mu} \cdot \mathbf{B} = \mu_B B_z (L_z + g_s S_z). \tag{2.13}$$

As it turns out, for the magnetic field strengths applied in this work, the effect is small enough so that it can be treated as a perturbation of the spin-orbit interaction. The correction to the energy is then

$$\begin{aligned} \Delta E_{\mathrm{ZE}} &= \langle jmls | \mathbf{H}_{\mathrm{ZE}} | jmls \rangle \\ &= \mu_B B_z \langle L_z + g_s S_z \rangle \\ &= \mu_B B_z \frac{\langle \mathbf{L} \cdot \mathbf{J} \rangle + g_s \langle \mathbf{S} \cdot \mathbf{J} \rangle}{j(j+1)} \langle J_z \rangle \\ &= \mu_B B_z g_j m_j. \end{aligned} \tag{2.14}$$

For legibility, the eigenstate quantum numbers are omitted from line two onward. The third line is obtained by application of the projection theorem. In the final step the Landé g-factor is defined as

$$g_j \equiv 1 + (g_s - 1) \frac{j(j+1) - l(l+1) + s(s+1)}{2j(j+1)}. \tag{2.15}$$

Inclusion of the Breit interaction and QED effects can change this g_j-factor from the third digit on.

2.1.5 Zeeman transitions

When an atomic system transitions between two energy levels the excess energy can be released in the form of a photon. In this work, the wavelength of the emitted photons

was measured to gain insights about the electronic structure of ions. The transition energy between two fine-structure levels is given by

$$\begin{aligned}\Delta E &= E^i + \Delta E^i_{\mathrm{ZE}} - E^f - \Delta E^f_{\mathrm{ZE}} \\ &= \Delta E_{\mathrm{FS}} + \Delta E_{\mathrm{ZE}}.\end{aligned} \tag{2.16}$$

The superscripts denote the initial i state and the final f state. Equation (2.14) shows that the energy of a fine-structure level in a magnetic field B_z is split into $2j+1$ sub-levels. Thus a fine-structure transition is split into a number of transitions with energies slightly deviating from the central wavelength ΔE_{FS}. The energy differences from the central wavelength are given by

$$\begin{aligned}\Delta E_{\mathrm{ZE}} &= \mu_B B_z (g^i_j m^i_j - g^f_j m^f_j) && \\ &= \mu_B B_z m^i_j (g^i_j - g^f_j) && \text{for } \Delta m = 0 \\ &= \mu_B B_z (m^i_j (g^i_j - g^f_j) \pm g^f_j) && \text{for } \Delta m = \pm 1.\end{aligned} \tag{2.17}$$

The division into $\Delta m = m^i - m^f$ groups is in anticipation of the selection rules which will be introduced below. The equations (2.17) show that the energy splitting between the Zeeman transitions is determined by $g^i_j - g^f_j$, and the splitting between the Δm groups by g^f_j, refer to Fig. 2.1.

To compare the predicted splitting with observations, it is necessary to determine the relative intensities of the transitions between the Zeeman sub-levels. Transitions rates between an initial state $|i\rangle$ and final state $|f\rangle$ separated by an energy E can be calculated using Fermi's golden rule

$$A_{if} \propto E^3 \langle f|T|i\rangle^2. \tag{2.18}$$

Here the interaction between the states is governed by the operator T. In the electric dipole approximation the operator is simply $-e\mathbf{r}$. With the quantization axis defined by the B-field in the z-direction, the dipole operator can be written as the spherical tensor operator D_q of rank 1

$$\begin{aligned}D_1 &= -\frac{e}{\sqrt{2}}(r_x + i r_y) \\ D_0 &= e r_z \\ D_{-1} &= -\frac{e}{\sqrt{2}}(r_x - i r_y).\end{aligned} \tag{2.19}$$

Now, to find the relative intensity of a Zeeman transitions between two fine-structure levels $|j^i m^i\rangle$ and $|j^f m^f\rangle$

$$\begin{aligned} A_{if} &\propto \langle j^f m^f | D_q | j^i m^i \rangle^2 \\ &= \langle j^f m^f 1q | j^i m^i \rangle^2 \langle j^f || D || j^i \rangle^2 \\ &= \langle j^f (m^i + \Delta m) 1 \Delta m | j^i m^i \rangle^2 \langle j^f || D || j^i \rangle^2, \quad \Delta m = 0, \pm 1. \end{aligned} \tag{2.20}$$

In the first step the Wigner-Eckart theorem is applied. The second step follows from the fact that the Clebsch-Gordan coefficients are only non-zero when $q + m^i - m^f = 0$. Furthermore, the reduced matrix element is equal for all the Zeeman transitions between the fine-structure levels. So the relative intensities of the Zeeman components only depend on the Clebsch-Gordan coefficients. In similar vein as the selection rule for the Δm's, it follows that $\Delta j = 0, \pm 1$. However, $j = 0 \rightarrow j' = 0$ transitions are not allowed. And finally, since the electric dipole operator is odd with respect to parity transformations, electric dipole (E1) transitions can only take place between states of opposite parity.

Similarly to the derivation of the relative intensities and selection rules for E1 transitions, it is possible to derive these for magnetic dipole (M1) transitions. The interaction operator in that case is the magnetic moment from equation (2.12). Only a few selection rules are different compared to E1 transitions. Because the magnetic moments operator is even with respect to parity transformations, M1 transitions only take place between states of the same parity. The interaction due to the magnetic dipole operator is much weaker then that of the electric dipole operator

$$\frac{\langle \boldsymbol{\mu} \cdot \mathbf{B} \rangle^2}{\langle e\mathbf{r} \cdot \mathbf{E} \rangle^2} \sim \left(\frac{\mu_B / c}{e a_0 / Z}\right)^2 \sim (\alpha Z)^2. \tag{2.21}$$

Since the total rate in (2.18) grows with E_0^3, in HCI the rate of M1 transitions scales with Z^{10} whereas E1 transition rates scale with Z^4. Hence, M1 transitions in the optical regime can be as strong as, or even stronger than E1 transitions.

The angular distribution of the emitted photons can be deduced by considering the form of the dipole operator in spherical tensor form, equation (2.20), and the Δm selection rules. For $\Delta m = 0$ the system behaves as a linear oscillator in the z-direction. And for $\Delta m = \pm 1$ the ion behaves as a circular oscillator in the xy-plane. The radiation pattern then follows

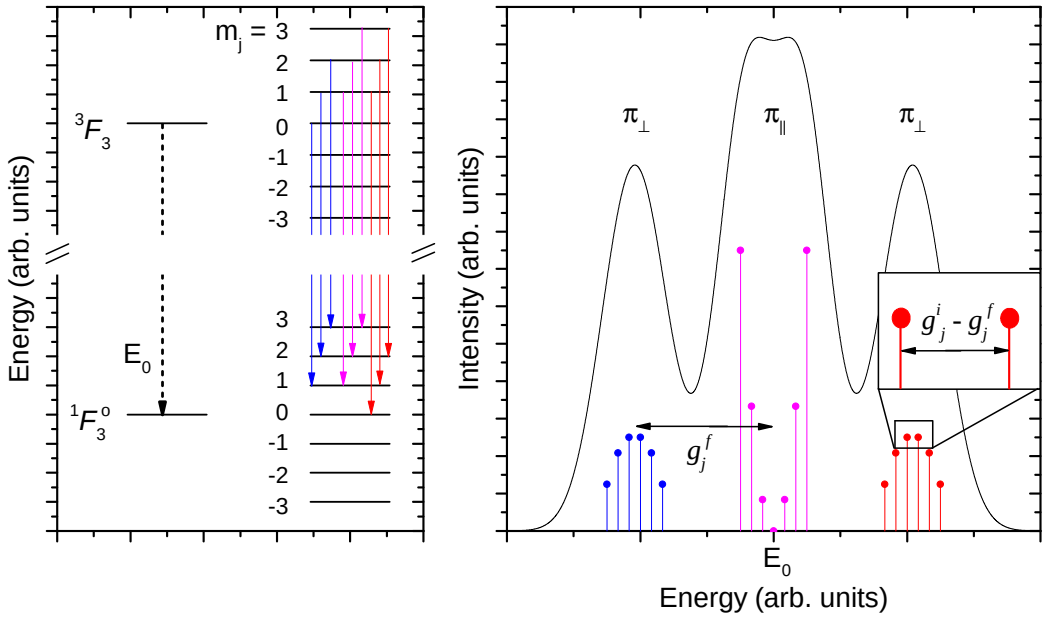

Fig. 2.1 Example of Zeeman splitting and of transitions between Zeeman levels. The initial ${}^3F_3$ and final ${}^1F_3^o$ are levels in Ir^{17+} . Since the levels are of opposite parity, an E1 type transition is expected. The g_j-factors were calculated using the Landé equation (2.15). In the left figure only a limited number of transitions are indicated for visibility, red $\Delta m = -1$, magenta $\Delta m = 0$, blue $\Delta m = +1$. In the right plot the intensities were calculated using the Clebsch-Gordan coefficients. Furthermore, the intensities were corrected for perpendicular observation according to equation (2.23). The black arrows and inset show how the splitting between the Zeeman components depends on the g_j-factors.

from classical electrodynamics [57],

$$I_{\Delta m=0} = \frac{3}{8\pi}\sin^2\theta \qquad (2.22)$$
$$I_{\Delta m=\pm 1} = \frac{3}{8\pi}\frac{1+\cos^2\theta}{2}.$$

In the measurements performed during this work, the observations were always made perpendicular to the magnetic field axis, so that

$$I_{\Delta m=0} = 2I_{\Delta m=\pm 1}. \qquad (2.23)$$

This equation holds for E1 and M1 transitions [49]. The polarizations of the emitted light are always linear when observed perpendicular to the magnetic field axis. However, the direction of the polarization depends on the type of transition and the Δm of the transition, the possibilities are summarized in table 2.1. Most importantly for the measurements in this

Table 2.1 Overview of the polarizations of fluorescence light from Zeeman transitions as observed either parallel or perpendicular to the magnetic field axis [49]. The light can be circularly polarized $\sigma^{\pm}$, linear parallel to the magnetic field axis $\pi_{\perp}$, or linear perpendicular to the magnetic field axis $\pi_{\parallel}$.

	E1		M1	
Δm	Parallel	Perpendicular	Parallel	Perpendicular
+1	σ^{-}	$\pi_{\perp}$	-	$\pi_{\parallel}$
0	-	$\pi_{\parallel}$	$\sigma^{\pm}$	$\pi_{\perp}$
-1	σ^{+}	$\pi_{\perp}$	-	$\pi_{\parallel}$

work, the polarization direction for the $\Delta m = 0$ and $\Delta m = \pm 1$ transitions switches depending on the transition being either E1 or M1. An example for the line shape of an Ir^{17+} transition due to all the aforementioned effects is shown in Fig. 2.1, more predicted line shapes for Ir^{17+} are given in appendix A.

2.2 Electron-ion interactions in an EBIT

The ions studied in this work were produced and trapped in an electron beam ion trap (EBIT). As the name suggests, in the EBIT an electron beam interacts with ions. Typically anywhere from 10^4 to 10^7 ions are trapped in a cylindrical volume of a few centimeter in length and approximately 500 µm in diameter. A more comprehensive discussion of the EBIT is given in chapter 3. In this section, the significant processes taking place in an EBIT are introduced and given theoretical background.

In an EBIT, sequential ionization to higher charge states is accomplished through electron impact ionization. In this process, an ion A of charge state q and in quantum state a interacts with an energetic electron. If the electron is energetic enough it can transfer part of its kinetic energy to the ion and thereby eject a bound electron from the ion,

$$A_a^q + e^- \rightarrow A_b^{q+1} + 2e^-. \tag{2.24}$$

At the end of the interaction the ion is left in the next higher charge state $q+1$ and quantum state b. The cross section in units of cm^2 for this process can be estimated with the semiempirical equation proposed by Lotz [58],

$$\sigma_{qa}^{\mathrm{EII}} = 4.5 \times 10^{-14} \sum_i \xi_i \frac{\ln(E_e/I_{iab})}{E_e I_{iab}}. \tag{2.25}$$

Here the ξ_i is the number of equivalent electrons in the subshell of the initial quantum state. Obviously the electron energy E_e needs to be as large, or larger then the ionization energy I_{iab} required to bring the ion to the state A_b^{q+1}. As a rule of thumb, the Lotz equation predicts that the maximum electron impact ionization cross section is at approximately 2.5 times the ionization energy I_{iab}. Since high energetic states are usually short lived (c.f. equation (2.18)) with respect to the rate of electron impact ionization, often only the ionization from the ground state needs to be considered. However, in some cases long lived meta-stable states exist that allow for efficient ionization even though E_e does not exceed the ionization energy of the ground state yet [59].

Electron impact not only causes ionization, it can also directly bring the atom to another quantum state,

$$A_a^q + e^- \rightarrow A_b^q + e^-. \tag{2.26}$$

When the ion is brought to an energetically higher state this is know as excitation, otherwise it is know as de-excitation or quenching. Electron impact excitation can occur only when the electron beam energy E_e is equal to, or higher, than the energy difference between the initial and final states E_{if}. The cross section for excitation of ions (not that of atoms) has its maximum at threshold, that is, when $E_e = E_{if}$. For dipole transitions the cross section at much higher energies decreases as [60, 61]

$$\sigma^{\mathrm{EIE}} \approx \frac{A}{E_e} + B\frac{\ln E_e}{E_{if}} \quad E_e \gg E_{if}. \tag{2.27}$$

Here A and B are constants. The value for the cross section in units of cm^2 at threshold can be approximated by the semiempirical van Regemorter equation [62],

$$\sigma^{\mathrm{EIE}}_{\mathrm{maximum}} \approx \frac{4.72^{-18}}{E_{if}^2}, \tag{2.28}$$

with E_{if} in eV. In general the electron impact ionization cross section is much larger than the cross section for excitation. Therefore, only when the electron beam energy is near the ionization energy of an ion will excitation play a role. At that point the electron beam energy is so high that mainly states with a high principal quantum number n are populated. The ion subsequently relaxes though multi-step radiative decay.

Photon ionization and excitation is not discussed in this work since the cross sections for these processes are relatively small and the photon density during the measurements was low. Only when intense radiation from an external source is introduced, does the need to consider

photon excitation and ionization arise. This is for example the case when the radiation from a free electron laser (FEL) is overlapped with the ion sample [63].

The inverse process of ionization, recombination of an electron with an ion, also occurs in the EBIT. The simplest recombination process is radiative recombination (RR), in which a free electron recombines with an ion and the excess energy is directly emitted in the form of a photon,

$$A_a^q + e^- \rightarrow A_b^{q-1} + \gamma. \tag{2.29}$$

Though electron-electron interactions there are instances when the excess energy can excite already bound electrons to a higher energetic state. Only in the next step is the excess energy radiated away, so that the total process can be described as

$$A_a^q + e^- \rightarrow A_b^{q-1} \rightarrow A_c^{q-1} + \gamma. \tag{2.30}$$

In the most common form of this process only one bound electron is raised to a higher state, in which case the process is known as dielectronic recombination. Since the excess energy has to be equal to the energy required for the excitation of the bound electrons, this is a resonant process. Recombination processes are extensively studied in the EBIT community, predominantly with the goal of providing data to model astrophysical object, refer for example to the review by Beiersdorfer [64]. Recombination processes to the L-shell of iridium were investigated by Hollain to gain a better understanding of the electronic structure of this element [65].

2.3 Computational methods in atomic physics

Over the course of this the work predictions from the lexible atomic code (FAC) were extensively used to interpret the performed measurements. The abilities of FAC include the calculation of atomic properties such as the energies of fine-structure levels, transition rates, and collisional excitation cross sections. Additionally, the libraries include a module to perform collisional radiative modeling of plasmas. The code was developed by M. F. Gu, who also published a review describing the basic functionality [66]. The advantages of FAC are its user friendliness and that most calculations can be performed in limited time on personal computer systems. In general, the results are accurate enough to identify lines in spectra. For example, predictions for the wavelengths of L-shell transitions were proven to be accurate at the level of 0.1% [67, 68].

Several numerical methods exist to solve the Schrödinger equation and thereby obtain a good approximation of the wave function. All the methods described here use the Dirac-Coulomb-Breit Hamiltonian

$$H_{\mathrm{DCB}} = \sum_i H_{\mathrm{Dirac},i} + \sum_{i<j} \frac{e^2}{|\boldsymbol{r}_i - \boldsymbol{r}_j|} + B_{ij}. \tag{2.31}$$

Which is equal to the Hamiltonian introduced in equation (2.8) plus the Breit operator B_{ij} [69]. The Breit operator partially takes into account retardation effects and magnetic interactions between the electrons. In FAC, a configuration interaction (CI) method is implemented. This method is also the basis for the results provided by N. S. Oreshkina. The results provided by A. Borschevsky were obtained using a coupled cluster (CC) method. Both methods are discussed shortly in the next section. Subsequently, an introduction to the collisional radiative model (CRM) is given.

2.3.1 The configuration interaction method

The wave function of a specific state of an N electron system can be described by configuration state functions (CSF). These are the antisymmetritrized products of N one-electron wave functions. The antisymmetric condition is required so that the Pauli principle is upheld. Usually, the Slater determinant

$$\phi = \frac{1}{\sqrt{N!}} \begin{vmatrix} \varphi_1(a_1) & \cdots & \varphi_N(a_1) \\ \vdots & \ddots & \vdots \\ \varphi_1(a_N) & \cdots & \varphi_N(a_N) \end{vmatrix} \tag{2.32}$$

is introduced to mathematically represent antisymmetritrized product. The $\varphi_i(a_i)$ represent solutions of the one-electron Dirac equation with quantum numbers a_i. In the configuration interaction Dirac-Fock-Sturmian (CIDFS) method as applied by N. S. Oreshkina, the $\varphi_i(a_i)$ for occupied orbitals are obtained from a multiconfiguration Dirac-Fock calculation [70, 71]. The one-electron wave functions for correlation orbitals were constructed from Sturmian basis functions.

The full solution to the multi-electron Dirac equation is a superposition of the CSF,

$$\Psi = \sum_i b_i \phi_i. \tag{2.33}$$

Ideally, the sum would be taken over all the possible configuration state functions ϕ_i. In the configuration interaction method the coefficients b_i are varied to yield the minimal energy for the system,

$$E = \langle \Psi | H | \Psi \rangle = \sum_i b_i \langle \phi_i | H | \phi_i \rangle. \tag{2.34}$$

For systems with many electrons it is often too computationally expensive to take the sum over all CSF, then the sum is truncated. Typically, the CSF are categorized according to the number of electrons excited from the ground state. For example, the CIDFS calculations were performed for a CSF basis of single excitations up to the $7s$, $7p$, $7d$, and $7f$ subshells and double excitations up to the $5p$ subshells. Even with such a relatively large basis and corresponding cost in computational time, the results did not show convergent behavior yet. Therefore, the uncertainty on the energies of the configurations was estimated to be approximately 1 eV. The uncertainty on the energy of fine-structure levels within a configuration was estimated to be at the level of 1% [72].

2.3.2 The coupled cluster method

In the coupled cluster method a different form for the full wave function is chosen, namely

$$\Psi = e^T \phi_0. \tag{2.35}$$

Here ϕ_0 is the CSF for the ground state of the system, and T is the so-called cluster operator [73]. The cluster operator is the sum of excitation operators,

$$T = \sum_i T_i. \tag{2.36}$$

The subscript i denotes how many excitations are produced by the operator. The general form of the cluster operator is given by

$$T_n = \frac{1}{(n!)^2} \sum_{h_1 \cdots h_n} \sum_{p_1 \cdots p_n} t_{p_1 \cdots p_n}^{h_1 \cdots h_n} a^{p_1} \cdots a^{p_n} a_{h_1} \cdots a_{h_n}. \tag{2.37}$$

Here the a denote creation and annihilation operators for occupied orbital h and unoccupied orbital p. The coefficients t are found by inserting the Hamiltonian (2.31) and the wave function (2.35) in the Schrödinger equation and solving for t [73].

The calculations performed by A. Borschevsky were limited to include up to double excitations. With this in mind, the exponential part of equation (2.35) can be expanded in a

Taylor series,

$$e^T = 1 + T + \frac{1}{2!}T^2 + \cdots \\ = 1 + T_1 + T_2 + \frac{1}{2}T_1^2 + T_1T_2 + \frac{1}{2}T_2^2 + \cdots \tag{2.38}$$

Although only excitation operators up to T_2 are considered, contributions of higher order excitations are also partly included by terms such as for example T_1T_2 for triple excitations. This makes the CC method very suited for calculations on highly correlated systems such as those studied in this work. The specific code used for the calculations by A. Borschevsky was written by E. Eliav, U. Kaldor, and Y. Ishikawa [74]. In the code, the ground state CSF ϕ_0 is found by a method based on the Dirac-Fock basis expansion [75]. Therefore, the complete method is known as the Fock-space coupled cluster (FSCC) method.

2.3.3 The collisional radiative model

To interpret emission spectra from plasmas it is often necessary to consider several excitation and de-excitation processes taking place in plasmas. Mathematically these processes can be modeled with a collisional radiative model (CRM) [76]. This method has for example been applied successfully to interpret x-ray spectra of stars as recorded with space observatories [77]. Also the interpretations of spectra from laboratory-produced spectra have greatly benefited from the support of CRM [78, 79]. In this work the CRM module of the FAC package was employed to generate synthetic spectra that could be compared to measured spectra [80].

As discussed in section 2.2, the main processes in and EBIT are electron impact ionization, electron impact excitation, and recombination. The charge state distribution is assumed to remain constant over time and to be dominated by the investigated charge state. Hence, excitations due to recombination from a higher charge state can be neglected. Electron impact ionization is assumed to mainly produce ions in their ground state. Therefore, the effects of ionization and recombination can be neglected for the modeling. Thus, the rate equation for the time dependence of the population n_i of the state i can be written as

$$\frac{dn_i}{dt} = \sum_{i>j} \rho_e C(\sigma_{ij}^{\mathrm{EIE}}, E_e) - \sum_{i<j} \rho_e C(\sigma_{ij}^{\mathrm{EIE}}, E_e) - \sum_{i>j} n_i A_{ij} + \sum_{i<j} n_j A_{ji}. \tag{2.39}$$

The first term accounts for the excitation from a less energetic state j by means of electron impact. The size of this term is determined by the electron density ρ_e, the energy of the electrons E_e, and the cross section for this process σ^{EIE}. The second term in equation (2.39)

accounts for the opposite process, electron impact de-excitation (quenching) from more energetic state j. The third term accounts for spontaneous decay from the state i to the state j which is described by the Einstein A_{ij} coefficient [81]. The fourth and last term describes spontaneous decay from a more energetic state j to the state i. The set of coupled differential equations for all the states n_i is homogeneous and therefore does not yield a unique solution. Therefore it is common to introduce the normalization $\sum_i n_i = 1$. For systems with a modest amount of states the set of differential equations can be solved using standard computational methods, larger system require more specialized techniques which are implemented in the FAC libraries [80, 82].

Chapter 3

Experimental setup

Man benutzt keinen Hammer für einen supraleitenden Magneten!

— J. R. Crespo López-Urrutia, August 2013

Since the successful development of the first electron beam ion trap (EBIT) in 1986 [83], it has become the apparatus of choice for the production and investigation of highly charged ions (HCI). There are two main reasons for this. First, there is the control of the experimental parameters: Due to the well-defined properties of the electron beam it is possible to selectively produce a certain charge state, to have control of the energy of the free electron in recombination processes, and to have a stable sample of HCI for long periods of time. Secondly, the cost of developing and operating an EBIT is relatively low: typical development costs are around one million euros, and the relatively small size and complexity of the apparatus mean that a single person can operate the apparatus. This is in contrast with apparatuses and techniques such as tokamaks [84], stellarators [85], and electron stripping of accelerated ions [86]. All but the last of these apparatuses produce broad charge state distributions, which makes the interpretation of spectra difficult and reduces the type of experiments that can be performed. Additionally, many of the mentioned apparatuses typically require years of development, and many millions of euros to build. Once build, the operational costs are high, which often limits the amount of available time for experiments. Electron cyclotron resonance ion sources (ECRIS) also deserve a mention here, they are on par with EBIT when it comes to developing costs and complexity [87, 88]. However, the charge state distribution of the ion sample in ECRIS is typically much broader, and production of the highest charge states is not possible. Furthermore, ECRIS sources provide little, if any, optical access to the trapped plasma.

In the following, the general principle of operation of an EBIT is explained, the details of important parts are then further elucidated in separate sections. The results obtained in

this thesis were all realized at the Heidelberg EBIT (HD-EBIT) located at the Max Planck institute for nuclear physics in Heidelberg. Relevant properties specific to the HD-EBIT will be given where necessary. The HD-EBIT was built and operated at the university of Freiburg in 1999 [89]. In 2001 it was moved to Heidelberg, where it has since been employed for various investigations of HCI [90, 91].

Finally, the working principle of two important tools in the spectroscopist's toolbox are introduced: gratings and cameras. Specific details of the gratings and CCD cameras employed for the different measurements in this work are discussed in chapters 4 and 5.

3.1 The electron beam ion trap

Ionization of particles in an EBIT is achieved through electron impact ionization. The required electrons are emitted as a beam from the electron gun. This beam is then compressed in a strong magnetic field to a diameter of approximately 50 µm. In the HD-EBIT, the magnetic field of up to 8 T is induced by a pair of superconducting coils in Helmholtz configuration. The ionization rates due to this are enough to overcome competing processes such as charge exchange with residual gas. Refer to Fig. 3.1 for a schematic drawing of the construction.

Ions are trapped radially to the electron beam due to its negative space charge. By applying suitable electrical potentials to a series of drift tubes (DTs) which are on axis with the electron beam, the ions are prevented from escaping in the axial direction. Since the ions near the trap center are forced on cyclotron orbits due to the strong magnetic field, they can be trapped for periods of time even on the order of minutes in the absence of the electron beam. This has been done for example to measure the lifetime of the $1s^2 2s^2 2p^2 P^o_{3/2}$ level in Ar^{13+} [92].

Neutral particles that traverse the electron beam are quickly stripped of their valence electron; consequently it is trapped and sequentially ionized to a charge state q. This process can take place as long as the electron beam energy is higher than the ionization energy of an ion. The electron beam energy, and thus the maximum achievable charge state, is determined by the electrical potential difference between the electron gun and the central DT. The electron beam expands again leaving the drift tube assembly and area of the strongest magnetic field, it is finally stopped at the electron collector.

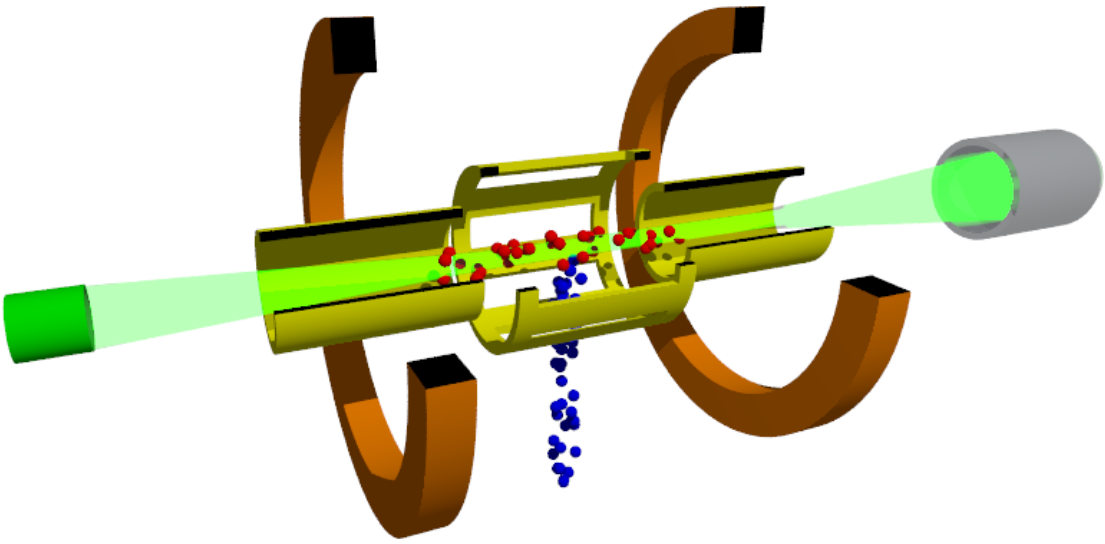

Fig. 3.1 Principle of operation of an EBIT. The electron beam (light green) is emitted from the cathode (green) and focused by the magnetic field of the coils (orange). Injected atoms (blue) are ionized at the trap center by electron impact. Ions (red) produced in the trap are confined by the space charge potential of the electron beam and the electric field produced by the drift tubes (yellow). The central drift tube is slotted to allow for observation of the ion cloud. After passing thought the drift tubes, the electron beam is dumped at the collector (gray).

3.1.1 The electron gun

The emission of electrons from hot cathodes has been studied extensively during past decades; mainly with the aim of improving these cathodes for application in microwave tubes. A thorough review of the history of dispenser cathodes can be found in the work of Cronin [93]. In the Philips labs it was discovered that a mixture of BaO, CaO, and Al_2O_3 has exceptionally good emission qualities due to the low work-function of the barium. By impregnating a tungsten matrix with the barium mixture it is possible to achieve the high temperatures of approximately 1200 °C that are necessary for efficient emission. However, due to these high temperatures, small amounts of barium and tungsten also evaporate from the cathode, which show up as contaminants of the ion cloud.

The cathode of the HD-EBIT has a diameter of 3.4 mm, which allows for a space-charge limited emission of up to 500 mA. The geometry of the cathode, its holder, and of the focus electrode are based on the work of Pierce [95], his design was optimized to produce a laminar flow of electrons. A third electrode, the anode, helps to focus the beam at the trap center.

An important requirement for optimal flow of the beam is the absence of a magnetic field at the position of the cathode, so the field due to the superconducting coils needs to

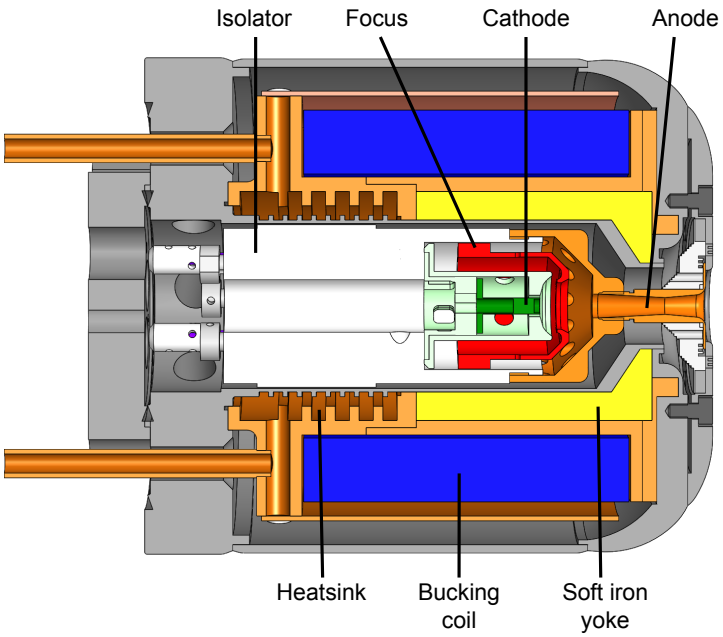

Fig. 3.2 Cross section of the electron gun of the HD-EBIT. The cathode, anode, and focus electrode are mounted on the isolator, which is made of non-conductive Macor™. The electrical connections for the electrodes run through the isolator and connect to the flange on the left (connections not shown). Cooling water flows through the heat sink to transport away the heat produced in the bucking coil.

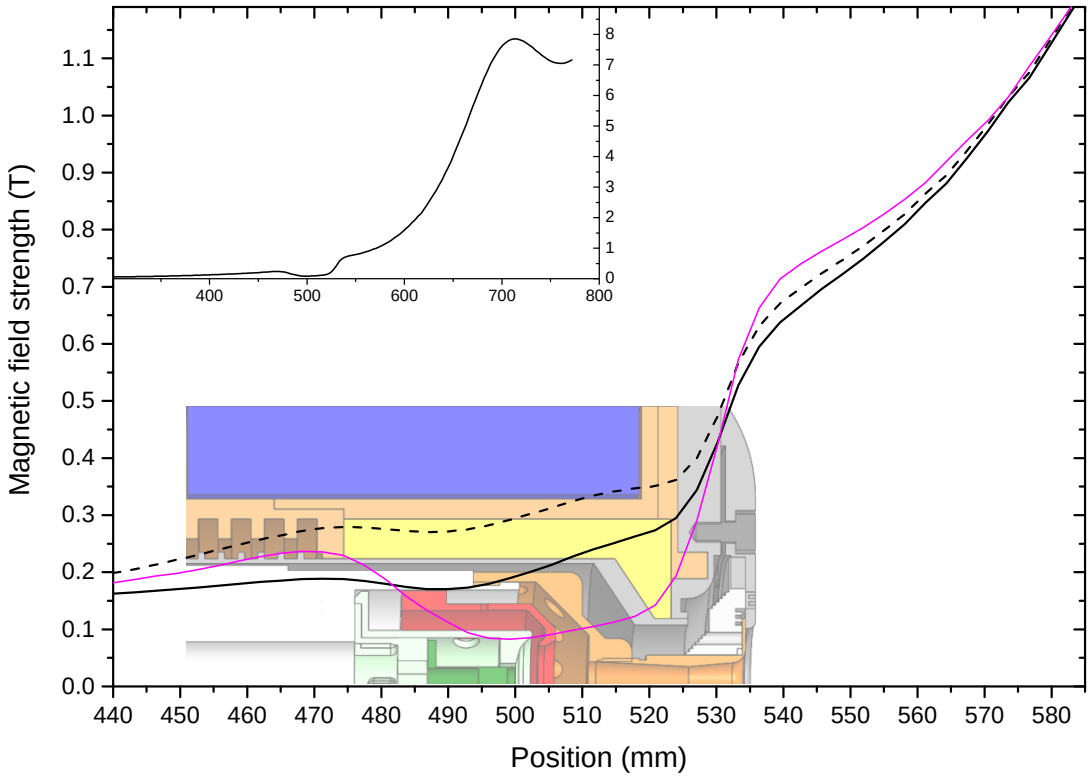

Fig. 3.3 Results of the magnetic field strength simulations performed with a finite element method in FEMM [94]. The results for the original design are shown in black, where the dashed line depicts the field strength when the coils are switched of and the continuous line depicts the field when both coils are at maximum current. The magenta line depicts the field strength for the new design with the bucking coil at maximum current. Part of the technical drawing of the gun is shown for reference. The inset shows the magnetic field strength over a larger region, including the first superconducting coil and the trap center.

be canceled here. To achieve this, the cathode is shielded from the residual magnetic field of the superconducting magnet by a soft iron yoke. Additionally, for increased control of the magnetic field at the cathode position, a bucking coil is installed around the yoke. This coil also helps to make the transition of the electron beam into the magnetic field of the superconducting coils smooth. In the original design of the gun for the HD-EBIT there were three additional small trim coils within the yoke to make a weak magnetic field in the axial and two lateral directions. At the start of this work the bucking coil had a short circuit, and the lateral trim coils were not used because their usefulness was limited. Although the gun still functioned with only the axial trim coil, modifications were required for a better focusing of the beam. The new design is shown in Fig. 3.2. The biggest change is that the new design does not have any trim coils anymore, but instead has a bigger yoke. The bigger yoke is predicted to shield the cathode better against external magnetic fields, see Fig. 3.3.

Two thermocouples were installed between the windings of the bucking coil. These are used to monitor the temperature of the coil to prevent overheating and subsequent short circuits. Additional improvements were the increase of distance between the focus electrode and the housing, thereby reducing the risk of discharges. The front of the gun housing was made smoother to prevent discharges between the gun and electrodes directly in front of the gun. The new gun was installed in 2014 and performed very well. Currents of 400 mA at energies of up to 60 keV were achieved, at which H-like Xe^{53+} was produced and extracted.

3.1.2 The central region

At the center of the EBIT the ions are produced and trapped. The central vacuum chamber of the HD-EBIT houses the drift tube assembly, the superconducting coils, and the cryogenic system, see 3.4. The superconducting coils of the HD-EBIT are mounted in a vessel which holds enough liquid helium to keep the magnet immersed and in a superconducting state for one week. This storage time is achieved due to two heat shields surrounding the liquid helium vessel in the vacuum. With a cryocooler, the heat shields are cooled to 20 K and 50 K. The large cryogenic surfaces provide pumping power in addition to the pumping with conventional turbomolecular pumps. In this manner a pressure of better than 10^{-10} mbar can be achieved.

The drift tube assembly consists of nine electrodes and their support structure. It runs through two opposing ports of a six-way cross, with the central drift tube at the center of the cross. Following the drift tubes are two electrodes known as the trumpet and the transport tube. Potentials can be applied to these to adjust the guiding of electrons and ions to the collector. The lower port of the six-way cross is employed for the injection of neutrals. The two horizontal ports for measurements of the fluorescence light from the ion cloud. Access to the upper arm was restricted so it was not used during this work.

3.1.3 The trap and the electron beam

The shape of the potential well at the central drift tube is mainly determined by the electron beam radius. The Brillouin radius of the electron beam,

$$r_B = \sqrt{\frac{m_e I}{\pi \varepsilon_0 v e B^2}}, \tag{3.1}$$

is only valid under the idealized conditions of a cathode temperature $T_c = 0$ K, and no magnetic field B_c at the cathode. In equation (3.1), I is the current of the beam, v the axial electron velocity, and B the magnetic field strength at the trap center. Under realistic

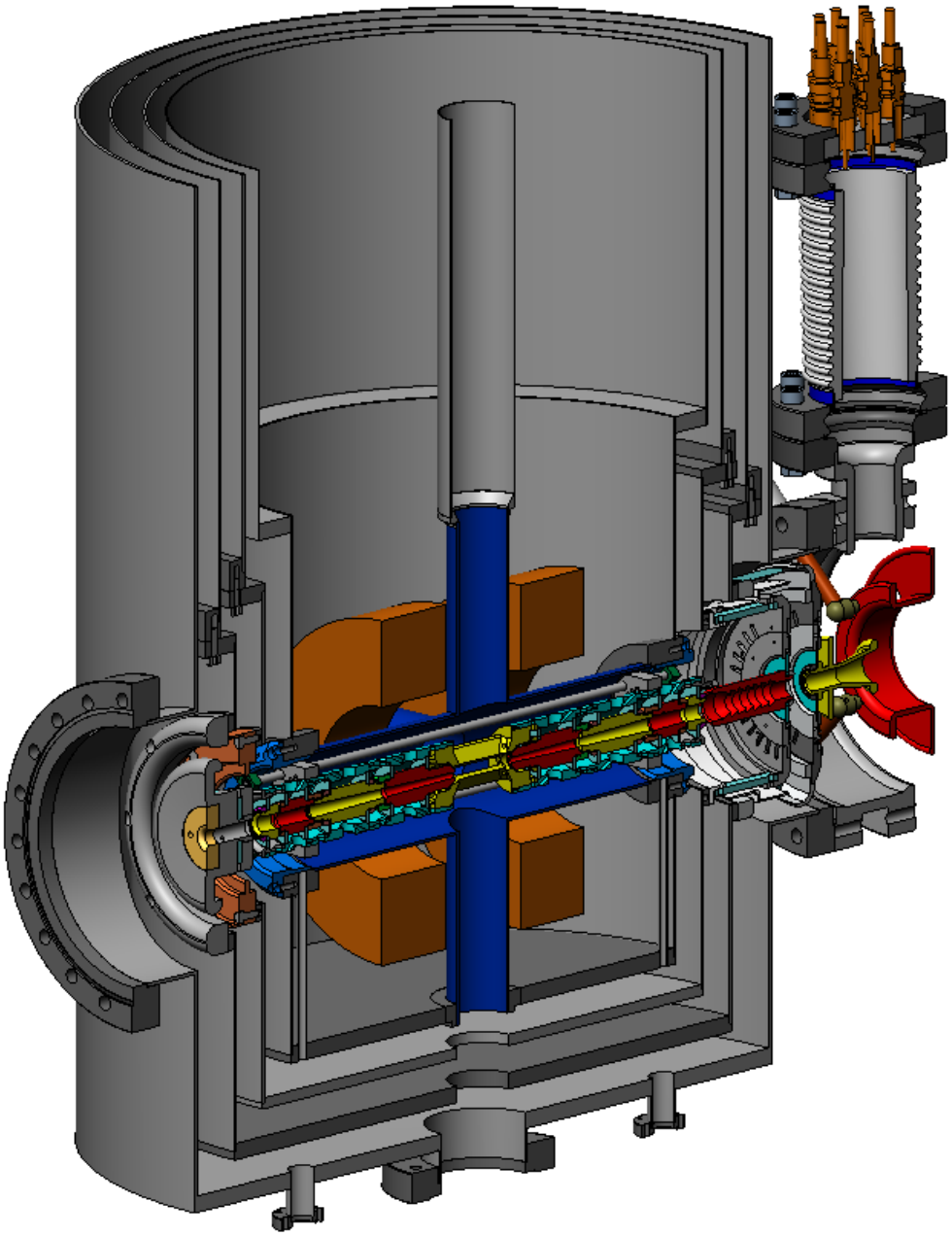

Fig. 3.4 Cross section of the central trapping region of the HD-EBIT. The electron beam travels from left to right through the drift tubes that here are colored alternately yellow and red. The central six-way cross (blue) allows for observation of the ion cloud and injection of particles. The drift tubes are connected to power supplies via the vacuum feedthroughs at the top right of the figure. The superconducting coils (orange) are mounted in the liquid helium vessel that is surrounded by two cooled heat shields.

conditions in an EBIT, T_c and B_c are not zero. The approximations of Herrmann [96] have proven to realistically take this into account [97, 98]. It is defined as the radius of the cylinder containing 80% of the electrons of the beam, and can be calculated by

$$r_H = r_B \sqrt{\frac{1}{2} + \sqrt{\frac{1}{4} + \frac{8 m_e k_B T_c r_c^2}{e^2 B^2 r_B^4} + \frac{B_c^2 r_c^4}{B^2 r_B^4}}}. \tag{3.2}$$

The Herrmann radius is approximately 25 µm under the following conditions: T_c =1450 K, B_c = 0.10 T, B =8.00 T, cathode diameter r_c =1.70 mm, I =40 mA, and electron beam energy E_e =400 eV. These values are similar to the settings used for the measurements presented in this work. The constants in equation (3.2) are the Boltzmann constant k_B, the electric constant ε_0, the electron mass m_e, and the electron charge e. The radius of the ion cloud depends on the shape of the trapping potential as well as on parameters such as its charge state distribution and temperature; radii up to 200 µm haven been observed [99, 100].

To estimate the radial potential in the trap the electron beam can be approximated by an infinitely long tube with a homogeneous charge density

$$\rho = \frac{I}{\pi v r_H^2}. \tag{3.3}$$

By employing Gauss his flux theorem and considering the boundary conditions the radial potential is obtained by

$$\begin{aligned} \phi(r) &= \frac{\rho}{2\pi\varepsilon_0} \ln\left(\frac{r}{r_{\mathrm{DT9}}}\right) + U_{\mathrm{DT9}}, && r_H \le r \le r_{\mathrm{DT9}} \\ \phi(r) &= \frac{\rho}{2\pi\varepsilon_0} \left(\frac{r^2}{2r_H^2} - \frac{1}{2} - \ln\left(\frac{r}{r_{\mathrm{DT9}}}\right)\right) + U_{\mathrm{DT9}}, && r \le r_H. \end{aligned} \tag{3.4}$$

A derivation of this equation can be found for example in [101]. In Fig. 3.5 the radial potential is shown for the parameters that were typically used during the iridium measurements. Often the electron beam energy is estimated by

$$\begin{aligned} E_e &= eU_{\mathrm{acc}} \\ &= e(-U_c + U_{\mathrm{DT9}}). \end{aligned} \tag{3.5}$$

That is, the potential difference between the cathode and central drift tube. But as Fig. 3.5 shows, the potential at the trap center is significantly changed by the space charge of the electron beam itself. Additionally, the space charge of the ion cloud contributes to the total

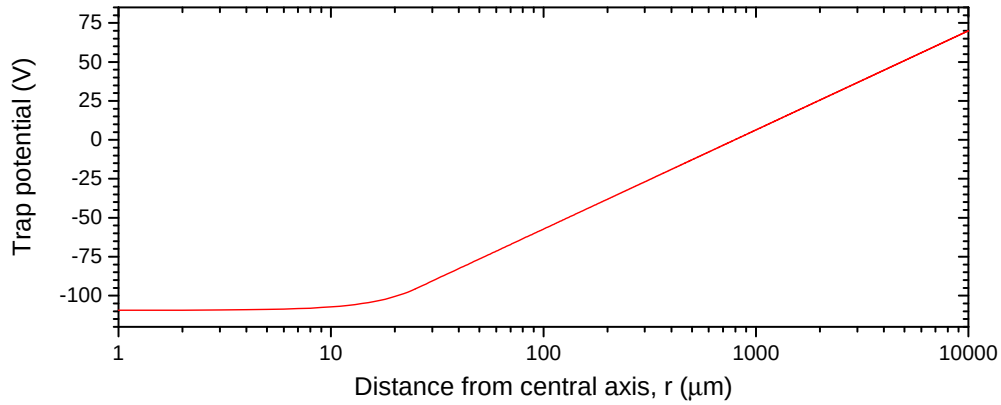

Fig. 3.5 Radial potential at DT9 according to equation (3.4). The parameters were chosen to be similar to the experimental settings used during the spectroscopy of Ir^{17+} at the HD-EBIT: $I = 40$mA, $E_e = 400$eV, $U_{\mathrm{DT9}} = 70$V, and $r_H = 25\,\mu$m.

potential at the trap center. To determine the true electron beam energy, these effects need to be taken into account.

Ions in the trap are constantly heated by electron impact, causing some ions to gain enough energy to overcome the trapping potential; thereby reducing the temperature of the remaining ions. The ions most likely to evaporate out of the trap are the those with the lowest charge state q, since the trapping strength scales linearly with q. Thus, this evaporative cooling can be enhanced by injecting an element that intrinsically cannot reach a high charge state, i.e., a low Z element [102]. Further enhancement of the cooling can be achieved by lowering the trapping potential so that only the coolest, high q, ions remain in the trap [103]. In this manner, ion cloud temperatures in the order of 200 eV/k_b can be achieved. An order of magnitude lower temperatures have been shown to be possible when applying forced evaporative cooling and temporarily switching off the electron beam [104].

3.1.4 The electron collector

After the electrons traverse the drift tubes, the electrons are dumped on the inner surface of the collector, see Fig. 3.6. The collector is directly connected to the same electrical ground as the cathode power supply so that the circuit is closed. To prevent electrons from passing though the collector, an additional electrode at a potential more negative than that of the cathode is installed. This so-called extractor can also serve to enhance the extraction of ions from the EBIT when required. An electromagnet around the inner tube of the collector is used to apply a magnetic field such that the electron beam is sufficiently divergent to hit the inner wall instead of being reflected back to the trapping region. The heat produced by the

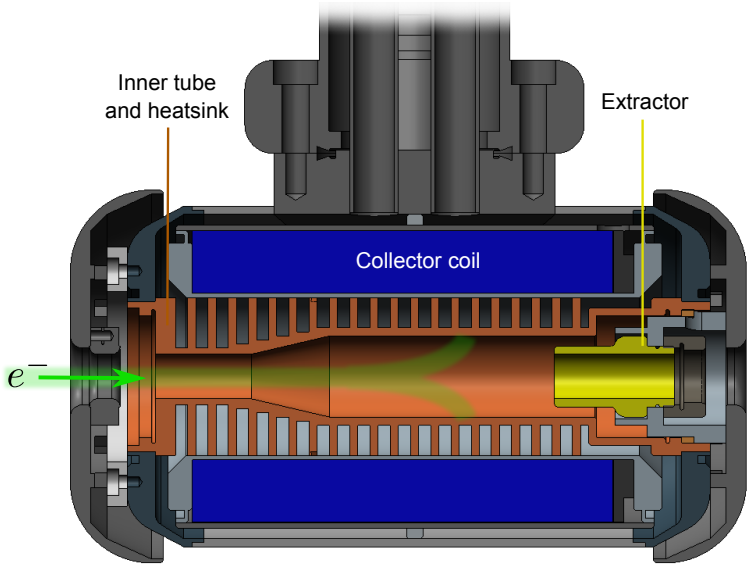

Fig. 3.6 Cross section of the electron collector of the HD-EBIT. The electron beam (green) diverges strongly in the magnetic field of to the magnet coil (blue) and subsequently hits the wall of the inner tube (orange). The extractor (yellow) is biased to a sufficiently negative potential to prevent the electrons from passing though the collector.

electrons hitting the collector, and the heat from the collector coil, is transported away by cooling water.

3.1.5 The injection system

In this work, the preferred method for injecting particles into the EBIT was by crossing a molecular beam with the electron beam at the trap center. Substances that are gaseous or volatile at room temperature are most suited for this type of injection. For the injection of the chemical elements investigated in this work, suitable volatile compounds were found, see table 3.1. The binding energies of molecules are at the level of a few eV, so their bonds are easily broken by the electron beam. In addition to the elements of interest, the compounds also contain hydrogen, carbon, and oxygen. This is advantageous since the light elements enhance evaporative cooling. At the HD-EBIT, a gas dosing valve was used to regulate the flow of gas into the first stage of the injection system, the pressure at this stage was typically in the 10^{-7} mbar range. The nozzle of the valve was aimed at a small aperture (a few mm^2) that leads to the second injection stage, where the pressure is approximately an order of magnitude lower. The next aperture leads to the central trapping region. The nozzle of the valve, both apertures, and the trap center are all in line to cross the molecular beam with the electron beam.

Table 3.1 Properties of the volatile organometals used to inject a range of chemical elements [109]. BP = boiling point, S = sublimation, VP = vapor pressure, MP = melting point, all for the given temperature. The compounds for Mo, Pr, and Pb require heating of the source to achieve a suitable injection pressure [110]. Heating of the other compounds was not necessary and in some case even decomposed the compound. The Sm compounds theoretically have suitable properties, but injection could not be proven.

Element	Molecule	CAS number	Property
Iron, Fe	$Fe(CO)_5$	13463-40-6	VP 46 mbar, 25 °C
Molybdenum, Mo	$((C_2H_5)_\times C_6H_6\eta_\times)_2Mo$	32877-00-2	BP 150-170 °C, 1.3 mbar
Praseodymium, Pr	$Pr(C_{11}H_{19}O_2)_3$	15492-48-5	S 150 °C, 0.13 mbar
Samarium, Sm	$Sm(NO_3)_3)\cdot 6H_2O$	13759-83-6	Ineffective
Samarium, Sm	$Sm(OCH(CH_3)_2)_3$	3504-40-3	Ineffective
Tungsten, W	$W(CO)_6$	14040-11-0	VP 1.6 mbar, 67 °C
Rhenium, Re	$C_8H_5Re\ (CO)_3$	12079-73-1	unknown
Osmium, Os	$(C_5H_5)_2Os$	1273-81-0	MP 226-228 °C
Iridium, Ir	$(C_6H_7)(C_8H_{12})Ir$	132644-88-3	BP 100 °C, 0.04 mbar
Platinum, Pt	$C_5H_4CH_3Pt(CH_3)_3$	94442-22-5	S 23 °C, 0.071 mbar
Lead, Pb	$Pb(C_{11}H_{19}O_2)_2$	21319-43-7	S 134 °C, 0.13 mbar

Several other methods to inject particles into EBITs are used in laboratories around the world. If a volatile compound is not available a Knudsen cell can be used to produce a vapor of the element of interest [105]. A more common method is to use a metal vapor vacuum arc (MEVVA) ion source or laser ion source to inject ions from the collector side into the trap center [106, 107]. For highly efficient injection of rare isotopes or of unstable nuclei a wire probe injector has been demonstrated to be suitable [108].

3.2 Spectroscopic instrumentation

In this work, grating spectrometers were employed to measure the wavelengths of fluorescence light. In such a device, light passing through the entrance slit or from an otherwise well-defined source is dispersed based on its wavelengths by a diffraction grating. A part of the resulting spectrum is then recorded by a light sensitive device. The principle of operation of the diffraction gratings and CCD cameras employed in this work are described next.

3.2.1 Blazed diffraction gratings

A reflective diffraction grating has a periodic groove structure such that each groove acts as a point source when illuminated. The conditions for constructive interference of light with wavelength λ from these virtual point sources occurs when the grating equation is satisfied [111],

$$\sin\alpha + \sin\beta = \frac{n\lambda}{d}. \tag{3.6}$$

Here, the angles α and β correspond to the angle of incidence and angle of reflection with respect to the grating normal. The integer number n is the diffraction order, and the width of a single groove is given by d.

Blazed gratings are optimized for a certain wavelength, as illustrated in Fig. 3.7. In first order, the light is reflected at the angle β with respect to the grating normal as required by the grating equation. With respect to the blaze normal the light is reflected at an angle of $\phi_o = \theta_b + \beta$. When this is equal to the angle of incidence with respect to the blaze normal ϕ_i, the conditions for specular reflection from the groove face is satisfied, and the reflection is optimal. The condition

$$\phi_o = \phi_i \Rightarrow \theta_b + \beta = \alpha - \theta_b \tag{3.7}$$

together with the grating equation (3.6) can only be satisfied for a specific wavelength; which is called the blaze wavelength.

How well spectral lines can be resolved with a grating depends on the difference in angle of reflection for two different wavelengths; this property is called the dispersion. The dispersion relation can be obtained by differentiating equation (3.6) with respect to λ for a fixed angle of incidence α

$$\frac{\partial\beta}{\partial\lambda} = \frac{n}{d\cos\beta}. \tag{3.8}$$

This equation shows that a better dispersion is achieved by increasing the groove density $k = d^{-1}$, or by using a higher diffraction order. It also shows that for larger angles of reflection, i.e. for lower wavelengths, the dispersion gets worse.

In many spectrometer types, focusing elements are needed to image the entrance slit on the detector plane. This makes the simple angular dependence on the wavelength from the grating equation more complex. The relation between the wavelength and the position p on

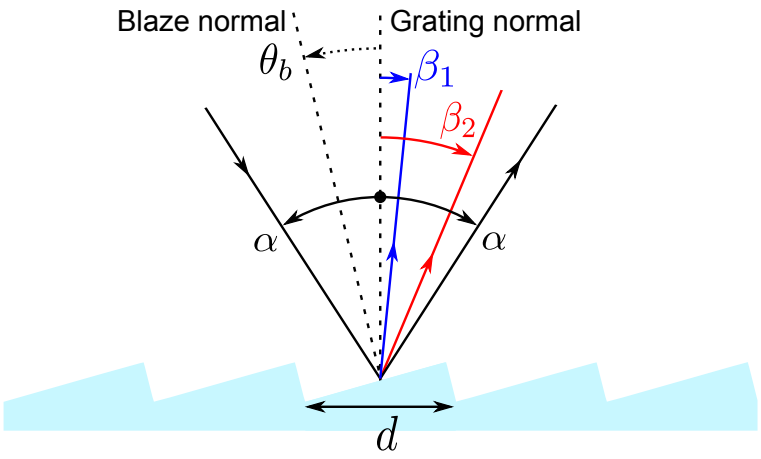

Fig. 3.7 Schematic drawing of a reflective, blazed diffraction grating. Due to the choice of blaze angle θ_b, it is as if the blue ray reflected under angle β_1, undergoes specular reflection from the groove face. This makes the diffraction of the blue ray highly efficient.

the detector can be parametrized by partial differentiation of the inverse dispersion relation,

$$\frac{\partial \lambda}{\partial p} = \frac{\partial \lambda}{\partial \beta}\frac{\partial \beta}{\partial p} = \frac{d\cos\beta(p)}{nL(p)}. \tag{3.9}$$

Here, $L(p)$ is the focal distance of the setup. Integrating the equation gives the wavelength for any given position on the detector

$$\lambda(p) = \lambda_0 + \int_0^p \frac{d\cos\beta(p')}{nL(p')}\mathrm{d}p'. \tag{3.10}$$

In practice, this is approximated with a polynomial to the highest statistically significant order. Spectral lines with known wavelengths are used to determine the coefficients of the polynomial.

3.2.2 CCD cameras

In the year 1969 the charge coupled device (CCD) was invented, in 2009 CCDs were so ubiquitous that its inventors Willard S. Boyle and George E. Smith were awarded that year's Nobel price in physics [112, 113]. Over years of innovation, CCDs have become more efficient and less prone to noise. That, combined with their spatial resolving power, make CCDs ideal for usage in spectrometers.

The conversion of photons to charge in a CCD is due to the photoelectric effect in a semiconductor. As in a photodiode, photons hitting the depletion zone at a p-n junction with

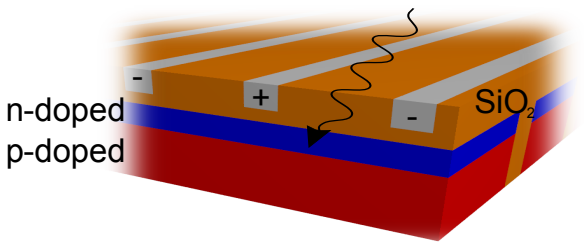

Fig. 3.8 Principle of a basic front-illuminated CCD chip. A photon hitting the p-n junction produces an electron-hole pair. free charge carrier is capacitively coupled and localized to the nearest biased metal strip (gray). SiO_2 barriers are in place to prevent electrical contact to the metal strip and to prevent movement of the free electron parallel to the strip. In modern back-illuminated CCDs, the image is projected on the p-doped side of the chip; so that loses due to the metal strips are eliminated. However, for this the p-doped substrate needs to be extremely thin.

sufficient energy create electron-hole pairs. In a CCD, the free charge carriers are stored in potential wells that define the single pixels. The potential wells are induced by applying potentials of opposite sign on neighboring metal strips embedded in an isolator on the surface of the p-n junction, see Fig. 3.8. At read out, the potentials on the metal strips are stepwise inverted, so that the free charge carriers are moved to the next row of pixels. This continues until the charge carriers reach the edge of the CCD. There the current due to the free charge carriers can be read out. It is subsequently amplified and converted to a digital signal by an analog-to-digital converter.

Several forms of noise are common in CCDs. Thermal noise is caused by the creation of electron-hole pairs due to thermal excitation in the semiconductor. By cooling the CCD this type of noise can be reduced. During the read out process some additional noise is added to the signal. Furthermore, when charged particles hit a CCD, excess electron-hole pairs are created. This corrupts the signal at the involved pixels. The charged particles originate mostly from stray muons that are produced when a cosmic ray hits the Earth atmosphere. During the data analysis, the corrupted pixels need to be identified and discarded from further analysis, a process also know as removing cosmics.

Chapter 4

Spectroscopy of Pm-like and Nd-like systems in the extreme ultra-violet regime

The clearest way into the Universe is through a forest wilderness.

— John Muir

The elements in the alkali group of the periodic table have been subject to extensive study because of their relatively simple electronic structure with a single ns electron outside closed shells. For the same reason, singly charged ions of the alkaline earth metals are the main subject of many experiments in atomic physics. In the realm of highly charged ions (HCI) too there is considerable interest in alkali-like ions. For example, the $2s$ - $2p$ transition in Li-like Pr^{56+} was recently studied as a means to access nuclear properties through the level splittings induced by the nuclear magnetic field [43]. Also, the transitions in Li-like ions have been extensively studied for their quantum electrodynamic (QED) contributions, see for example Epp *et al.* [63] and references therein. The $3s$ - $3p$ transitions of a wide range of Na-like ions were investigated in the work of Gillapsy *et al.* [44]. The reordering of levels due to the dominance of the Coulomb interaction in HCI gives Ni-like ions with 28 bound electrons a closed shell configuration. Hence, the next alkali-like series for HCI is the Cu-like sequence. Corresponding $4s$ - $4p$ transitions were investigated for a range of ions by Gillapsy *et al.* among other groups [44]. The $4f$–$5s$ level crossing gives HCI of the Pm-like ($Z = 61$) iso-electronic sequence configurations with a single $5s$ electron above a closed $n = 4$ shell. Curtis and Ellis were the first to publish on their theoretical investigation of Pm-like HCI [46].

Initially, it was suggested that the $5s\,^2S_{1/2}$ - $5p\,^2P_{1/2}$ and $5s\,^2S_{1/2}$ - $5p\,^2P_{3/2}$ doublet could be used for diagnostic purposes of plasmas. Many nuclear fusion research facilities employ divertors and other plasma facing components made of tungsten, causing small amounts of sputtered tungsten to leak into the plasma. Current examples are ITER and Wendelstein 7-X [114, 115]. From the observation of the $5s$ - $5p$ transitions of Pm-like W^{13+} in the plasma, properties such as the plasma temperature, amount of contamination, and density of the impurities can be deduced [116]. Controlling the impurities is important, since transitions of W in the x-ray region can radiate away significant amounts of energy [117, 118].

Since the publication by Curtis and Ellis much effort has been done to observe the $5s$ - $5p$ transitions in a variety of Pm-like ions. A series of Pm-like ion species were studied using the beam-foil technique at the Bochem Dynamitron-Tandem Laboratorium [119]. The heaviest Pm-like ion investigated was U^{31+} at the TEXT tokamak, where the broad charge state distribution made the interpretation of the spectra especially difficult [120]. At the Shanghai EBIT, and more recently at the Tokyo-EBIT, the recorded spectra were less cluttered because in EBITs the charge state distribution can be better tuned to a specific charge state [121, 79]. Still, no definitive identification of $5s$ - $5p$ transitions was made due to the dense forest of lines. Tentative claims that were made are summarized in table 4.5 near the end of this chapter.

To interpret the dense spectra, it is necessary to turn to theory. On this front much progress has been made: Originally it was thought that in Pm-like W^{13+} the ground state would be $5s\,^2S_{1/2}$. State-of-the-art calculations that are fully relativistic and take into account more configurations predict that only from Pm-like Pt^{17+} onward the $5s\,^2S_{1/2}$ configuration is the ground state [122, 123, 72]. This is illustrated in Fig. 4.1. The uncertainty of the latest predictions is estimated to be at the level of 1% for the energy levels and at the level of 2% - 20% for the transition rates.

Recent proposals to use HCI for metrology purposes sparked a renewed interest in, among others, the Pm-like systems [124]. The Nd-like ion Ir^{17+} is even more interesting for fundamental research since it features transitions that are highly sensitive to variation of the fine-structure constant. Those transitions are in the optical range, which is covered in chapter 6. In order to interpret the complex electronic structure of Ir^{17+} the EUV spectra provide essential information. They also provide additional data to benchmark atomic theory for atomic systems with complex correlations between many electrons in an open shell.

In this chapter, measurements of the EUV spectra of the Pm-like systems Re^{14+}, Os^{15+}, Ir^{16+}, and Pt^{17+} are presented. The obtained spectra are compared to synthetic spectra produced by a collisional radiative model (CRM) of the Flexible Atomic Code (FAC). Based on this comparison, identifications of the lines was possible. The measured wavelengths

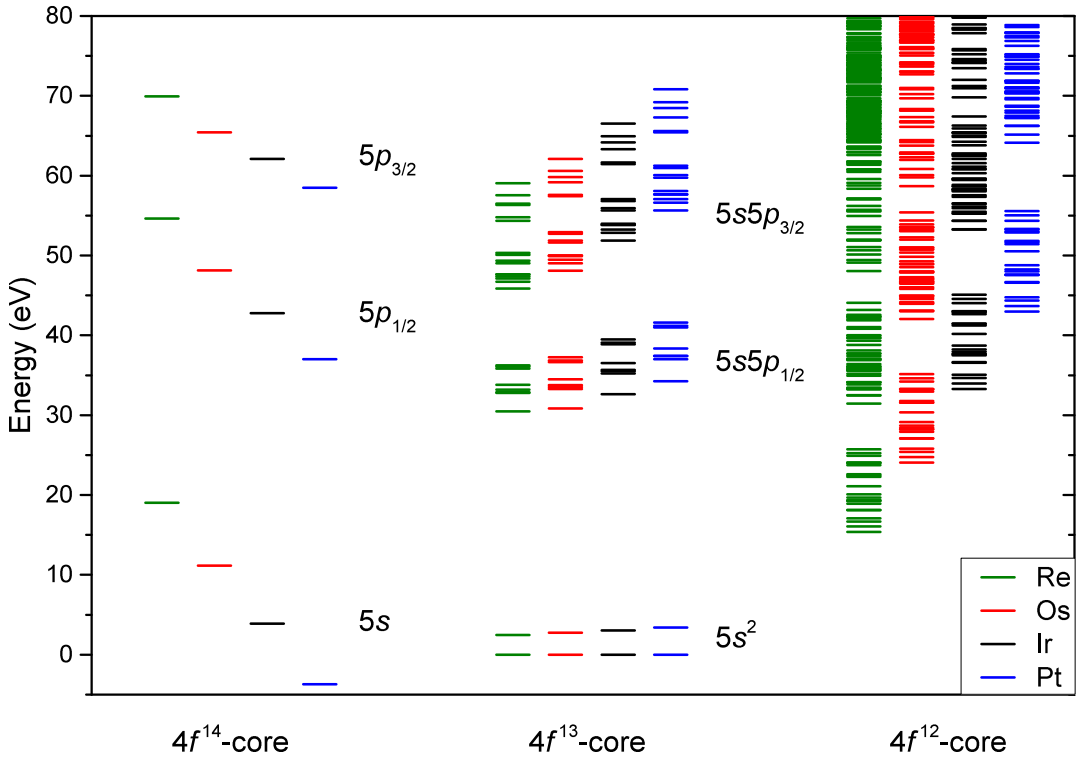

Fig. 4.1 Level scheme for Pm-like Re, Os, Ir, and Pt as calculated within the CIDFS framework by N.S. Oreshkina [72]. The lower $4f^{13}5s^2$ level of the each element is arbitrarily fixed to 0 eV; all other energies are relative to that reference. The strongest transitions are expected to take place between configurations with the same $4f^k$-core, since other transitions require large changes of the total angular momentum, J.

were compared to predictions. Moreover, EUV spectra of the Sm-like and Nd-like charge states were also obtained.

4.1 Vacuum ultra-violet spectrometer

To observe the EUV fluorescence light emitted by the ions, a spectrometer developed by T. M. Baumann was employed in this work [125]. Its main components are a reflective grating to disperse the light, and a camera to record the spectrum. The components are mounted in a vacuum chamber that was connected to the vacuum of the HD-EBIT. Windowless operation in vacuum was necessary due to the strong absorption of EUV light by any material. A cross section of the setup is shown in Fig. 4.2a.

The grating is concave, with a radius of curvature $R = 13\,450$ mm, so that the light from the source is focused onto the detector without the need for additional refractive elements.

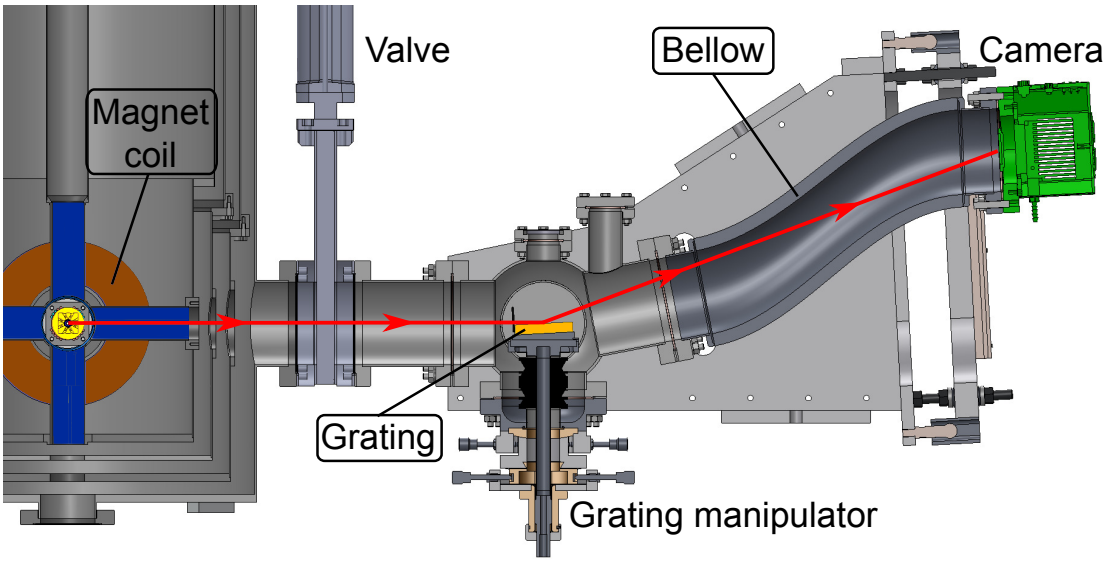

(a) Cross section of the EUV spectrometer attached to the HD-EBIT. The path of a ray of light (depicted in red for visibility) traveling from the ion cloud at the center of the central drift tube (yellow) to the camera is shown. The grating (orange) is mounted on a manipulator to fine tune its position. A slit is installed in front of the grating to reduce the amount of stray light reaching the camera. Important mechanical components that are also shown: a flexible bellow to allow repositioning of the camera, and a valve to separate the vacuum system of the EBIT and spectrometer if necessary.

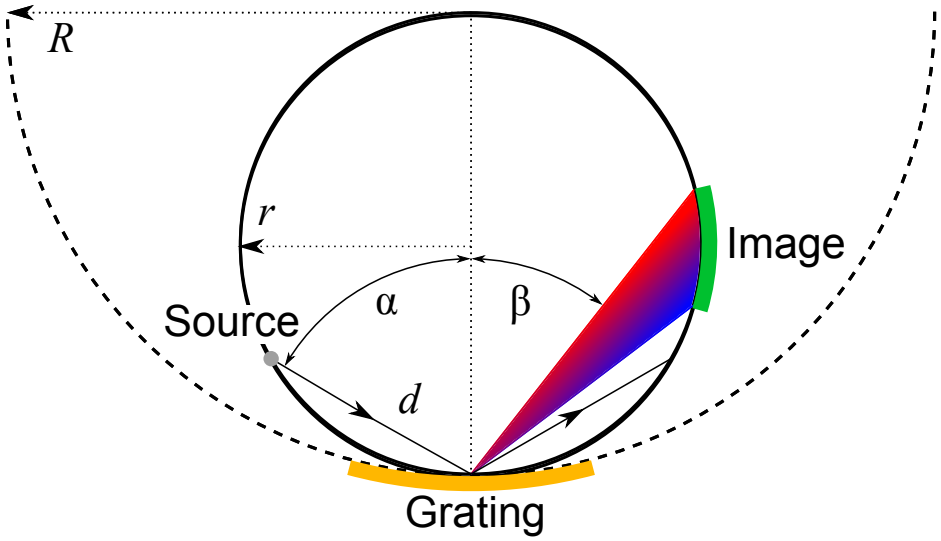

(b) Schematic depiction of a spectrometer in Rowland configuration. Light from the source point (gray) on the Rowland circle is reflected by the grating (orange), the zeroth order reflection is shown as the black line with arrows. (Not to scale).

Fig. 4.2 Experimental setup.

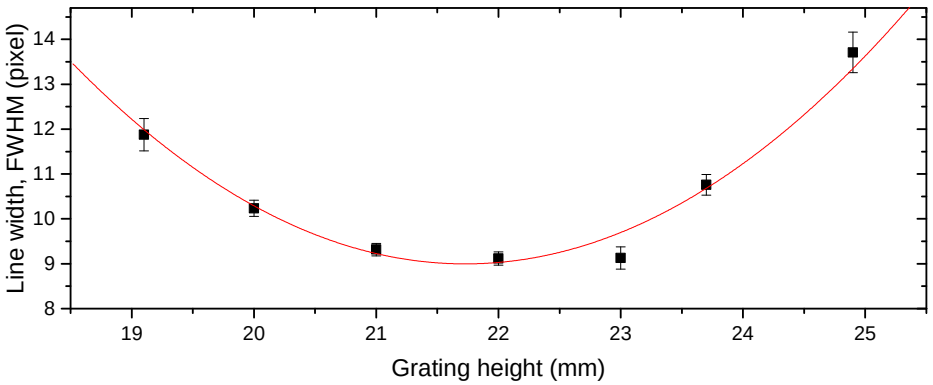

Fig. 4.3 To optimize the resolving power of the spectrometer, the line width of the Ir^{16+} line at approximately 19.8 nm was measured for several grating heights. The red line is a fit of a parabolic function to the data to determine the position where the line width is minimal, which was found to be at 21.7 mm. The actual achieved minimal line width was lower than indicated here, since the investigated line was later found to be a blend of two lines. However, the iron lines that were used for the calibration are not blends and have line widths of 7 pixels. This gives a resolving power of $\lambda/\Delta\lambda \approx 600$.

The typical construction is such that the light source, grating, and camera are all on a circle with a radius $r = R/2$, which is known as the Rowland circle [126]. Any point source on the Rowland circle is focused onto another point on the Rowland circle, refer to Fig. 4.2b. The geometry can be fine-tuned by positioning the grating using the grating manipulator, the effect of varying the grating height is demonstrated in Fig 4.3.

A key point in this instrument is the use of a variable-groove-density grating, capable of producing a nearly flat focal plane within a range of wavelengths. In this manner, the image of the ion cloud can be focused over nearly the whole CCD. Because of this property, these gratings are known as flat-field gratings. The grating installed in the EUV spectrometer was manufactured by Hitachi, and is optimized for usage in the range from 5 nm to 30 nm [127, 128]. Important design parameters are summarized in table 4.1. Under ideal conditions, the resolving power of the spectrometer is approximately λ / $\Delta\lambda \approx 1800$ at 20 nm. This is calculated assuming a source size, i.e. ion cloud diameter, of 50 µm. The grating is used in grazing incidence (87°), since reflectivity in the EUV range is otherwise very low [111]. The optical acceptance of the spectrometer is consequently relatively small at $4.6 \cdot 10^{-4}$ sr. For improved reflectivity the grating is coated with gold, which has a refractive index of $n_{gold} \approx 0.85$ at 20 nm [129].

The grating disperses the light in the range of 5 nm to 30 nm over a height of of approximately 100 mm at the focal plane. Since the CCD chip has a height of 27 mm, only a limited region can be recorded per acquisition. To allow recording of the whole spectral range of the

Table 4.1 Properties of the grating employed in the EUV spectrometer.

Property	Value
Average line density	1200 grooves/mm
Blaze	9 nm
α	87°
R	13 450 mm
d	564 mm

grating, the camera is mounted on a linear manipulator and attached to the grating vacuum chamber by a flexible bellow, refer to Fig. 4.2a.

The CCD camera (Andor DO486) consists of 2048×2048 pixels on a $27.6 \times 27.6\,\mathrm{mm}^2$ chip. It is cooled by a multi-stage Peltier element, making it possible to reach temperatures down to $-95\,^{\circ}\mathrm{C}$, thereby reducing the dark current to $N_{DC} \approx 0.36$ electrons / pixel hour. The camera was operated at the highest gain where 1 count equals 0.7 e^-. At the set read-out speed of 31 kHz the read-out noise is $N_{\mathrm{RO}} \approx 2.5$electrons. Unfortunately, binning of the pixels was only possible along the dispersive axis. Read-out noise reduction by binning was thus not an option, since it would have resulted in a loss of resolving power.

4.2 Calibration

Accurate calibration of the spectrometer requires measuring a series of lines with well-known wavelengths. The setup did not allow for external feeding in of calibration light, but some HCI that can be produced in the HD-EBIT have well-known lines. The advantage is that the calibration light source is at exactly the same position as the ions under investigation if the EBIT electron beam alignment is not changed. This eliminates errors that would occur when the calibration light and the investigated light do not follow the same path.

Iron ions of the charge states from 9+ to 14+ have a number of lines around 20 nm that can be well resolved and whose wavelengths are known at the $4 \cdot 10^{-4}$ nm level, see Fig. 4.4 [39]. The ionization potential of the iron ions used here is in the range 250 to 450 eV, which is the same range required for the production of the Pm-like Re, Os, Ir, and Pt ions. Therefore, the operating parameters of the EBIT need very little re-adjustment and the position of the ion cloud will not be affected. For this method of calibration, iron atoms needed to be introduced into the trap region. The compound $\mathrm{Fe(CO)_5}$ has been used to inject iron atoms into EBITs before [64]. However, switching between injection sources took at

least one hour, so calibration spectra were typically only recorded at the beginning of a measurement sequence.

Variations of environmental conditions such as temperature influence the alignment of the setup. To quantize these effects, a measurement with no changes to the EBIT and spectrometer parameters was performed for 26 hours. Approximately every half hour a spectrum was acquired around 20 nm, with the EBIT tuned to produce Ir^{18+}. By fitting Gaussian functions to three well resolved lines the line centers were determined for each spectrum, the results are shown in Fig. 4.5. As in [130], a variation with a period of 24 hours is apparent, the amplitude of the variation is too large to be negligible. However, as will be shown later, a persistent helium line in the spectra could be used to partially correct for this variation.

Simultaneous injection of iron and iridium was also investigated to allow more regular calibrations [131]. Injection of iron and iridium compounds through a single gas dosing valve was successful, but the interpretation of the spectra was made difficult by to the increased number of lines in the spectra. Using two gas dosing valves increased the control over the injected substances, but also increased the difficulties with aligning the two nozzles of the valves. Moreover, residual gas remained up to an hour in the injection stages, thereby contaminating the ion cloud and thus increasing the time to obtain clean ion spectra.

4.3 Data analysis

Several steps were performed to generate the spectra. These were mainly executed using a program called Shiftmatrix (developed in LabVIEW by M.C. Simon) and the commercially availably software package Origin. A visualization of the steps is shown in Fig. 4.6. In the first step, the pixel rows were translated according to a parabolic function to correct for astigmatism and rotation of the camera with respect to the grating and the ion cloud,

$$x_{\text{straight}} = x_{\text{original}} + b \cdot y + c \cdot y^2. \tag{4.1}$$

The coefficients b and c were optimized to yield the smallest line widths and thereby the best resolving power for the final spectra. All the spectra were corrected using the same values for b and c so that this procedure did not lead to systematic errors. The cosmics were also removed during this step. Since the CCD chip was not binned during read-out, the signal at individual pixels did not strongly exceed the noise level. The pixels that were affected by cosmic muons however had highly increased values. Therefore it was sufficient to apply a low-pass filter for the removal of cosmics.

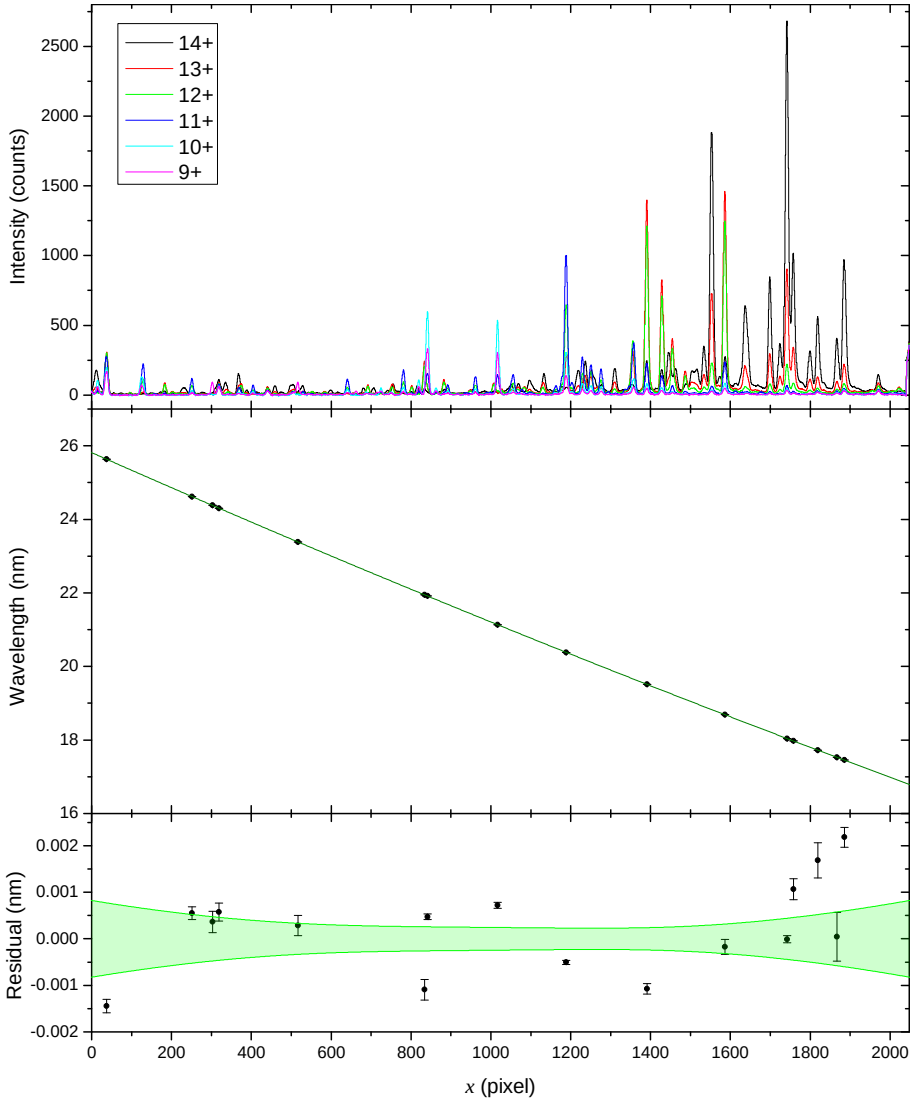

Fig. 4.4 *Top:* Spectra of several iron charge states that were used to calibrate the spectrometer. The peak centers of well resolved lines with known wavelengths were determined with Gauss fits. *Middle:* The found pixel values were plotted against the known wavelengths. The fit (green line) of a parabolic function to the data found the calibration function $\lambda(x) = 25.8136(8) - 4.797(2) \cdot 10^{-3} \cdot x + 1.922(8) \cdot 10^{-7} \cdot x^2$. *Bottom:* Residuals between the data points and the calibration function (circles). The 1-σ confidence band of the fit is shown in green, this is taken as the uncertainty due to the calibration.

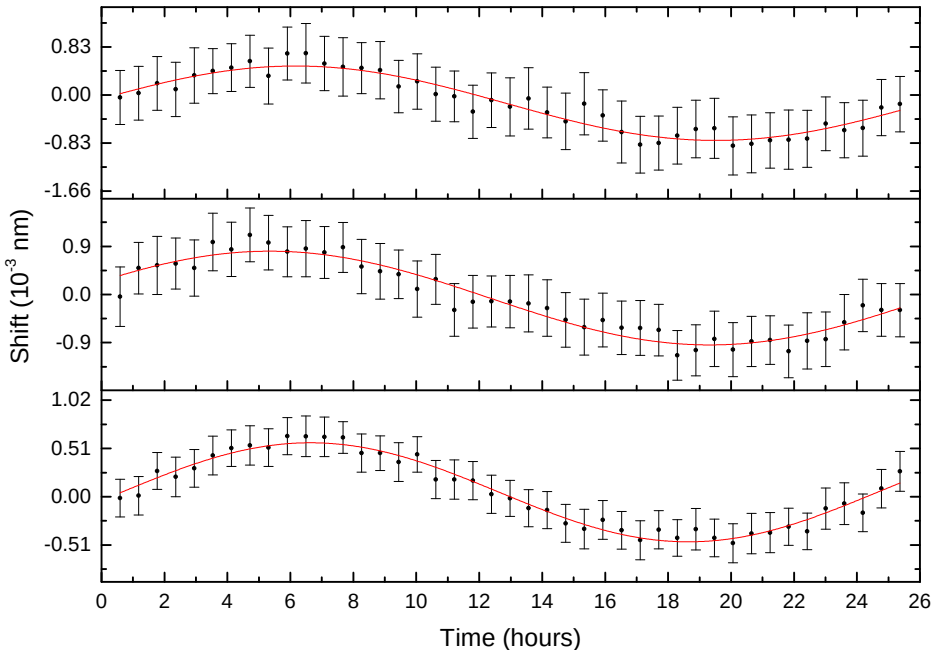

Fig. 4.5 The center of the iridium lines at 18.7721(11) nm (top), 19.6169(8) nm (middle), and 20.0852(10) nm (bottom) were measured regularly over the course of approximately 26 hours. The relative variation of the peak centers over time is shown. Daily temperature fluctuations of 1 °C were measured in the laboratory, which is sufficient to account for the observed amplitude of the wavelength fluctuation. The red line shows fits of sinusoidal functions to the data, from this the period was determined to be 24.0(4) hours and the amplitude to be $5.2(2) \cdot 10^{-4}$ nm. The data was taken on 03-09-2013 from 17:00 until 04-09-2013 at 18:30.

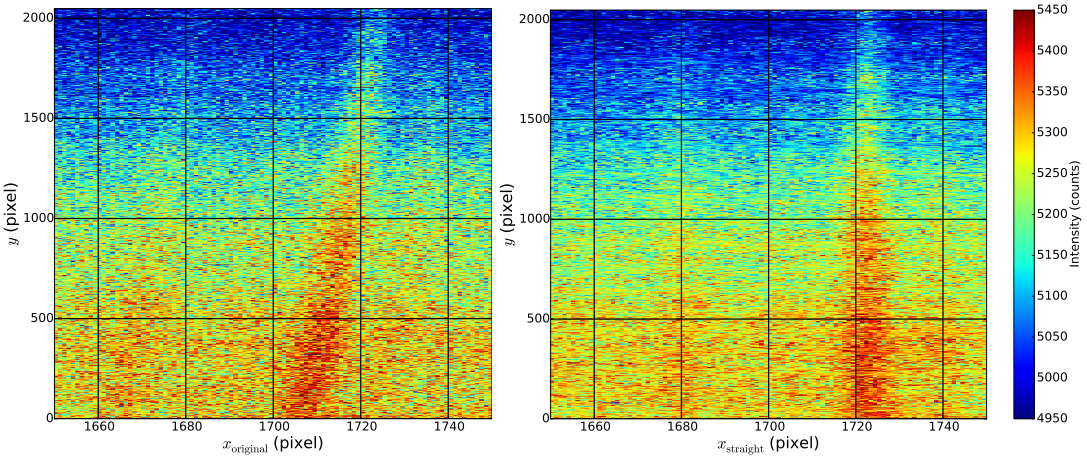

(a) Zoom of raw CCD image

(b) Straightened and cleaned CCD image

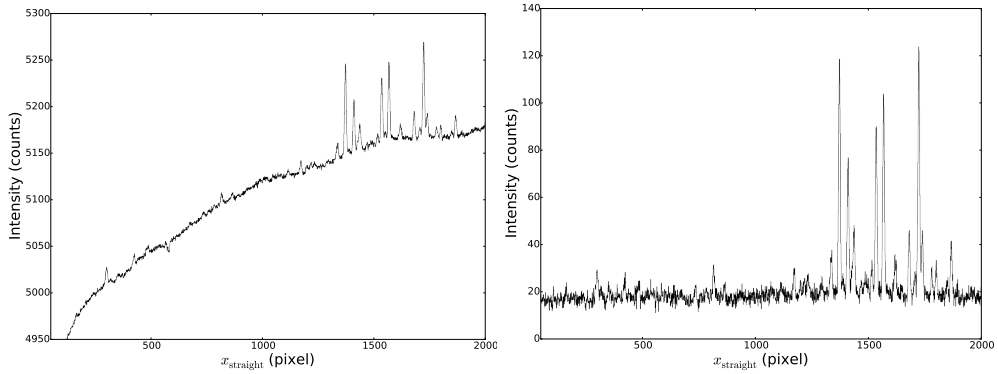

(c) Projection

(d) Projection without background

Fig. 4.6 Step by step example of the data analysis procedure. In the first step the raw data (a) was transformed so that the spectral lines are straight and the cosmics are removed, resulting in (b). The 2D image was then projected onto the x-axis to produce the spectrum (c). To produce the final spectrum (d) the background was subtracted.

In the next step the image was projected onto the dispersive axis to produce a spectrum. Stray light from the electron gun cathode reaches the camera and produces a smooth but not flat background. This was measured by taking a spectrum while the trapping potential was inverted, such that no ions remain trapped and only light due to other sources remains. This results was then subtracted from the ion spectrum to produce the final results.

4.4 EUV spectra of Re, Os, Ir, and Pt

4.4.1 Full overview of the acquired data

At the Pm-like charge state of Re, Os, Ir, and Pt ions there are 61 remaining electrons bound to the nucleus. The ionization potentials of the Pm-like and neighboring charge states are separated by maximally 50 eV, see table 4.3. Consequently, the charge state distribution does not strongly peak around one particular charge state. Hence, the spectra contained contributions from several charge states. In order to clearly determine which charge state generates which line, it was necessary to vary the electron beam energy while monitoring the line intensities. Lines that show the same intensity behavior belong to the same charge state.

At the beginning of a measurement sequence, the electron beam energy was tuned to a value well below the energy required for the production of the Pm-like charge state. The first spectrum of the sequence was taken at these settings. Subsequently, the potential on all drift tubes was increased by 10 V and the next spectrum was taken. This procedure continued until the electron beam energy was well above the ionization energy of the Pm-like charge state. At the end of the sequence, a spectrum of the background light was acquired. An overview of the results for Re, Os, Ir, and Pt can be seen in Fig. 4.7. Important experimental parameters are listed in table 4.2. Iridium spectra were taken for the whole spectral range from 5 to 30 nm [131]. However, beyond the region shown in Fig. 4.7, no strong lines were found.

As expected, there are strong similarities between the spectra of ions belonging to the same isoelectronic sequence. Characteristic lines appear at a slightly shifted wavelengths, that can be explained by the scaling with Z^2 of the binding energies. Since in this work only the spectra of the Pm-like and Nd-like sequence are of interest, those are the subject of further studies in subsequent sections. At approximately 24.3 nm a line can be seen (most noticeable in the Re spectra) that does not show a variation of intensity over the range of electron beam energies. This line could be assigned to the He^+ doublet $4p\,^2P_{1/2}$ - $1s\,^2S_{1/2}$ and $4p\,^2P_{3/2}$ - $1s\,^2S_{1/2}$ of which the wavelengths are known to be 24.302 644 454 nm and 24.302 687 696 nm [132]. It was used where possible to correct for the spectrometer shifts

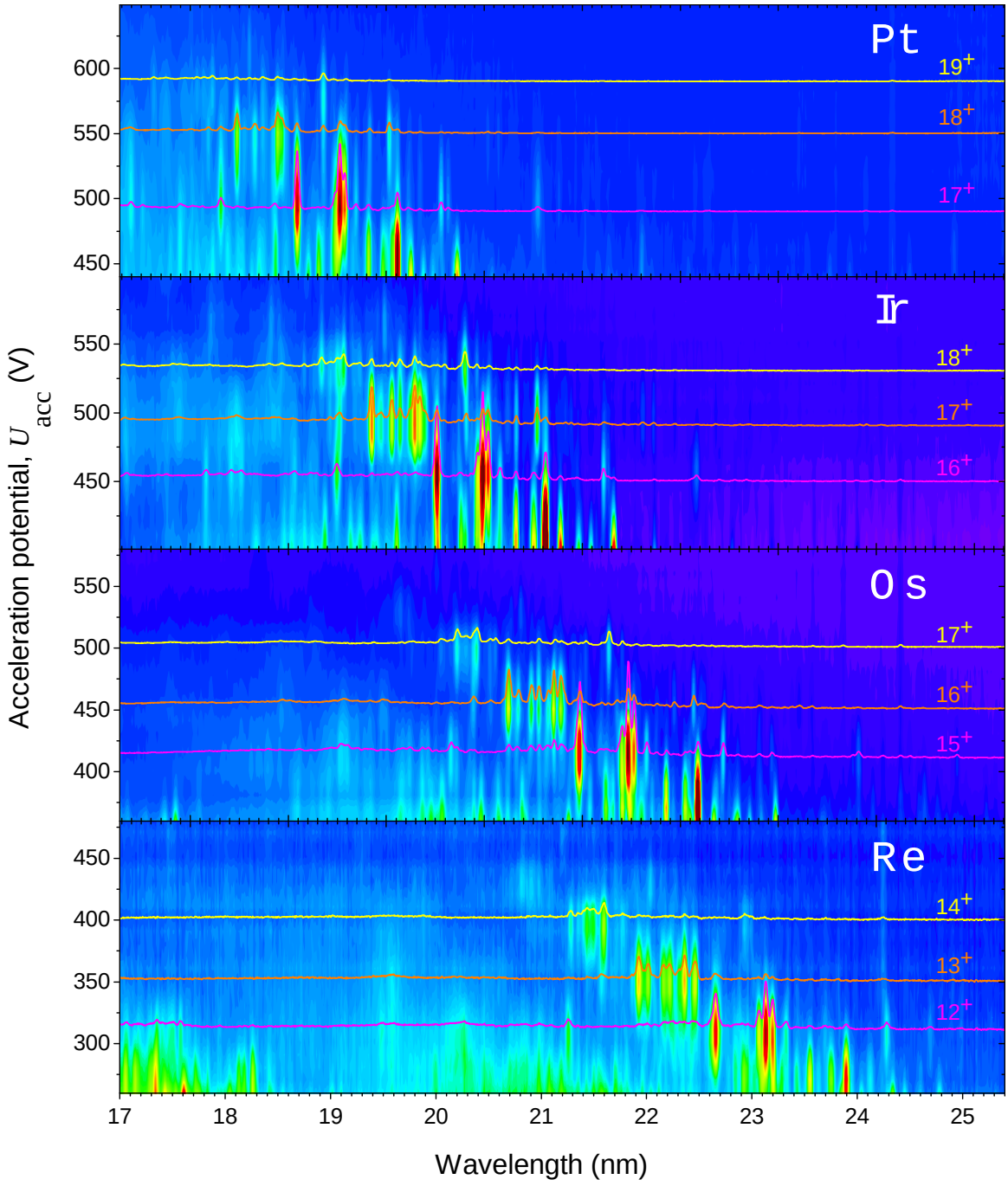

Fig. 4.7 Overview of the spectra of Re, Os, Ir, and Pt ions of the Pr-like (yellow), Nd-like (orange), and Pm-like (magenta) charge states. The experimental parameters are summarized in table 4.2. The wavelength axis is only approximate due to the linearization of the dispersion which was required to construct this figure. The identification of the charge states is explained in the next section 4.4.2.

Table 4.2 Measurement parameters. The lower current during the rhenium measurements was required to ensure a stable operation of the EBIT at the lowesr electron beam energies.

Property	Value	
	Re	Os, Ir, Pt
Acquisition time per spectrum	1640 s	1640 s
Electron beam current	10 mA	30 mA
Potentials on DT4, DT9, DT5	20, 40, 20 V	20, 70, 20 V

discussed earlier. The helium contamination of the ion cloud was most probably caused by a small leak in the liquid helium vessel of the superconducting magnet.

4.4.2 Charge state determination

The vertical axis of Fig. 4.7 represents the potential difference between the electron gun cathode and the central drift tube U_{acc}. As discussed in chapter 3.1.3, the electron beam energy is not exactly equal to the applied acceleration potential. The potential shift due to the space charge of the electrons can be as much as $5\,\mathrm{V\,mA^{-1}}$ at these low energies. Moreover, the space-charge potential due to the trapped ions affects the electron beam energy; depending on the amount of trapped ions and their charge. Since the ionization potentials of the investigated ions are energetically close to each other, it is necessary to take the space charge effects into account to determine the electron beam energy. Based on the model for the radial trap potential in chapter 3.1.3 the space charge due to the electron beam is approximately $-4.0\,\mathrm{V\,mA^{-1}}$. The uncertainty on this value is hard to estimate because the model relies on approximations that were never tested at such low electron beam energies. Moreover, the model does not take into account the effect of the space charge due to the ions.

By repeating the measurement at a low electron beam current the effect of the space charge could be reduced. Figure 4.8 shows the measurement of iridium at a low current of 10 mA. At this current, the uncertainty on the correction is estimated to be 10 V. The correction was applied to the acceleration potential. The ionization energies of the charge states were determined by the onset of fluorescence of spectral lines, and are given in table 4.3. The measured values are compared to the predicted production energies in Fig. 4.8(b). From this, the charge state identification in the iridium spectra was made. The similarities between the spectra along the iso-electronic sequence were used to identify the charge states in the Re, Os, and Pt spectra. The agreement between predicted and observed spectra, which is shown in the next section, strengthens confidence in a correct charge state identification.

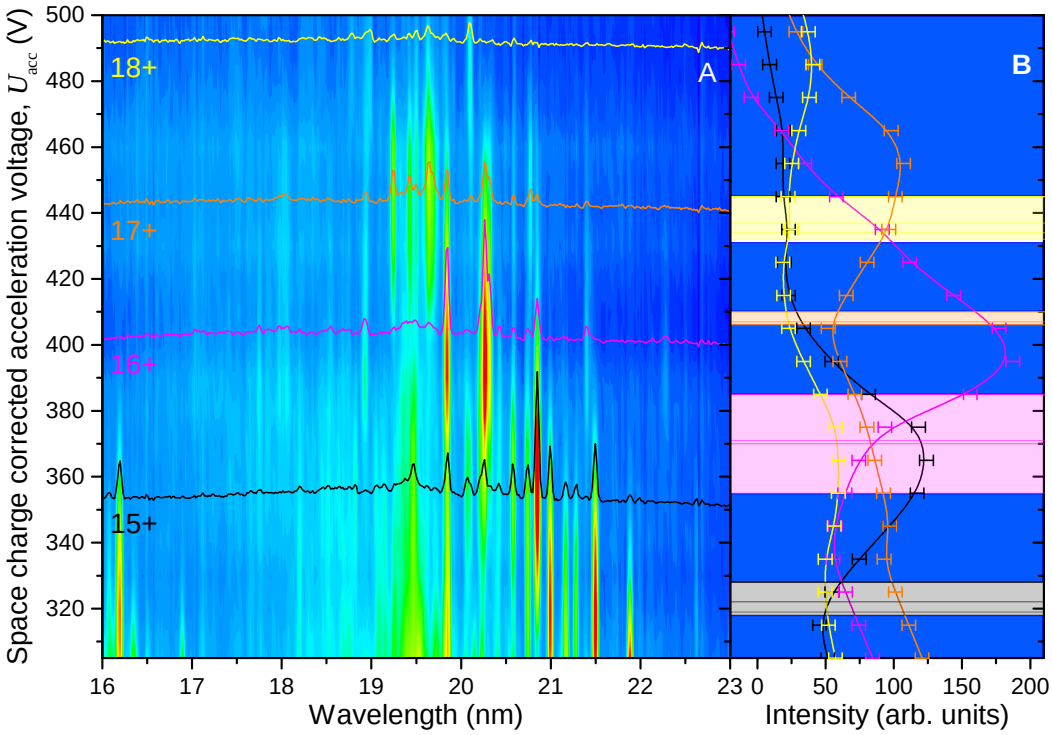

Fig. 4.8 (A) Composite, smoothed image consisting of iridium spectra obtained at 10 V intervals of the electron beam acceleration voltage U_{acc}. The electron beam current was stabilized at 10 mA, where space charge effects are small. Spectra taken at the maximum of fluorescence for each charge state are overlaid. (B) Projections of the average of the three strongest lines onto the U_{acc}-axis for different charge states; at low energies lines from other charge states contribute to the Ir^{17+} result. Smooth lines were added as guides to the eye. The strengths of the lines are maximal at the energies where the next charge state starts to be produced. Colored bands indicate the spread of the predicted production energies (cf. table 4.3); colors correspond to the overlaid spectra of (A), the blue background was added for contrast.

Table 4.3 Overview of the measured and predicted energies required to produce various charge states of iridium. All values are given in eV.

Charge state		Measured	FAC	Oreshkina [72]	Scofield [133]	Carlson [134]
Sm-like	Ir^{15+}	320(10)	319	318	322	328
Pm-like	Ir^{16+}	355(10)	370	371	385	355
Nd-like	Ir^{17+}	405(10)	407	406	410	406
Pr-like	Ir^{18+}	440(10)	434	432	437	445

4.5 Identifications of lines in the Pm-like spectra

The individual EUV spectra of Pm-like Re, Os, Ir, and Pt obtained in this work are shown in Fig 4.9. Gaussian functions were fitted to well-resolved lines that belonged to the Pm-like charge state to determine the central wavelength and peak intensity. The results are summarized in table 4.4. The use of Gaussian functions to fit the lines was motivated by the expected Doppler broadening and by the spatial distribution of the ion cloud. Furthermore, the Zeeman splitting is expected to be at the order of 10^{-4} eV, which is too small to be resolved with the employed spectrometer. The quality of the fits was monitored by verifying that the reduced χ^2 was satisfactory and by checking the fit residuals for deviations from the normal distribution. The confidence in the correctness of the fits was supported by confirming that the found line widths correspond to the resolving power of the spectrometer as determined with the Fe lines. In some cases the width of a line was found to significantly exceed the expected value. This can be caused by blended transitions with near equal transition energies and strengths. Lines with increased widths are marked in the fit results table.

Ideally, predictions for the transition energies and rates are good enough to directly identify lines by comparing them to the predictions. Based on predictions such as presented in Fig. 4.1, or as can be found in the work by M.S. Safronova *et al.* [124], a dense cluster of bright lines is to be expected in the investigated region of the Pm-like spectra. Similar predictions for the atomic structure and transition rates were obtained with FAC calculations. A synthetic spectrum based on these results is shown in Fig 4.10a. According to theory, the strongest transitions take place within the $4f^{12}$-core configurations. Transition rates are in the order of 10^{11} s^{-1} for the strongest $4f^{12}5s5p^2$ to $4f^{12}5s^25p$ transitions, whereas the $4f^{13}5p^1$ to $4f^{13}5s^1$ transitions are predicted to have a rate of approximately 10^{10} s^{-1}. Clearly, the observed spectra do not show the predicted large number of strong transitions. To explain this, the excitation processes in the EBIT and the branching ratios of the decay channels need to be taken into account using CRM.

First, the energy levels, transition rates, and electron impact (de-)excitation cross sections were calculated for the $4f^{14}5(s,p,d)$, $4f^{13}5s^2$, $4f^{13}5s5p$, $4f^{12}5s^25(p,d)$, and $4f^{12}5s5p^2$ configurations. This set of eight configurations was chosen because it reproduced the observed spectra the best. Inclusion of more configurations (up to twenty configurations in total) shifted the transitions to higher energies. The calculated transition rates and cross sections were used in the CRM calculation to numerically solve the quasi-stationary-state rate equations. For this, an electron density of 10^{11} cm^{-3} was chosen, as explained in the next section. The electron energy distribution was centered at 395 eV and set to follow a Gaussian distribution with a width of 5 eV, the distribution was cut off at 390 eV and 400 eV. The solution gives the line strengths corrected for the energy level population distribution

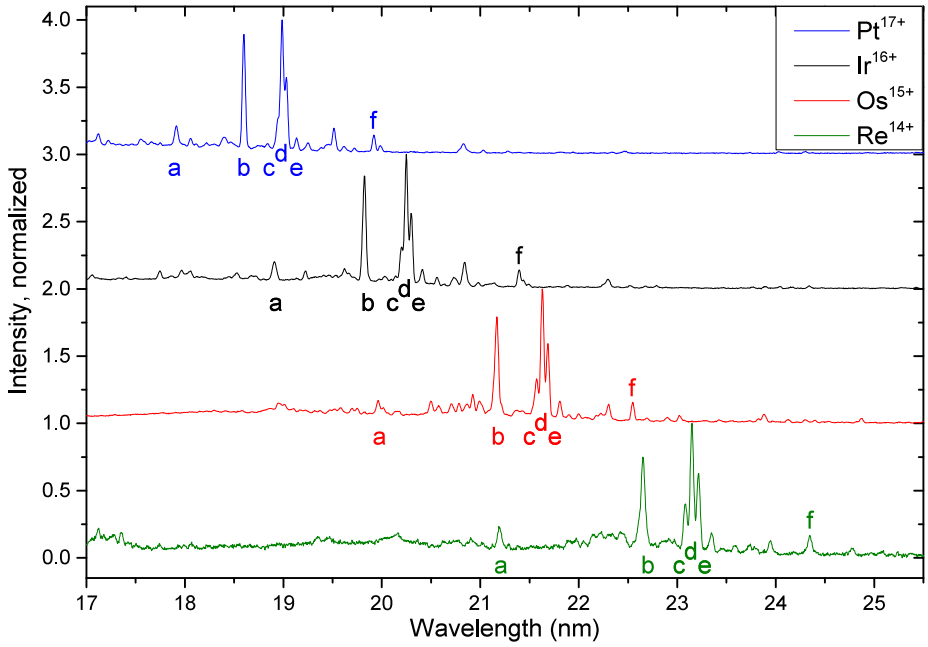

Fig. 4.9 Spectra of Re, Os, Ir, and Pt taken at the electron beam energies where the fluorescence of the Pm-like lines is strongest. Characteristic lines that are visible for all the elements are labeled with the letters a to f. Note that minor contributions from the neighboring charge states also contribute to these spectra, see Fig. 4.7.

and for the quenching of transitions by electron impact. Based on the corrected line strengths a new synthetic spectrum was made, see Fig 4.10b. An example of the Python code for the procedure is given in appendix B. The much-improved similarity to the observed spectra allows for the identification of several lines, as indicated in table 4.4.

4.5.1 Influence of the electron beam density

The rate of electron impact (de-)excitation depends on the electron density. From the operational conditions of the EBIT, a peak electron density of $7 \cdot 10^{12}\,\mathrm{cm}^{-3}$ is expected. But as can be seen in Fig. 4.11, the best agreement with the observed spectra is achieved for an electron density in the order of $10^{11}\,\mathrm{cm}^{-3}$. Since a limited amount of configurations is considered in these CRM calculations, the population distribution of the $4f^{13}5s^{1}5p^{1}$ configuration, and therefore the relative line strengths, might not be accurately reproduced. Inclusion of more configurations with higher excitation energies might correct this. However, as discussed earlier, inclusion of more configurations in the FAC calculations results in a worse accuracy for the transition energies. The current CRM calculations also neglect the possibly incomplete overlap of the ion cloud with the electron beam. The radius of the ion

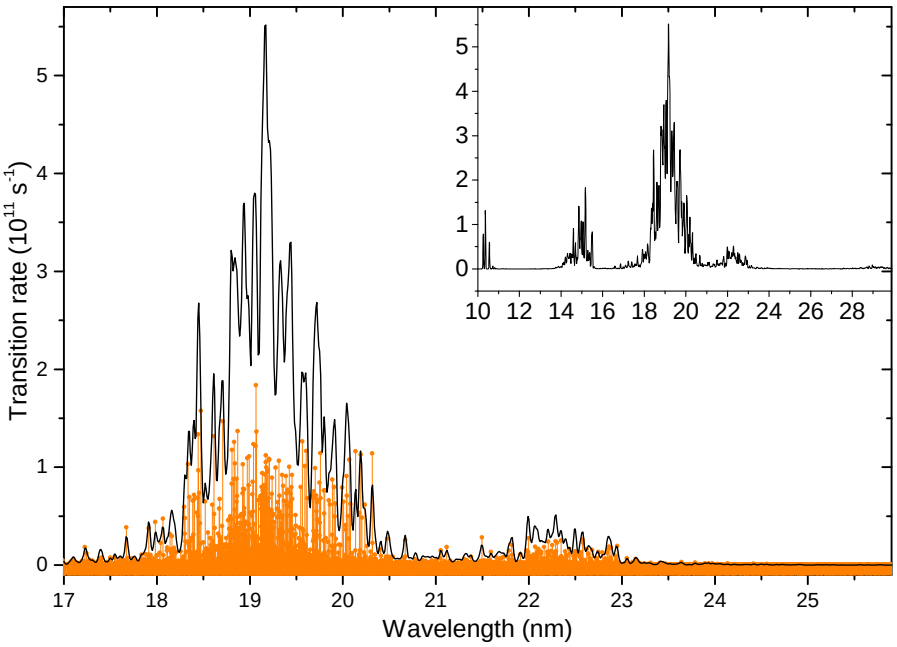

(a) Spectrum based solely on the transition rates as calculated with FAC. Similar predictions were made using other methods [72, 124]. The height of the synthetic spectrum was divided by 2 for visibility.

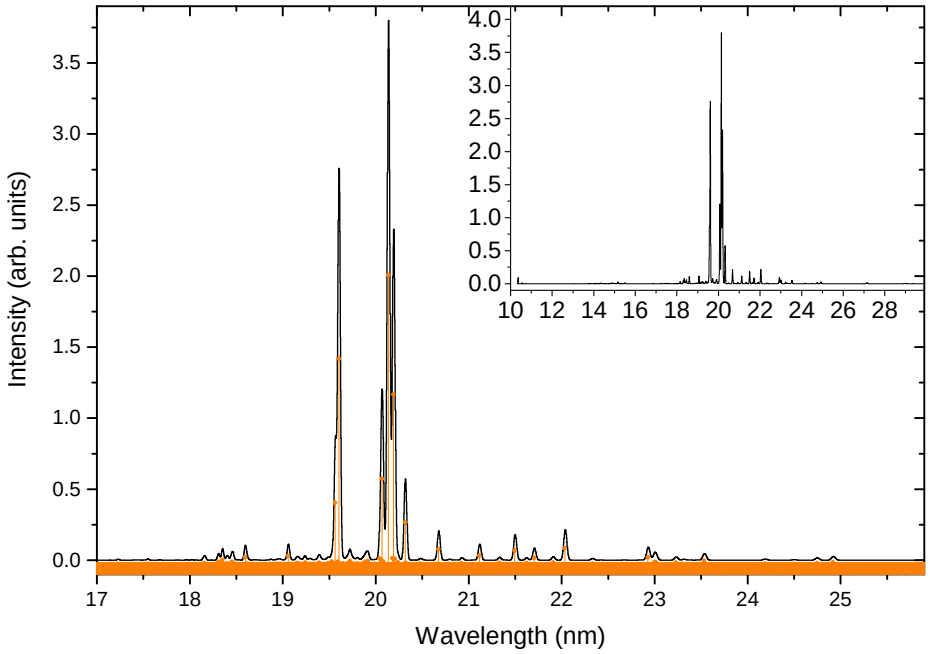

(b) Spectrum based on CRM calculations.

Fig. 4.10 Synthetic spectra of Pm-like Ir^{16+}. The predicted lines (orange) were convolved with Gaussian functions with a width corresponding to the resolving power of the spectrometer. Significant differences between the spectra are due to the absence of the $4f^{12}$-core transitions. The inset shows that in the region outside 17-26 nm no strong lines are to be expected.

Table 4.4 Measured lines in the Pm-like charge state. Wavelengths λ are given in nm. Their uncertainties are given by the square-root of the sum of squares of the fit uncertainty and the calibration uncertainty. The relative intensities (I) have been corrected for the theoretical efficiency of the spectrometer and are estimated to be accurate at a level of 20-30%. Note that the Re spectra were taken at a lower electron beam current, see table 4.2. The upper part of the table shows characteristic lines that appear in the spectra of multiple elements. These lines were given an identifying letter in the column Id that is referenced to in Fig 4.9. The lower part of the table shows unidentified lines that were. The superscript ^{b} blends.

Id	Rhenium (14+)		Osmium (15+)		Iridium (16+)		Platinum (17+)		levels	
	λ	I	λ	I	λ	I	λ	I	upper	lower
a	21.178(2)	8	19.9537(6)	24	18.9056(17)	26	17.9131(14)	20		
b	22.6432(15)^b	36	21.1503(29)^b	102	19.8225(8)^b	153	18.5985(10)^b	133	$4f^{13}5s^15p^1(J=7/2)$	$4f^{13}5s^2(J=7/2)$
c	23.0708(14)	24	21.5637(7)	83	20.1974(9)	52	18.9429(13)	34	$4f^{13}5s^15p^1(J=7/2)$	$4f^{13}5s^2(J=5/2)$
d	23.1401(13)	54	21.6236(6)	283	20.2481(9)	188	18.9865(9)	152	$4f^{13}5s^15p^1(J=9/2)$	$4f^{13}5s^2(J=7/2)$
e	23.2033(13)	32	21.6788(6)	159	20.2986(9)	103	19.0313(9)	83	$4f^{13}5s^15p^1(J=5/2)$	$4f^{13}5s^2(J=7/2)$
f	24.3145(13)	10	22.5409(6)	44	21.3886(8)^b	27	19.9195(10)	21	$4f^{14}5p^1(J=3/2)$	$4f^{14}5s^1(J=1/2)$
	22.6004(16)	33	18.9426(13)	12	17.9526(44)^b	11	17.0194(52)^b	3		
	22.6941(16)	18	18.9994(15)	9	18.0436(42)^b	10	17.0688(46)^b	3		
	22.7712(16)	5	21.1636(7)^b	114	18.5201(27)	7	17.1213(22)	11		
			21.2093(18)^b	11	18.6663(23)	7	17.2227(20)^b	5		
			21.8003(6)	34	18.7203(23)	6	19.1322(11)	13		
			23.0181(10)	15	20.4102(10)	22	19.7225(11)	4		
			23.8785(9)	21	22.2743(17)	13	19.9859(11)	7		
			24.1225(11)	8	22.7683(19)	8	20.8277(13)	11		
			24.3936(11)	7			21.0290(18)	3		
			24.8698(13)	14						
			25.5087(18)	5						

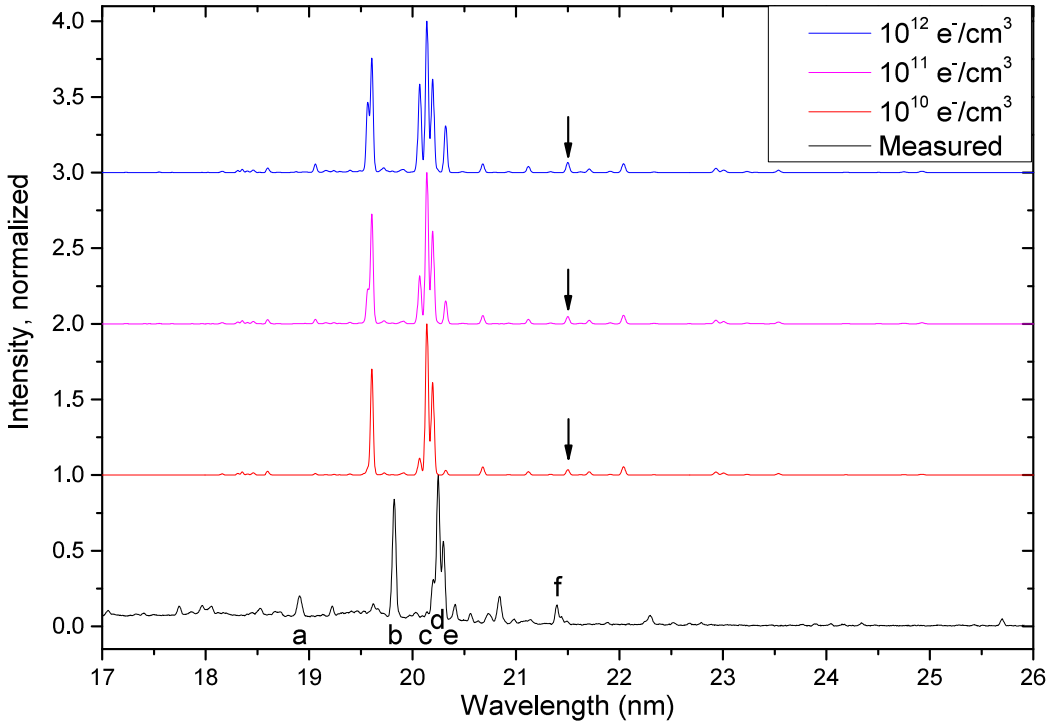

Fig. 4.11 Comparison of the Pm-like Ir^{16+} spectrum to CRM calculations at several electron beam densities. Mainly the intensity ratio between peaks c and d is affected by its value, which is used to fine-tune the input parameters of the CRM calculations. The position of the $5s_{1/2}$ - $5p_{3/2}$ transition in the synthetic spectra is indicated with arrows.

cloud depends strongly on the shape of the trapping potential and the charge state of the ions. It has been shown for example, that a cloud of Fe^{9+} can expand to a radius ten times larger than that of the electron beam, which reduces the effective electron density that the ions experience significantly [100]. In conclusion, the CRM calculation performed in this work are suitable to identify lines; to extract information about the electron beam density, a more complete model is required.

4.5.2 Comparison of the $5s$ - $5p$ wavelengths to predictions

In table 4.5, the measured wavelengths for the $4f^{14}5p$ to $4f^{14}5s$ transitions are compared to calculations made in the course of this work with FAC. Additionally, state-of-the-art calculations made with other advanced codes are included. For completeness, tentative identifications from literature are also included. The differences between theory and measurement are visualized in Fig. 4.12. The behavior of the CIDFS and RMBPTB is fairly similar to each other. Especially at the level crossing from $Z = 76$ to $Z = 77$ do the predictions have large deviations from the measurements. Interestingly, here the sign of the differences changes.

Table 4.5 Comparison of available theory values with the observed transitions (Expt.) identified as $5s_{1/2}$ - $5p_{3/2}$. All values are given in nm. It has to be noted that the FAC results of this work were optimized to the measurements by restricting the number of configurations included in the configuration interaction calculations, refer to section 4.5.

Ion	Expt.	CIDFS [72]	RMBPTB [123]	COWAN [123]	FAC
W^{13+}	25.82(2) [121, 122]	26.40	26.112	26.083	26.13
Re^{14+}	24.3145(13)	24.49	24.288	24.280	24.33
Os^{15+}	22.5409(6)	22.80	22.652	22.521	22.60
Ir^{16+}	21.3886(8)	21.27	21.166	21.282	21.50
Pt^{17+}	19.9195(10)	19.89	19.811	19.839	19.95
Au^{18+}	18.40(3)[119, 122]	18.63	18.570	18.566	18.67
Pb^{21+}	15.30(10) [121, 122]		15.408	15.341	15.48

Concluding, the accuracy of the currently available predictions for the $5s_{1/2}$ - $5p_{3/2}$ transition energy is at the level of of 1%. The large and systematically negative difference between the predictions and the identifications at W ($Z = 74$) and Au ($Z = 79$) makes the literature identifications suspicious, and therfore additional measurements would be required for those ions.

4.6 Identifications of transitions in the Ir^{17+} spectrum

Spectra of Ir^{17+} were obtained during approximately 5.5 hours while the HD-EBIT was kept at a constant current of 40 mA and an acceleration potential of 560 V. The 21 spectra were averaged and calibrated to produce the spectrum presented in Fig. 4.14. Guided by the data from Fig. 4.7, the Ir^{17+} lines were selected for fitting in the same manner as for the spectra of the Pm-like systems. The results of the fits are summarized in table C.1. Lines in the isoelectronic spectra of Nd-like Re, Os, and Pt were also fitted; the results are summarized in appendix C. Likewise, the lines in the Pr-like spectra were fitted, the results are also summarized in appendix C. The rest of this section concerns only the spectra of Nd-like Ir^{17+} .

To support the identification of lines in Ir^{17+} , a synthetic spectrum was generated using CRM. For the calculation of the energy levels, transitions rates, and excitation cross sections the following configurations were included in FAC: $4f^{14}$, $4f^{13}5s^1$, $4f^{13}5p^1$, $4f^{12}5s^2$, $4f^{12}5s^15p^1$, $4f^{11}5s^25p^1$. Inclusion of more configurations in the calculations shifted the

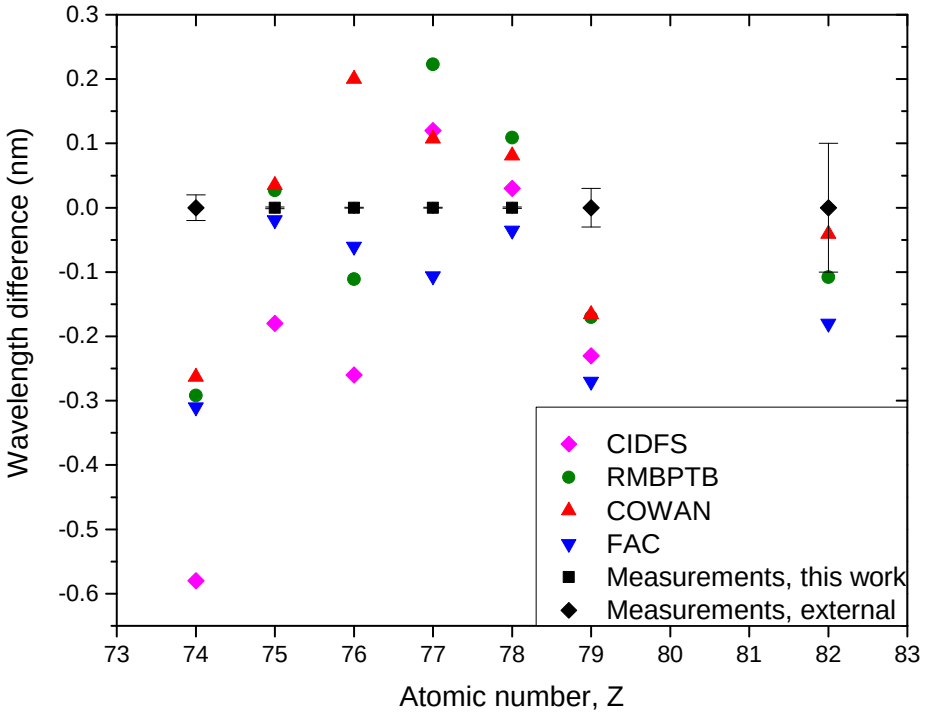

Fig. 4.12 Differences between available experimental and theoretical values for the $5s_{1/2}$ - $5p_{3/2}$ transitions, based on table 4.5. The measurements that were not performed during the course of this work were obtained by Träbert, Hutton, and Vilkas [119, 121, 122], c.f. table 4.5.

transitions energies to higher values, away from the measured values. The results for the energy levels are shown in the Grotrian level diagram Fig. 4.13.

The electron energy distribution for these calculations was centered at 440 eV and set to follow a Gaussian distribution with a width of 5 eV, the distribution was cut-off at 435 eV and 445 eV. The measured spectrum was best reproduced at an electron density of 10^{12} cm^{-3}. As discussed before, the model does not include all the configurations that can be populated by electron impact excitation, and the overlap of the ion cloud with the electron beam is not considered. Therefore, the electron density for the CRM calculations does not correspond to the peak electron density in the EBIT.

The synthetic spectrum shows that the brightest spectral features are most likely due to transitions to the $4f^{12}5s^2$ and $4f^{13}5s$ configurations. Transitions to the $4f^{14}$ configuration in the investigated spectral range are predicted to be too weak to be observed with the present setup. Compared to the Pm-like spectra, the Ir^{17+} spectrum features more bright transitions which are energetically closely spaced. Therefore, identifying transitions was difficult. Where a close resemblance between the measured and predicted spectra was observed, tentative

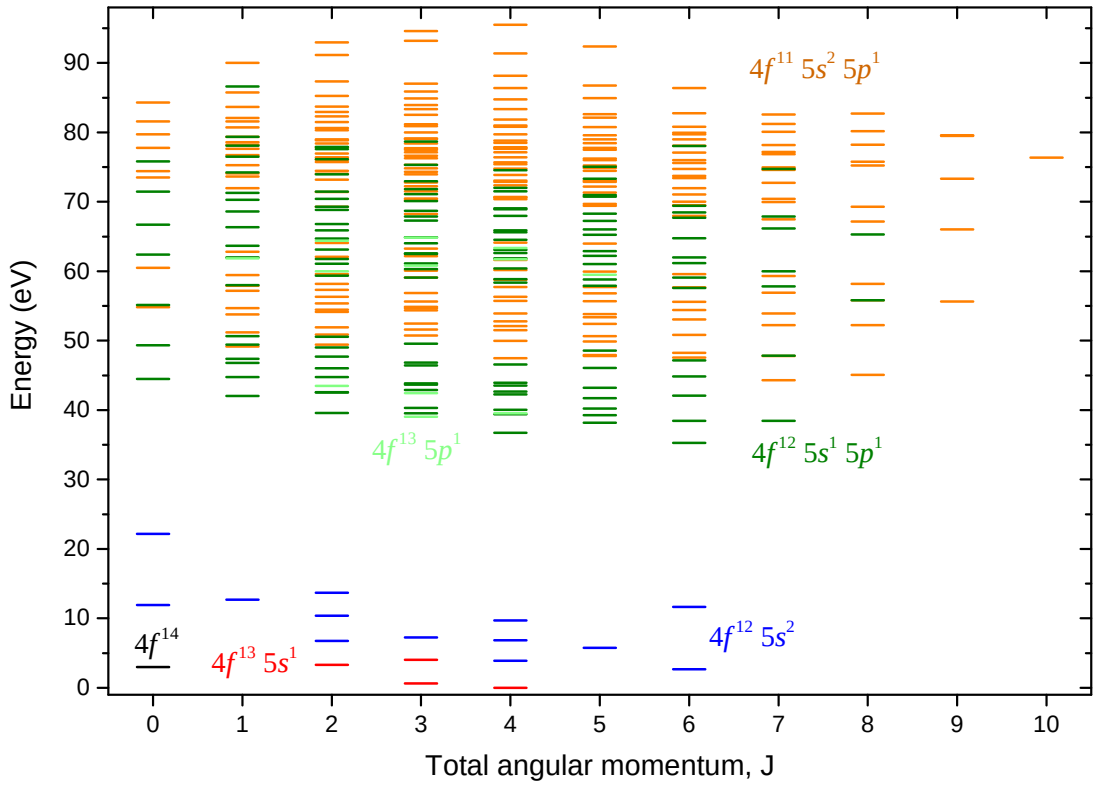

Fig. 4.13 Grotrian level diagram of the energy levels of Ir^{17+} as obtained with FAC.

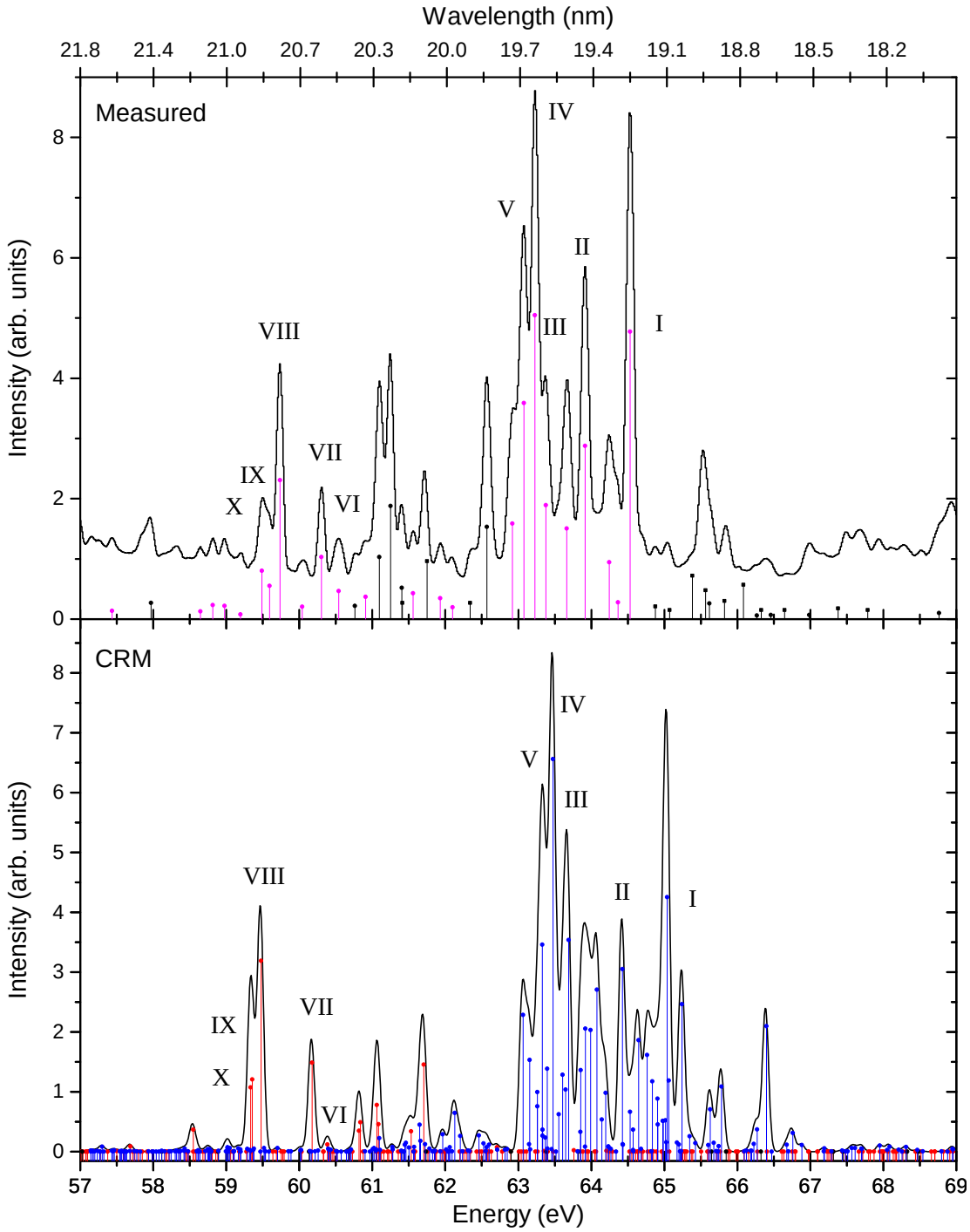

Fig. 4.14 Detailed view of the brightest spectral features of Ir^{17+} observed in the EUV range. Spectral lines that were determined to belong to Ir^{17+} were fitted and are indicated in magenta. Lines belonging to Ir^{16+} (circles) and Ir^{18+} (squares) are indicated in black. In the CRM spectrum the color of the circle indicates the lower level of the transition. Transitions to the $4f^{12}5s^2$ configuration are indicated in blue, to $4f^{13}5s^1$ in red, and to $4f^{14}$ in black. The identified lines are labeled with Roman numerals in both spectra; the numeral correspond to those in table 4.6

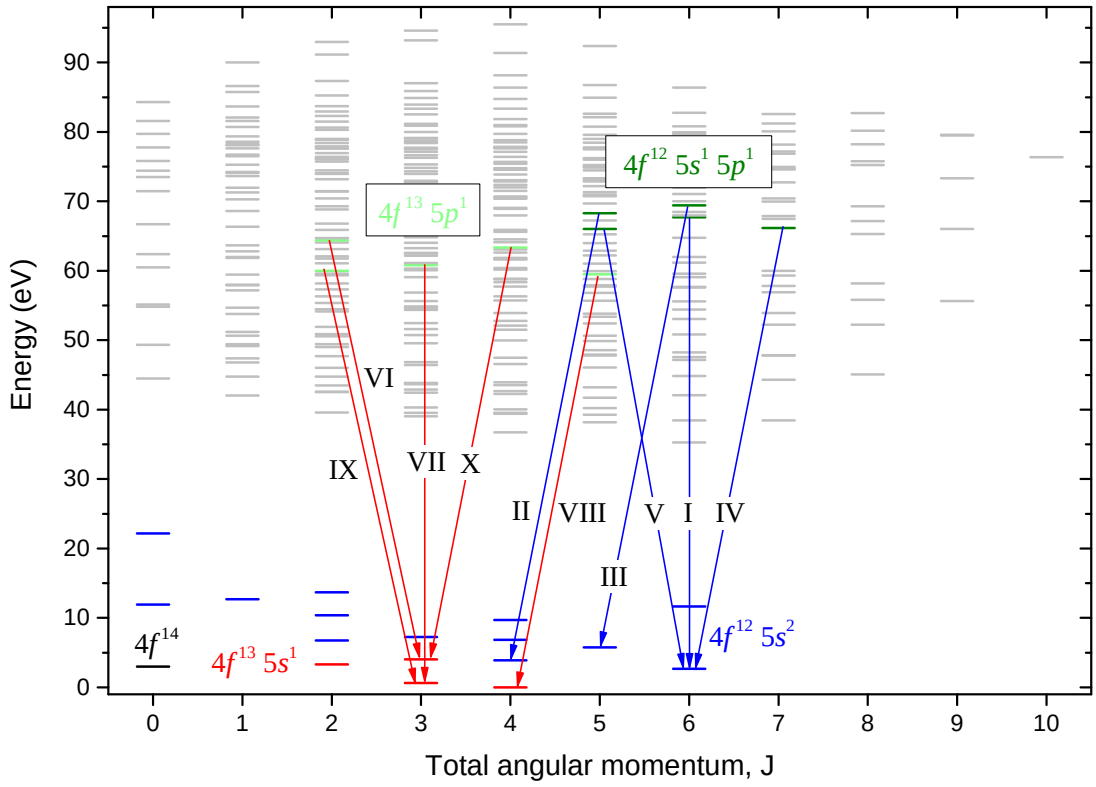

Fig. 4.15 Grotrian level diagram of the energy levels of Ir^{17+} as obtained with FAC. The identified transitions are indicated with arrows, the roman numerals correspond to the Id values in table 4.6. Fine-structure levels of the $4f^{13}5p^1$, $4f^{12}5s^15p^1$, and $4f^{11}5s^25p^1$ configurations that do not participate in identified transitions are colored in gray

identifications were made; refer to table 4.6. Due to admixture of spectral features from Ir^{16+} and Ir^{18+}, the predicted bright lines around 60 eV and 66 eV could not be resolved.

One of the goals of this work is to find the energy splitting between the $4f^{12}5s^2$ and $4f^{13}5s^1$ configurations. As with the Pm-like systems, transitions between configurations with different $4f$-cores are highly suppressed. This is confirmed by the two types of transitions that were identified. Those are namely E1 transitions between the $4f^{12}5s^2$ (parity even) and $4f^{12}5s^15p^1$ (parity odd) configurations, and transitions between the $4f^{13}5s^1$ (parity odd) and $4f^{13}5p^1$ (parity even) configurations. Hence, Rydberg-Ritz combinations with a single upper level to levels of both the $4f^{12}5s^2$ and $4f^{13}5s^1$ configurations were not found.This is demonstrated in the Grotrian level scheme of Fig. 4.15, where all the identified transitions are marked.

If transitions between the upper two $4f^{12}5s^15p^1$ and $4f^{13}5p^1$ configurations were to be observed, they could be used to deduce the splitting between the lower two configurations. Many of the predicted $4f^{12}5s^15p^1$ to $4f^{13}5p^1$ transitions are calculated to have energies in

Table 4.6 Line catalog of the fitted transitions in the Nd-like charge state. The wavelengths were converted to eV using hc =1239.841 973 9(76) nm eV as recommended by CODATA [13]. Where identifications were made the involved levels are indicated and a short identification in Roman numerals is indicated. The L and S quantum numbers of the fine-structure levels in the $4f^{12}$ and $4f^{13}$ configurations could not be determined, therefore, only the valence orbitals and total angular of those levels are given. For the $4f^{13}5s^2$ and $4f^{12}5s^2$ fine-structure levels the term symbols as listed in section 1.3 were used.

λ (nm)	Energy (eV)	Intensity (arb. units)	Transition Upper	Lower	Id
19.2222(12)[b]	64.5005(40)	72	$4f^{12}5s^15p^1(J=6)$	$^3H_6$	I
19.27174(18)	64.3347(59)	4			
19.3077(11)	64.2149(37)	14			
19.4073(10)	63.8853(33)	43	$4f^{12}5s^15p^1(J=5)$	$^3F_4$	II
19.4833(10)	63.6361(33)	23			
19.5715(10)[b]	63.3494(32)	28	$4f^{12}5s^15p^1(J=6)$	$^3H_5$	III
19.6169(8)[b]	63.2027(26)	76	$4f^{12}5s^15p^1(J=7)$	$^3H_6$	IV
19.6644(9)[b]	63.0501(29)	54	$4f^{12}5s^15p^1(J=5)$	$^3H_6$	V
19.7126(12)[b]	62.8959(38)	24			
19.97271(11)[b]	62.0768(33)	3			
20.02634(9)[b]	61.9106(27)	5			
20.14692(9)[b]	61.5400(29)	6			
20.36168(17)[b]	60.8909(50)	6			
20.48496(8)[b]	60.5245(23)	7	$4f^{13}5p^1(J=2)$	$^1F_3^o$	VI
20.56433(7)[b]	60.2909(19)	15	$4f^{13}5p^1(J=3)$	$^3F_3^o$	VII
20.65508(13)	60.0260(36)	3			
20.7598(10)[b]	59.7232(29)	35	$4f^{13}5p^1(J=5)$	$^3F_4^o$	VIII
20.80929(30)[b]	59.5812(85)	8	$4f^{13}5p^1(J=2)$	$^3F_3^o$	IX
20.84504(23)	59.4790(64)	12	$4f^{13}5p^1(J=4)$	$^1F_3^o$	X
20.94853(17)	59.1852(49)	1			
21.02527(10)	58.9691(29)	3			
21.08258(10)	58.8088(27)	4			
21.14316(15)[b]	58.6403(42)	2			
21.5879(8)	57.4323(21)	2			
21.7671(8)	56.9594(21)	6			
21.8674(9)	56.6982(23)	5			

the order of 10 eV, which is outside the range of both spectrometers employed in this work. Some of the predicted transitions are in the optical range, but there the transition rates are extremely low at 10^{-1} s^{-1} or less.

In Fig. 4.16a the measured energies of the identified lines are compared to the predictions made with FAC. The predicted transition energies to the $4f^{12}5s^2$ configuration are systematically too high by approximately $0.4(1)$ eV. Conversely, the transition energies for the transitions to the $4f^{13}5s$ configuration are systematically too low by approximately $0.17(6)$ eV. In the work of Windberger, the optical transitions of Ir^{17+} were compared to several predictions, including predictions made with FAC calculations [34]. Those calculations were based on a larger basis of 16 configurations compared to the 6 configurations used for identification of the EUV lines. As is demonstrated in Fig. 4.16b, disagreement between the measurements and the FAC calculations with a large basis are at the level of 15-20 eV. This suggests that the FAC calculations performed in this work are better at predicting the energy difference between the $4f^{12}5s^2$ and $4f^{13}5s^1$ configurations, which is investigated in chapter 6.

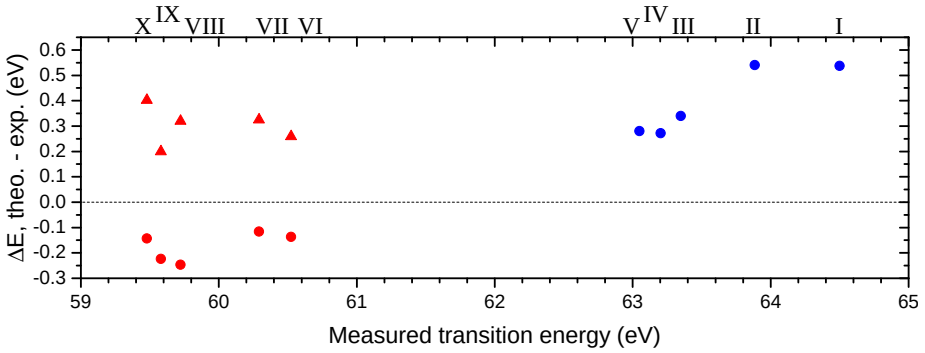

(a) Comparisons of the measurements to the FAC predictions optimized for the EUV spectra (circles) and FSCC (triangles).

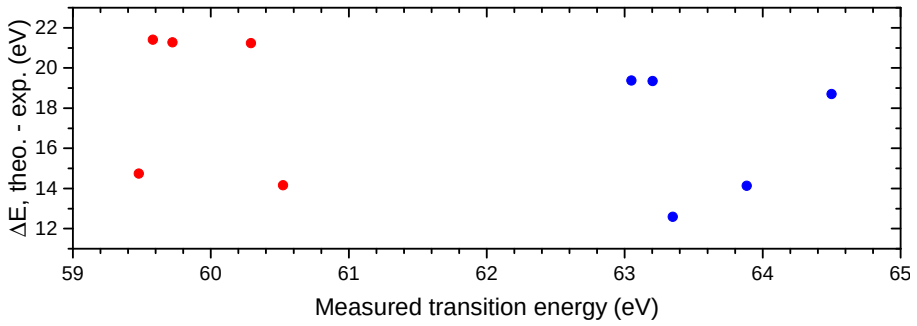

(b) Comparisons of the measurements to FAC predictions with an increased configuration basis, as was used in previous work [34].

Fig. 4.16 Differences ΔE between the predicted transition energies and the measured transition energies for the identified lines. The color coding corresponds to that of Fig. 4.14, that is, blue for transitions to the $4f^{12}5s^2$ configuration, and red for transitions to the $4f^{13}5s$ configuration. The uncertainties are smaller than the symbols.

Chapter 5

Spectroscopy in the optical regime

> Non; mais Dieu a donné à l'homme l'intelligence pour venir en aide à la pauvreté de ses sens: je me suis procuré de la lumière.
>
> Le Compte de Monte-Cristo, Alexandre Dumas

When asked how he could read and write in the darkness of his dungeon, Abbé Faria gave the answer cited above. The statement more or less translates to 'Man has the intelligence to aid his mediocre senses, therefore, I made a light source.'. This can be applied to much of the work of experimental physicists. Examples include the improvements made to telescopes by Galileo Galilei, to more recent high-tech advances such as optical frequency combs and the LIGO interferometers [33, 135]. Physicists have always relied on ingenuity to improve their observational capabilities. In this chapter the setup and data analysis methods, which were employed to investigate extremely weak optical transitions of ions in an EBIT, are described.

5.1 The optical spectrometer setup

To measure the wavelengths of the fluorescence light emitted from the ion cloud in the EBIT, a grating spectrometer was employed. A telescope system and the so-called periscope box were used to focus the image of the ion cloud on the entrance slit of the spectrometer. Light from a hallow cathode lamp could be imaged on the entrance slit of the spectrometer for calibration purposes. The setup had previously been employed to investigate optical transitions in several other highly charged ions (HCI) [136, 137, 130, 138]). Next follows a description of the individual components of the setup. An overview of the full setup, from light source to camera for recording of the spectra, is shown in Fig. 5.1. Since the camera had recently been replaced with a newer model, details concerning the performance of the

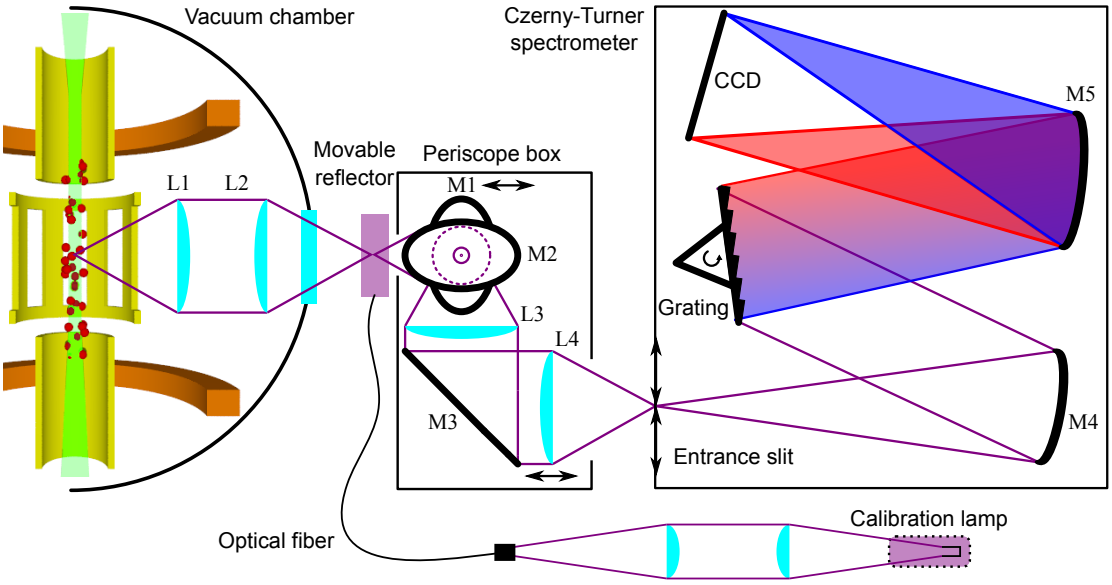

Fig. 5.1 Schematic overview of the setup used for spectroscopy in the optical range, adapted from [130]. The path of the fluorescence light from the ion cloud is shown in purple, and after the grating separated into its two components: red and blue. The movable reflector can be used to couple calibration light into the optical system. Details concerning the setup are given in the main text.

new camera are discussed in deeper detail. On the basis of camera performance, an analysis of the noise, and the stability of the calibration the optimal read-out scheme was established.

The telescope system consisting of the lenses L1 and L2 serves to increase the amount of collected light. Both lenses have a diameter of 25.4 mm and a focal length of 150 mm, so that light over a solid angle of $\Omega \approx 0.17$ sr is collected. The image of the horizontally elongated ion cloud needs to be rotated by 90° so that it can be aligned with the vertical entrance slit of the optical spectrometer. For this purpose the periscope box houses the two mirrors M1 and M2. Due to space constraints a third mirror M3 is required to reflect the light away from the EBIT, towards the spectrometer. With the lenses L3 and L4 in the periscope box, the image is refocused at the entrance slit of the spectrometer.

The lenses in the setup are made of fused silica, so that the transmission efficiency of those does not vary by more than 5% over the here investigated range of 200 nm to 700 nm. To focus the image of the ion cloud onto the entrance slit, it was necessary to adjust the focusing and alignment of the periscope box when a new wavelength region was investigated. The focusing is optimized by translating lens L4 along the optical axis. The alignment of the focus with the entrance slit of the spectrometer is optimized by translating mirror M1 as indicated in Fig 5.1.

The spectrometer, of the type TRIAX 550 of the Horiba company, was build after a design by Czerny and Turner [139]. It has a focal length of 550 cm and a focal ratio of $f/6.4$. Light that passes the entrance slit is collimated by a toroidal mirror (M4 in Fig. 5.1) and reflected onto the flat diffraction grating. Part of the dispersed light is then refocused by another concave mirror M5 such that an image is produced at the position of the camera. The spectral range that is imaged onto the camera is determined by the angle of the grating, both mirrors M4 and M5 are fixed in place during operation. The resolving power of the spectrometer is partly determined by the width of the entrance slit, that can be set from 2.00 mm down to 0 µm. Another determining factor for the resolving power is the line density of the grating, which for the measurements performed in this work was 2400 grooves/mm.

Calibrating the setup can not be done with light from the ions in the EBIT as was done for the measurements in chapter 4 for two reasons. First, there is no HCI with enough optical transitions of which the transition wavelengths are known to high precision. Second, to reach the required precision of 1 ppm, calibrations need to be made more frequently than can be achieved by switching the injection source. For these reasons the calibration light source is a FeAr hollow cathode lamp outside the vacuum of the EBIT. The neutral and first charge states of these elements have sufficient optical transitions to calibrate the spectrometer over the whole optical range. With an optical fiber the calibration light is guided to illuminate a diffuse aluminum plate which is mounted between the vacuum chamber and the periscope box. The diffuse plate can be moved with an electromagnet into the path of the light from the ion cloud. In this manner, the calibration light is reflected into the periscope box and follows the same path as the light from the ion cloud.

A new camera of the type Princeton PIXIS 2KBUV was installed to replace the original camera that broke down. Its properties are summarized in table 5.1. A noteworthy difference is that the new camera is cooled by a Peltier element instead of liquid nitrogen, so that the typical operating temperature is $-70\,^{\circ}\mathrm{C}$ instead of $-195\,^{\circ}\mathrm{C}$. Consequently, the thermal noise is approximately 50% higher compared to the previous camera [137, 136]. The detector is coated to enhance the efficiency in the ultra-violet range, refer to Fig. 5.2.

In addition to the thermal noise, the read-out process also adds noise. The read-out noise is given per bin, because the read-out electronics can be configured to add multiple pixels together in a single bin before performing the read-out step. Binning in the horizontal direction leads to loss of spectral resolution but binning in the vertical direction does not have this disadvantage, as is demonstrated in Fig. 5.3(top). In a spectrum, where multiple rows of bins are projected in the vertical direction, the read-out noise is expected to decrease

Table 5.1 Properties and settings of the PIXIS 2KBUV camera [140].

Property	Value
Dimensions	2048×512 pixels
Pixel size	$13.5 \times 13.5\,\mu m^2$
Operating temperature	$-70\,^{\circ}C$
Read-out noise, N_{RO}^{bin}	3.74 e^- / bin
Thermal noise	1.59 e^- / pixel hour
Read-out frequency	100 kHz
Pre-amplifier setting	Low-noise output
Conversion gain	1.01 e^- / count

as

$$N_{RO} = N_{RO}^{bin}\sqrt{\frac{512}{n}}, \tag{5.1}$$

where n is the number of pixels that are added in one bin. The predicted behavior can be observed in Fig. 5.3(bottom). Clearly increased binning reduces the read-out noise in the spectrum, but some of the vertical information is needed for the removal of cosmics and for the correction of optical aberrations. Experience shows that a binning of 64 pixels per bin, i.e. dividing the CCD into 8 rows, gives sufficient vertical information to remove the cosmics that accumulate over half an hour with high fidelity.

5.2 Measurement procedure

Several hours, or even days, of integration time were required to achieve a good enough signal to noise ratio for the investigated lines. This is because the transitions rates of the investigated lines are in the range of only $1-100\,s^{-1}$. To ensure a high quality of the data, a procedure was developed which prevents some of the pitfalls that would otherwise occur. The details and reasoning behind the procedure will be described next, but first the steps are summarized as:

1. Optimize spectrometer for the wavelength of interest
2. Acquire background spectrum
3. Acquire calibration spectrum

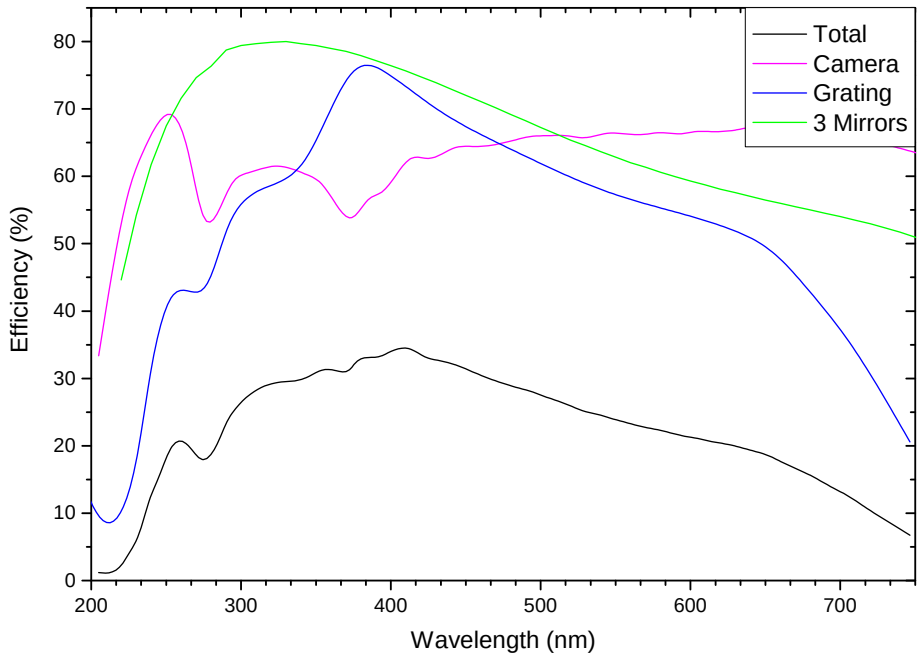

Fig. 5.2 Efficiency curves for the setup [140, 141]. The curve for the total efficiency is constructed from efficiencies of the individual components.

4. Acquire ion spectrum
5. Repeat step 3 and 4 for another 5 times
6. Acquire calibration spectrum
7. Rotate the grating slightly and restart the sequence from step 2

As described in the previous section, the focusing and alignment of the optical setup needs to be optimized for each wavelength range. Sometimes it was necessary to tune the EBIT to another charge state for a bright enough line with the correct wavelength for optimization. To optimize the focusing at the entrance slit of the spectrometer, spectra were recorded for several positions of lens L4 with the entrance slit fully opened to 2.00 mm. In this was, the real image of the ion cloud was not clipped at the edges of the slit. The lens position was set where the test line had the minimum line width and the highest intensity, corresponding to a good focus in order to optimize the signal intensity. The alignment of the image on the center of the slit was optimized by varying the position of mirror M1 in steps of 10 µm or more. The mirror position where the width of the entrance slit had no measurable effect anymore on the position of the peak center on the CCD was set for the rest of the measurements. This ensured that the intensity maximum of the image coincided with the center of the entrance slit.

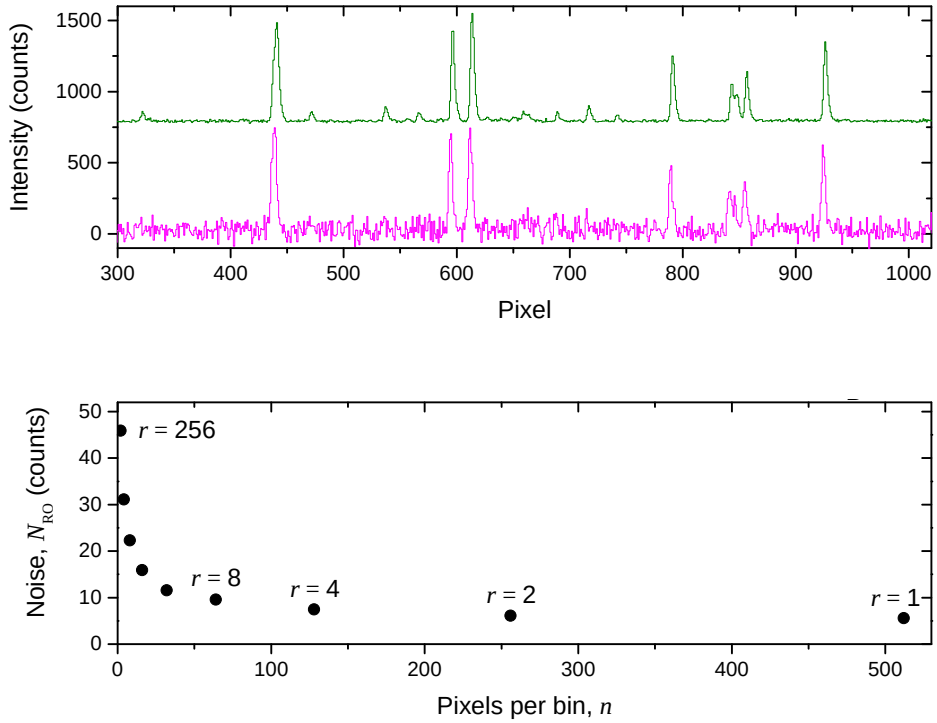

Fig. 5.3 Calibration spectra were taken with several vertical bin sizes to study the effect on the noise. The spectra were obtained for 30 s each; pixel 1000 corresponds approximately to 360 nm. *Top:* The magenta spectrum was taken without any binning, i.e. 1 pixel per bin, the green spectrum was taken with a binning of 256 pixels per bin. An offset was added to the upper spectrum for clarity. The CCD images were not corrected for optical aberrations, causing the spectral lines to be slightly asymmetric and. *Bottom:* The noise, determined by the standard deviation of the signal over an area without lines, plotted as a function of the binning. The number of rows r covering the full CCD is displayed next to selected data points; $r = 8$ was selected for the measurements in this work.

The next steps were fully automatized, and to reduce stray light and temperature fluctuations, entry to the laboratory was restricted. First, a measurement of the background light was made for 30 min by inverting the trap potential. In this way no ions remain in the trap, while the light due to background light sources such as the hot cathode was unchanged. This also ensured that possible contaminants of the ion cloud were ejected regularly. Also, by starting with a background measurement, the mechanics of the spectrometer have time to settle. As has been shown in [130, 138] for example, the grating continues to rotate slightly during the first 20 min after having been rotated. For the background measurement this was not an issue since it will be smoothed later anyway.

Next, light from the ion cloud was recorded for six times 30 min, a calibration spectrum was taken before and after each ion cloud acquisition. In previous work, drifts of spectral

lines at the level of $6 \cdot 10^{-4}$ nm over 30 min were observed when the spectrometer was not recalibrated [130]. This is the same effect that was already observed for the EUV spectrometer in Fig. 4.5. The temperature in the laboratory was not actively stabilized; periodic temperature fluctuations in the order of 1 °C over a 24 hours could cause components of the spectrometer to shift by an estimated 10 µm. Since calibrations were taken before and after each ion cloud measurement, and because over 30 min the drift was approximately linear, two calibrations could be interpolated to make systematic shifts negligible. Additionally, for much longer acquisition times the number of pixels that need to be discarded due to cosmics would grow too large. On the other hand, shorter acquisition times would increase the number of CCD read outs, and thus increase the read-out noise. The calibration spectra were taken for 1 to 5 min, depending on the brightness of the reference lines.

Finally, the grating was intentionally rotated to shift the spectral range by shifted 0.1 nm. Then, the measurement sequence was restarted by taking the next background spectrum. By moving the grating, the risk of corrupting the whole measurement due to a CCD imperfection coinciding with a line of interest, was reduced. This was more of a precaution, because no strong sensitivity fluctuations over the CCD area were observed.

5.3 Analysis procedure

In general, the analysis procedure for the optical spectra is analogous to the procedure applied to obtain the EUV spectra. However, the long measurement times and high demands to the precision of the measurements required more advanced techniques for certain steps. In the next section an algorithm to remove cosmics from the data is introduced. Followed by a description of the steps required to compose the final spectrum from hours of data.

5.3.1 Removal of cosmics

The employed cosmic removal procedure is based on the algorithm described by Pych [142]. This algorithm was developed for images taken with telescope systems, such as for example Keck II [143]. Where, as for the current application, cosmics need to be removed with high fidelity, while spectral features differing in intensity by several orders of magnitude need to be retained.

The images recorded with the CCD were stored in two dimensional data matrices with 2048 pixels in the dispersive, x-direction, and 8 rows in the non-dispersive y-direction. To remove cosmics from a single image, first the data matrix was divided in sub-areas as indicated in Fig. 5.4. Subsequently the intensity histogram of each area was determined, an

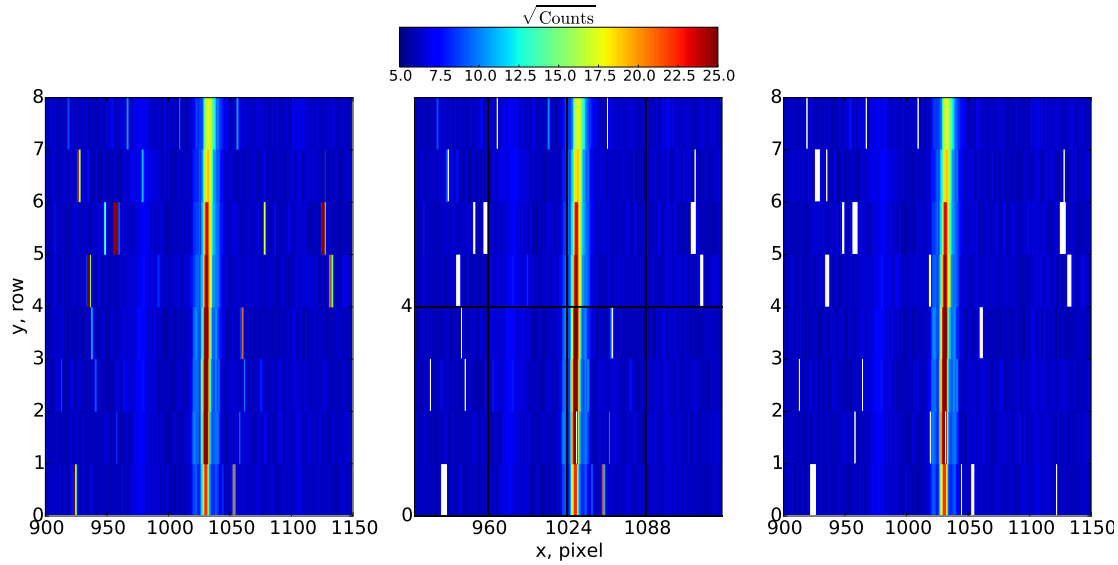

Fig. 5.4 Section of a recorded image to demonstrate the cosmic removal procedure. *Left:* The original image, with a bright spectral line with resolved Zeeman structure belonging to Ir^{17+} at approximately 391.8 nm. A weak line belonging to Ir^{18+} can be seen near column 970. The cosmics can be recognized by their high count value and small area. *Center:* an intermediate step in the cosmic removal process. The grid (64 × 4 bins) that is used in this initial iteration is indicated with black lines, already removed cosmics are colored white. *Right:* the final, cleaned image. By using several grid sizes and multiple iterations, the remaining cosmics were removed.

example is shown in Fig. 5.5. Pixels affected by cosmic muons (cosmics) can be recognized in the histogram by their high value and low frequency. To determine where the cut-off value for cosmics is, the standard deviation σ_h of the distribution is calculated and multiplied by a user defined correction value f_c. If in the histogram there is a region with zero frequency for more than $\Delta = \sigma_h \cdot f_c$ counts, everything past it is marked as a cosmic. Bright peaks in an area cause a higher σ_h, hence the cut-off criterion is adapted to the contents of each area. After the whole image was treated like this, the grid was moved by a few pixels and the procedure was repeated.

By comparing the value of each bin against the distribution of only its neighboring bins, the risk of marking spectral lines as cosmics is greatly reduced. By choosing appropriate correction factors for the threshold, and performing multiple iterations with varying grid sizes, the cosmics could be removed with high fidelity. As Fig. 5.4 shows, the cosmics were removed while the strong line marked as a cosmic. Typically approximately 300 bins were discarded per ion cloud acquisitions of 30 min.

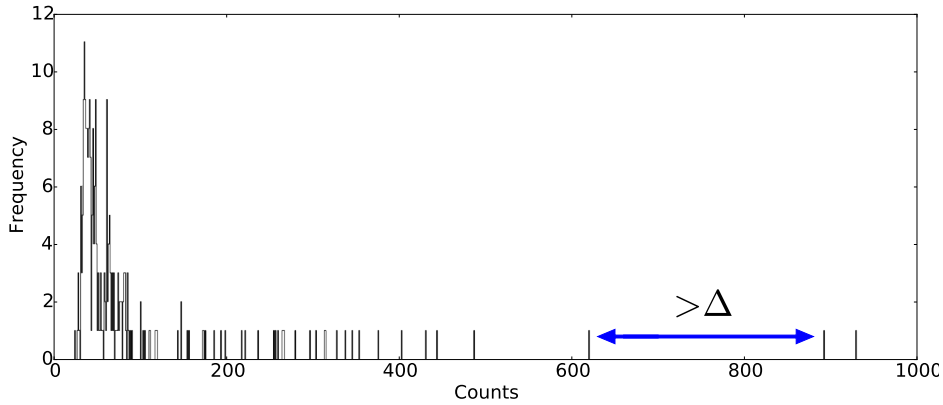

Fig. 5.5 Frequency histogram for the values (Counts) of the bins in the area in corresponding to the lower half from column 1024 to 1088 of Fig. 5.4. The peak centered around 50 counts is due to the nearly flat background, the secondary peak at 70 counts is due to the bright spectral line in this area. In this first iteration, bins with more than 620 counts are marked as cosmics and discarded for the rest of the analysis.

5.3.2 Image correction and row selection

The recorded images were distorted due to optical aberrations, see Fig. 5.6. Coma of the image due to off-axis reflections from the mirrors is reduced in a Czerny-Turner spectrometer as a result of its symmetrical geometry. However, due to imperfections in the alignment, residual coma and astigmatism remain. A rotation of the camera with respect to the grating together with the optical aberrations caused the spectral lines to be slanted and curved. This can be corrected by shifting each row by an amount that is parametrized by the parabola

$$\text{shift} = p_0 + p_1 \cdot y + p_2 \cdot y^2. \tag{5.2}$$

Where the coefficient p_0 is the peak position in the lowest row to which the other rows will be aligned, p_1 is the linear term correcting the slanting, and p_2 the quadratic term correcting for the curvature. The coefficients were determined by fitting the parabola to peak centers, as shown in Fig. 5.6. Due to the varying dispersion of the grating, the parabola coefficients needed to be determined for each wavelength range. Often, a single ion cloud measurement did not yield a bright enough line to determine the coefficients with the required precision. In this case a line from a calibration spectrum was used.

The aforementioned optical aberrations cause the focus of the image at the CCD to be curved. Thus, only a part of the image recorded with the CCD is properly focused. For the best resolving power, only those CCD rows where the focusing was satisfactory were considered in the analysis. The width and intensity of the central peak in Fig. 5.7 was determined for each row. Clearly, the focusing was optimal around row 2 and coincides with

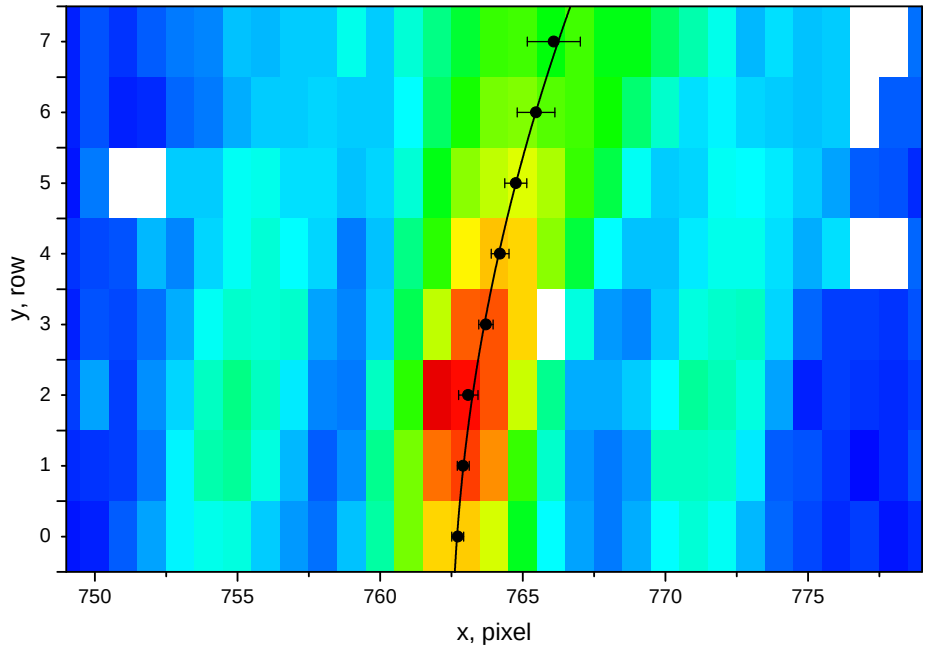

Fig. 5.6 Detailed view of the Zeeman-split Ir^{17+} line at 391.8 nm. The central peak position at each row was determined by the fitting of Gaussian functions. The results are indicated by the black dots. The uncertainties were multiplied by a factor of 10 for visibility. The black line indicates the parabola $x = 762.62(6) + 0.13(5) \cdot y + 0.047(8) \cdot y^2$ that was determined with a fit to the data points.

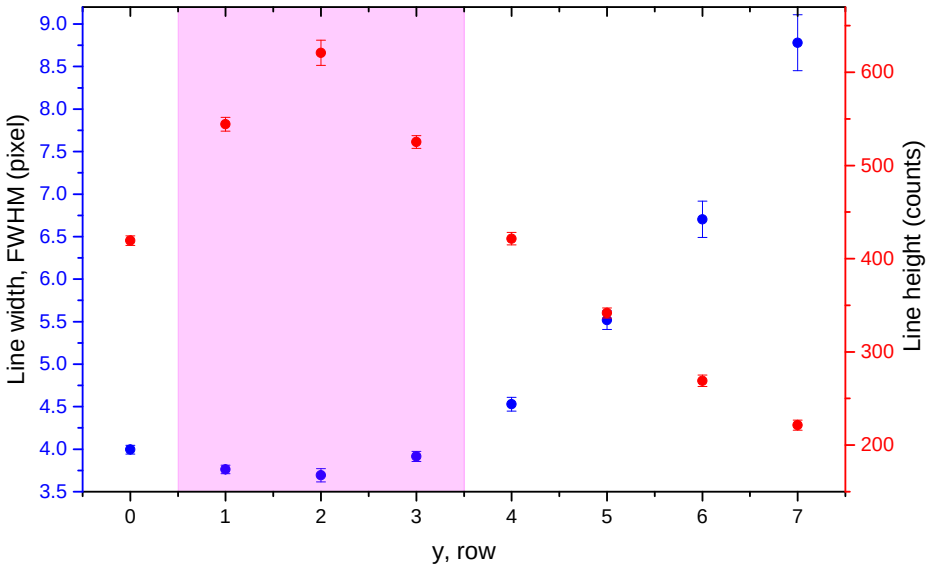

Fig. 5.7 Of each row of the CCD image the peak widths and heights were determined and plotted. The central peak contains multiple Zeeman components, thus the widths found here are larger than expected for a single transition. The area that was used to produce the final spectra is indicated in pink.

the maximum peak intensity, as it should ideally be. Thus, for the best resolving power and highest intensities only rows 1, 2, and 3 were considered in the data analysis.

5.3.3 Composing the final spectrum

After the cosmics were removed from the background data, they were smoothed with a moving average filter. The filter window had a width of 40 pixels, small enough to retain the features of the background but wide enough to smooth out the noise. Each smoothed background was then subtracted from the six corresponding spectra of the ion cloud in the EBIT. The cosmic removal procedure was applied to the resulting background-free ion cloud data. Subsequently each one was straightened and the rows 1, 2, and 3 were projected onto the dispersive axis to produce a spectrum. Except for the background subtraction, the calibration spectra were treated in exactly the same way. Identified calibration lines were used to construct a calibration function as shown in Fig. 5.8. The average of the calibration functions from directly before and after an acquisition of an ion cloud image was used to calibrate each spectrum.

Some lines were so bright that a single acquisition of 30 min was sufficient to fit a Gaussian function to the line. This could be used to check the reproducibility and stability of the measurements and the analysis method, shown exemplary in Fig. 5.9. However, to

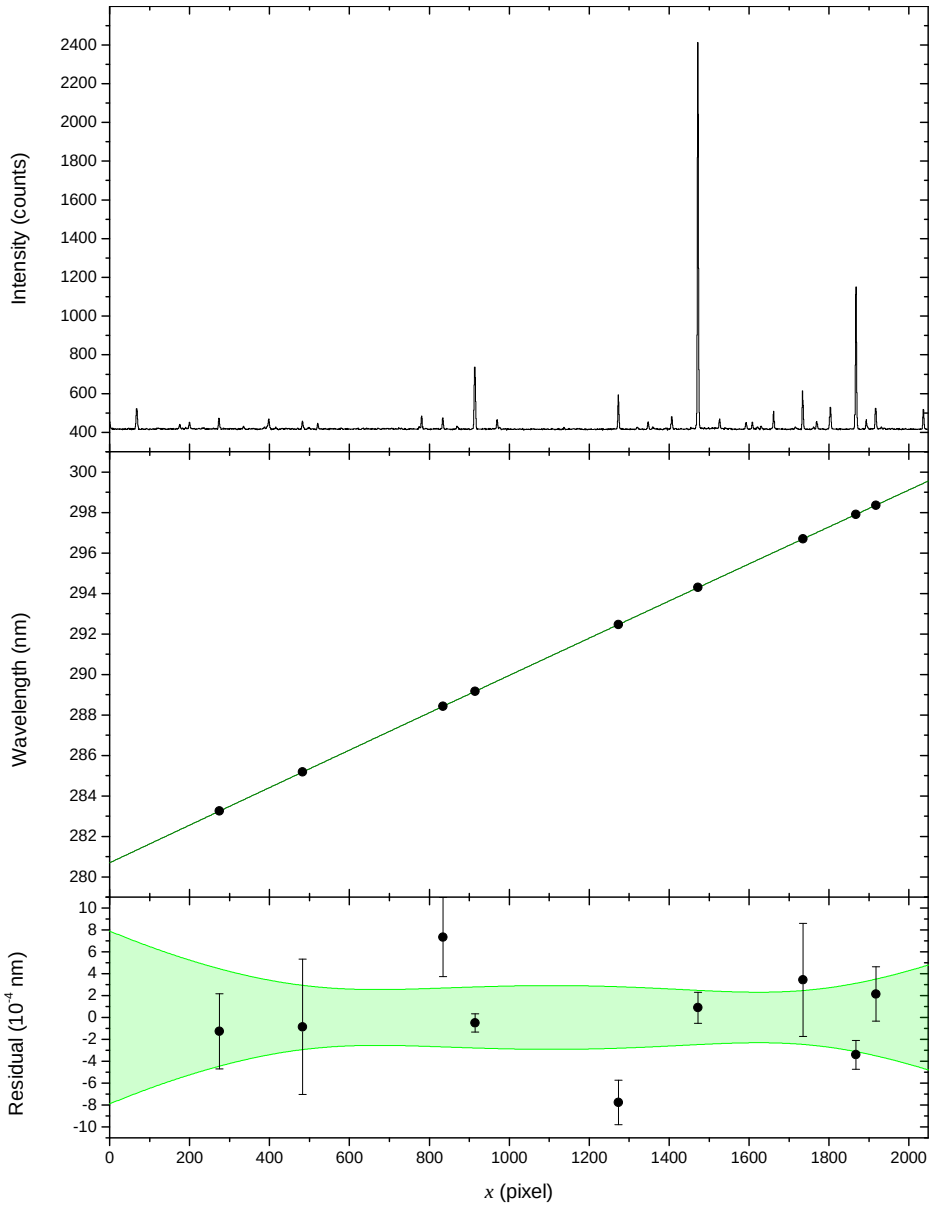

Fig. 5.8 *Top:* Spectrum obtained by a 5 min exposure of light from the Fe-Ar calibration lamp. The peak centers of well-resolved lines were determined with Gauss fits. *Middle:* The values found were plotted against the wavelengths of reference lines [39]. The fit (green line) of a parabolic function to the data yielded the calibration function $\lambda(x) = 280.6951(7) + 9.310(2) \cdot 10^{-3} \cdot x - 4.85(7) \cdot 10^{-8} \cdot x^2$. *Bottom:* Residuals between the data points and the calibration function (circles). In green the 1-σ confidence band of the fit is shown. This is taken as the calibration uncertainty. As in this example, typical uncertainties of $5 \cdot 10^{-4}$ nm or less were found for the central spectral region.

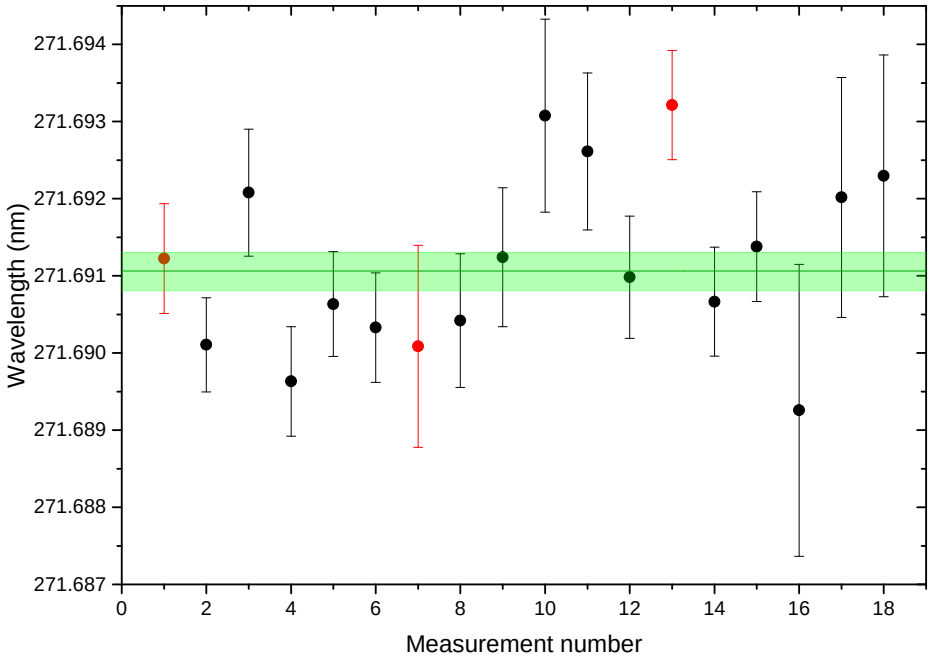

Fig. 5.9 Results for 18 sequentially measured spectra, each individual spectrum was acquired over 30 min. In each spectrum, a Gaussian function was fitted to the Ir^{17+} line at approximately 271.7 nm to determine the wavelength. The results are plotted here in chronological order, the red points indicate the start of a sequence of 6 ion cloud acquisitions. Error bars were calculated by the square-root of the quadratic sum of the fit and calibration uncertainties. The green line indicates the average wavelength 271.6911(3) nm, with the uncertainty as a light green band.

better resolve the line shape, or to confirm the existence of weak lines, it was often necessary to increase the signal-to-noise ratio by adding together many hours worth of data. For this purpose, individually calibrated spectra were added together and rebinned so that the final spectrum again had 2048 wavelength bins. Furthermore, this has the added advantage that the uncertainty due to the calibration was reduced by the square-root of the number of added spectra. Often, the calibration uncertainty was reduced so much as to be negligible compared to the fit uncertainty.

5.3.4 Fitting of lines with Zeeman components

For the fitting of Zeeman models to the observed lines, the wavelengths in nm were converted to energies in eV using

$$E = \frac{hc}{\lambda_{\mathrm{vac}}}. \tag{5.3}$$

The recommended values for Planck's constant h and the speed of light c were taken from CODATA, $hc = 1239.841\,973\,9(76)$ nm eV [13]. The wavelength λ_{vac} used for the conversion is the wavelength in vacuum. Because the spectrometer was placed in air, the measured wavelengths needed to be corrected for the refractive properties of air. The refractive index of air n_{air} depends on factors such as air pressure and humidity, which were not closely monitored during the measurements. However, the reference lines used for the calibration were taken under well controlled conditions [144, 145]. So those wavelengths in air can be converted to wavelengths in vacuum using [146, 147]

$$\lambda_{\mathrm{vac}} = n_{\mathrm{air}}\lambda_{\mathrm{vac}} \tag{5.4}$$

$$n_{\mathrm{air}} = 1 + 10^{-8}\left(8\,342.13 + \frac{2\,406\,030}{130 - S^2} + \frac{15\,997}{38.9 - S^2}\right) \tag{5.5}$$

$$\text{with} \quad S = \frac{1000}{\lambda_{\mathrm{air}}}. \tag{5.6}$$

The model for the line shapes was based on the following assumptions which were motivated in section 2.1.5. 1) Each spectral line has multiple Zeeman components with energy differences $\Delta E_Z(g_j^i, g_j^f)$ from the central transition energy E_0. 2) The relative intensities of the components within a Δm group are determined by Clebsch-Gordan coefficients. 3) The efficiencies of the setup for the two orthogonal linear polarizations are parametrized by A_0 and $A_{\pm 1}$. 4) The Zeeman components are convolved with a Gaussian function with a width w_G. The fit function based on these assumptions is

$$f(E_0, w_G, A_0, A_{\pm 1}, \mathrm{offset}) = \mathrm{offset} + \sum A_{\Delta m} \langle j_f (m_i + \Delta m) 1 \Delta m | j_i m_i \rangle^2 \cdot \mathrm{Gaussian}(E_0 + \Delta E_Z, w_G). \tag{5.7}$$

Here the sum is understood to be taken over all the transitions between the Zeeman levels. The g_j-factors that are needed to determine the energy differences ΔE_Z were calculated employing different techniques, see table 5.2. The two independently performed advanced calculations (Oreshkina and Bergengut) give results that are consistent at the level of 1%, which suggests that the predictions are accurate at this level. For well-resolved lines, the g_j-factors can be left as free fit parameters and thus extracted from the measurement. However, previous measurements found deviations between measurements and predictions at the 10% level [130]. In these cases both the g_j-factors of both upper and lower levels strongly deviated from the predictions. This can be explained by the fact that the two g_j-factors are correlated fit parameters. As shown in section 2.1.5, the difference between the g_j-factors determines the energy splitting within one Δm group, while the value of the individual

Table 5.2 Overview of g_j-factors calculated using the Landé g_j-factor equation (2.15), multi-configuration method with a Dirac-Fock-Strumian basis (Oreshkina), and a configuration interaction method (Begengut). The last column (Windberger) gives experimental results. Sometimes the experimental data yielded two inconsistent values, which are therefore both given.

		g_j		
State	Landé	Oreshkina [148]	Berengut [34, 149]	Windberger [130]
$^3F_4^o$	1.250	1.248	1.25	1.24(2)
$^3F_3^o$	1.083	1.049	1.032	1.045(8)
$^3F_2^o$	0.667	0.664	0.667	0.668(9)
$^1F_3^o$	1.000	1.029	1.051	1.03(2)
$^3H_6$	1.167	1.161	1.164	1.155(4)
$^3F_4$	1.250	1.136	1.138	0.99(2)
$^3H_5$	1.033	1.031	1.033	1.031(4), 0.95(4)
$^3F_2$	0.667	0.827	0.847	1.09(6)
$^1G_4$	1.000	0.990	0.995	0.84(2), 0.85(2)
$^3F_3$	1.083	1.081	1.083	0.97(7), 0.90(3)
$^3H_4$	0.800	0.917	0.917	0.77(2), 0.82(5)
$^1D_2$	1.000	1.127	1.132	1.36(6), 0.92(14)
$^1J_6$	1.000	1.000	1.003	
$^3P_1$	1.500	1.497	1.500	
$^3P_2$	1.500	1.205	1.188	

g_j-factors determines the splitting between the Δm groups. Hence, in general the predicted g_j-factors are taken to be accurate at the 1% level. If a large deviation is found by the fitting procedure, the g_j-factors of both upper and lower levels should deviate from the predicted values. Furthermore, the Gaussian widths, peak intensities, and the ratio of amplitudes $A_0/A_{\pm 1}$ can be compared to expected values.

The dispersion and resolving power of the grating is not linear, so the resolving power, and thus the line width depends on the wavelength of the measured line. To determine the line widths at various wavelengths, the lines of the Fe-Ar calibration spectrum were used. A parabola was fitted to the data to obtain a function for the line width over the whole optical range, see Fig. 5.10.

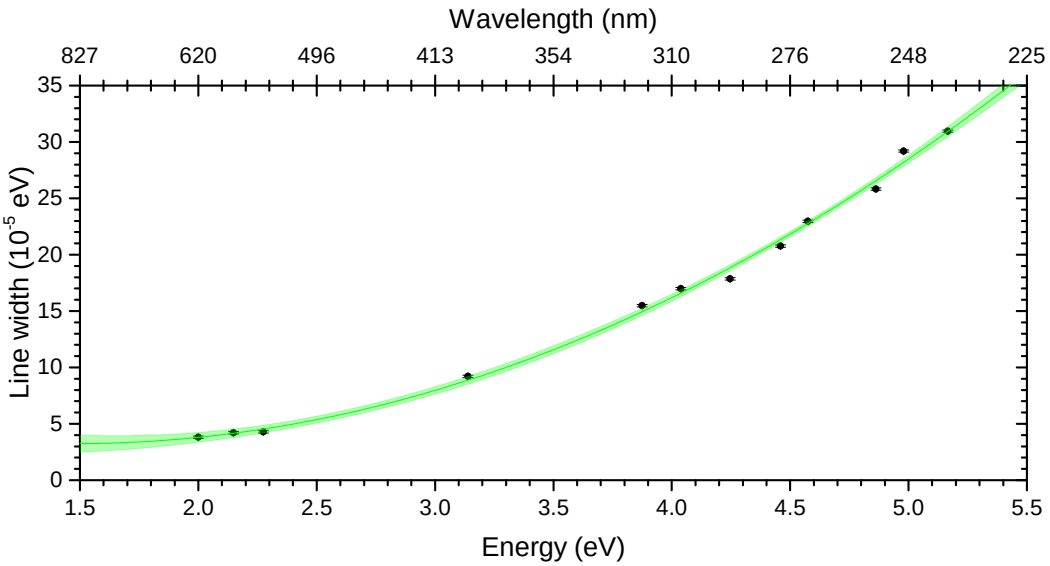

Fig. 5.10 Line widths as function of the line energy, determined using the Fe-Ar calibration lines. The green line shows the best fit of a parabolic function to the data with its 1σ confidence band. The fit yielded $f(x) = [8(3) - 6(2)x + 2.0(2)x^2] \cdot 10^{-5}$.

The uncertainty σ for the individual data points of a spectrum composed of n_{RO} acquisitions is estimated to be

$$\sigma = \sqrt{(\mathrm{Counts} - \mathrm{DC\ offset})^2 + n_{\mathrm{RO}}(N_{\mathrm{RO}}^{\mathrm{bin}})^2}. \tag{5.8}$$

The DC offset is a property of the CCD. It concerns a potential bias added to the input of the ADC during the read-out phase to ensure that it is never at its lower limit of zero signal. Although the offset should be stable, due to technical problems of the camera, over the course of hours fluctuations in the order of 100 counts were observed. These fluctuations could be corrected by comparing the baseline of spectra in a sequence.

Chapter 6

Measurement and interpretation of the optical spectra

In Ir^{17+} , the transitions with a high sensitivity to a variation of the fine-structure constant α are those that take place between the $4f^{14}$, $4f^{13}5s^1$, and $4f^{12}5s^2$ configurations. As a result of configuration mixing, there are E1 tranisitons taking place between them. However, due to the small overlap between the wave functions of the configurations, their transition rates are typically $10\,s^{-1}$ or less. This low rate makes them suitable for precision laser spectroscopy. It also means that the transitions are difficult to observe. The optical transitions to the $4f^{14}$ configuration all require a change of total angular momentum $\Delta J \geq 2$, and are therefore thought to be too weak to be observed with the methods employed in this work. Several optical electric-dipole (E1) transitions between the $4f^{13}5s^1$, and $4f^{12}5s^2$ configurations are expected to be strong enough to be observed, and are at the focus of this chapter. In earlier work of our group, 11 magnetic dipole (M1) transitions taking place between fine-structure levels of the same configuration were identified, see Fig. 6.1. Here, the remaining optical M1 transitions were measured. These can be used in the search for so-called Rydberg-Ritz combinations, where several measured transition energies can form a combination that adds up to zero; that is, they form a closed optical cycle. When a Rydberg-Ritz combination is found that includes previously identified transitions, the assignment of the unidentified lines can often be inferred. This requires a high accuracy of the energy measurements in order to exclude fortuitous agreements. Here, the techniques described in chapter 5 are employed to search for and to measure several weak lines in the Ir^{17+} spectrum. Unidentified lines were tested for Rydberg-Ritz combinations that include interconfiguration transitions. Several E1 candidates were found, the line shapes were tested for their agreement with the Zeeman models.

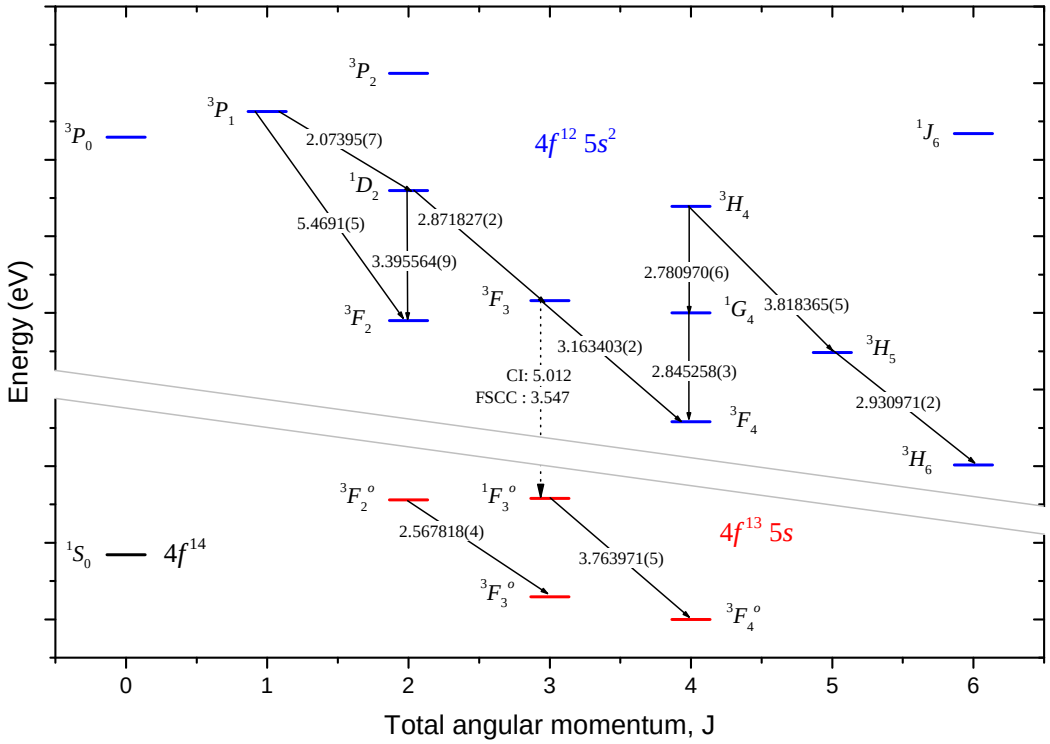

Fig. 6.1 Grotrian level scheme of the $4f^{14}$ (black), $4f^{13}5s$ (red), and $4f^{12}5s^2$ (blue) configurations of Ir^{17+} . The black arrows indicate the M1 transitions that were identified in the work of Windberger *et al.*, transition energies are indicated in eV [34, 130]. The splitting between the configurations was not yet known. Predictions for the energy of the $^3F_3$ - $^1F_3^o$ transition based on Fock space coupled cluster (FSCC) and configuration interaction (CI) calculations are shown at the dashed arrow [34, 27]. For the $4f^{14}$ $^1S_0$ level energy there are equally large discrepancies between predictions.

6.1 Overview of precision spectra

Based on available calculations, the E1 transitions between the $4f^{13}5s^1$ and $4f^{12}5s^2$ configurations were expected to be in the ultraviolet (UV) range, examples are given in section 6.3.2. Additionally, most of the previously unidentified lines have wavelengths in the UV. The E1 candidates suggested in our earlier work are also in the UV range [34]. Therefore, spectra in the range from 230 nm to 330 nm were measured. In the search for M1 lines, the region around 395 nm was also investigated. All the spectra were obtained as described in chapter 5. The most important parameters are: electron beam current $I = 40$ mA, spectrometer entrance slit width $W_s = 70\,\mu$m, acquisition time for a single spectrum $t_s = 30$ min.

Overviews of the recorded spectra are shown in Fig. 6.2, 6.3, and 6.4. For these overview spectra, the intensity offset was subtracted and the square-root of the intensity is shown instead of the intensity itself. Visually, this emphasizes weak lines that might otherwise go

unnoticed. Binning artifacts can be noticed in the background noise, rebinning of the data did not significantly change this.

The assignment of charge states is based on previous work where the electron beam was scanned while monitoring the intensity behavior of the lines. Lines that were not observed in previous measurements were marked as unassigned. They could have two causes: Ir^{17+} lines that were previously not observed because they were too weak, or contaminants in the ion sample. Normally, the contaminants are quickly expelled from the trap by means of evaporative cooling. However, some measurements were performed while, unknowingly at the time, the Macor isolator of the electron gun was damaged. This made the electron beam slightly unstable, but not unusable. Consequently, an excess of contaminants could have been introduced in the trap. For example, due to electrical discharges, material of the Macor (Si, Mg, Al, K, B, F, and O) could have been ionized and trapped. Since in the literature no values were found for optical transitions of highly charged ions of the suspected contaminants, it was not possible proof this hypothesis with the current measurements. Not all spectra were taken with a damaged electron gun isolator, only the spectra starting at 229 nm, 244 nm, and 261 nm were affected.

The Ir^{17+} lines and the unassigned ones were fitted to determine their central wavelengths. The results are summarized in table 6.1. Since identifications of the lines could not be made yet, Gaussian instead of Zeeman functions were fitted to the lines. Consequently, the uncertainties on the wavelengths could be improved if the proper Zeeman model were to be fitted. Lines without a central peak, but instead two strong peaks symmetrically around a central wavelength were fitted with two Gaussian functions. The average of the two line centers was then taken to be the central wavelength. Some of the unassigned lines were excluded because they were most probably due to the previously described contaminants in the trap. For example, the line near 240.1 nm appears in a spectrum that was taken when the electron gun isolator was broken but could not be reproduced after the isolator was repaired.

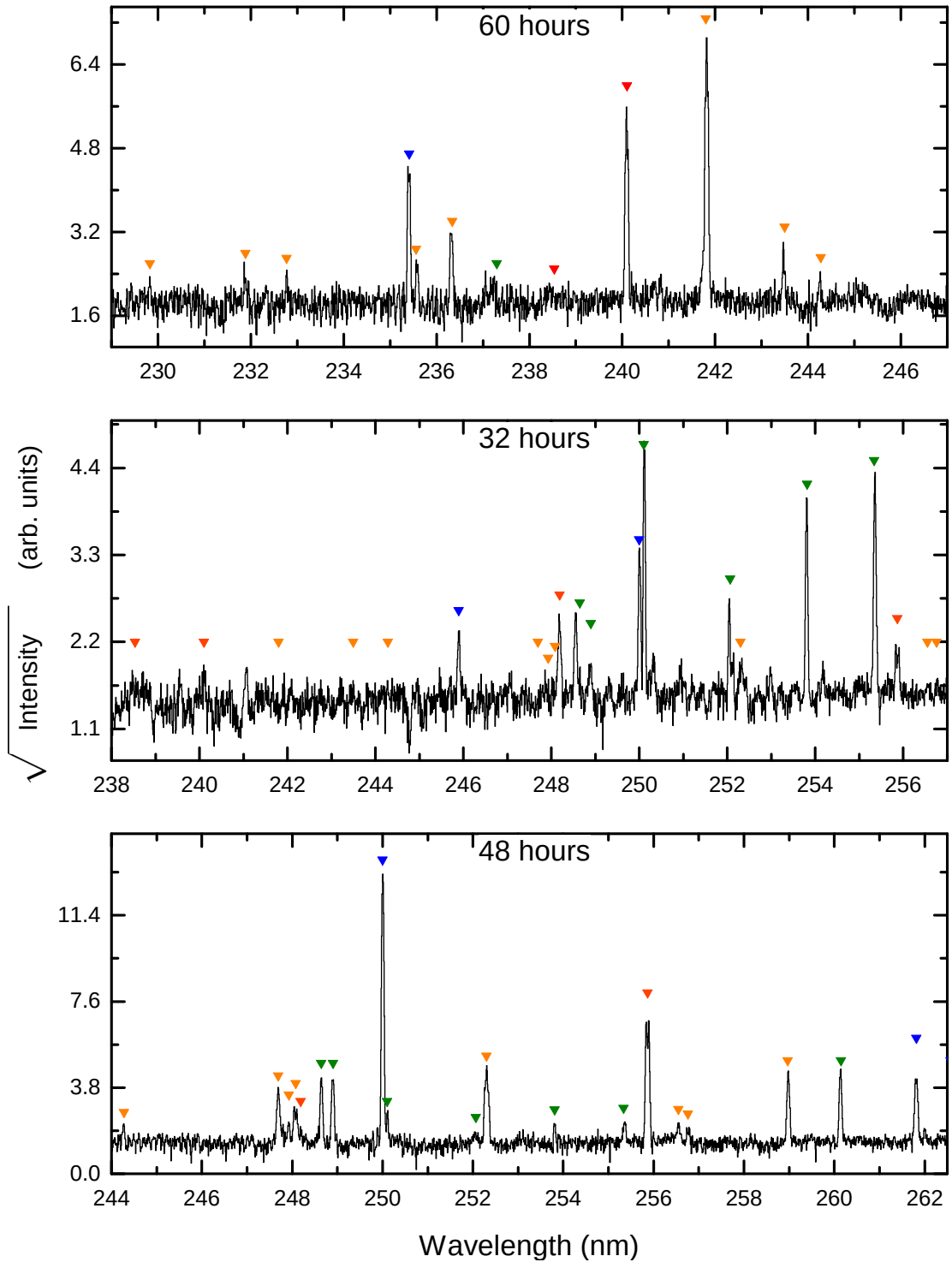

Fig. 6.2 Overview spectra taken at consecutive spectral ranges. The intensity offset was subtracted and the square-root of the intensity is taken to emphasize weak lines. The cumulative acquisition time is indicated at the top of each spectrum. The position of lines are indicated by triangles that are colored according to their charge state assignment Ir^{16+} (green), Ir^{17+} (red), Ir^{18+} (blue), unknown (orange).

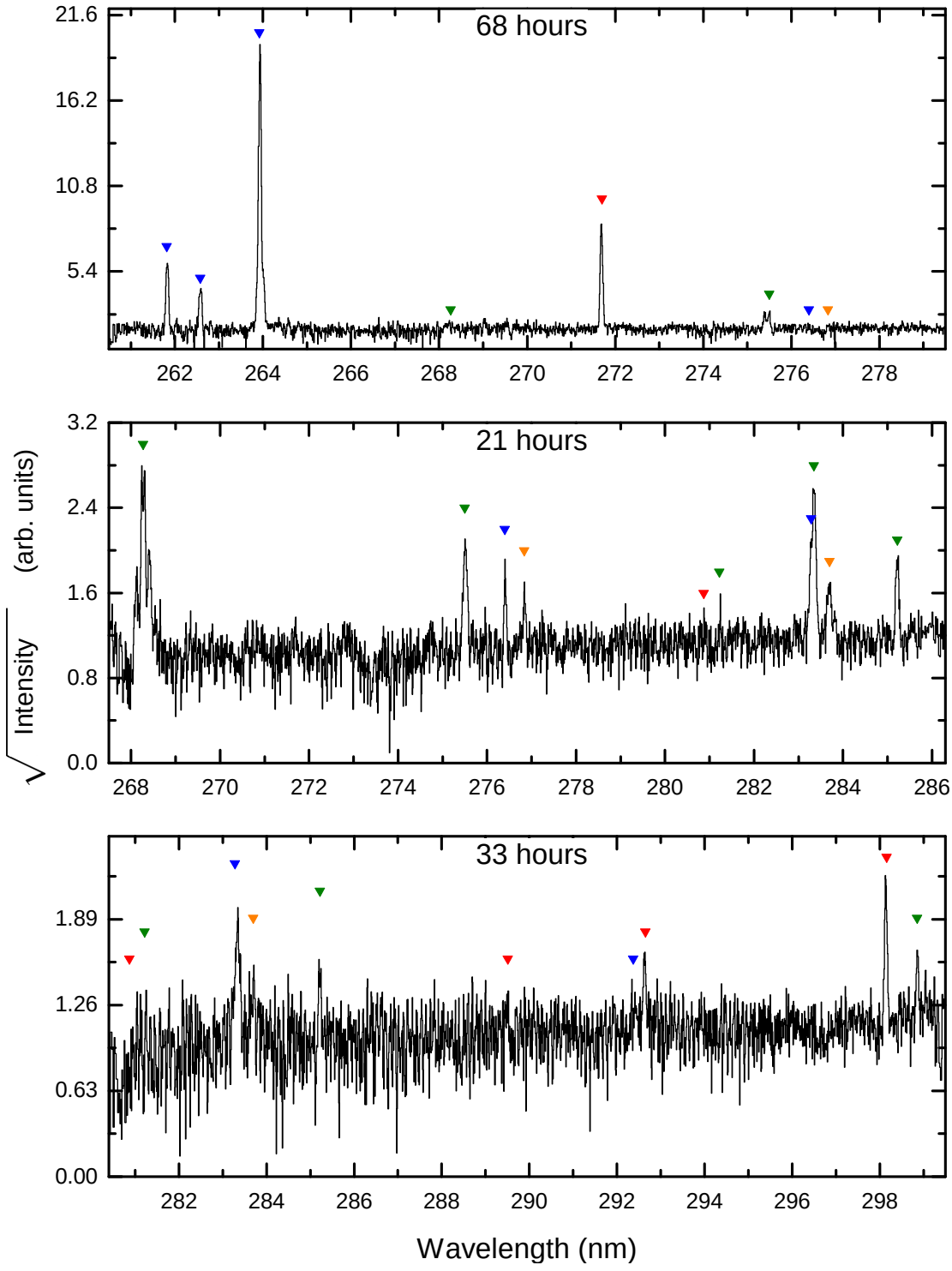

Fig. 6.3 Overview spectra taken at consecutive spectral ranges. The intensity offset was subtracted and the square-root of the intensity is taken to emphasize weak lines. The cumulative acquisition time is indicated at the top of each spectrum. The position of lines are indicated by triangles that are colored according to their charge state assignment Ir^{16+} (green), Ir^{17+} (red), Ir^{18+} (blue), unknown (orange).

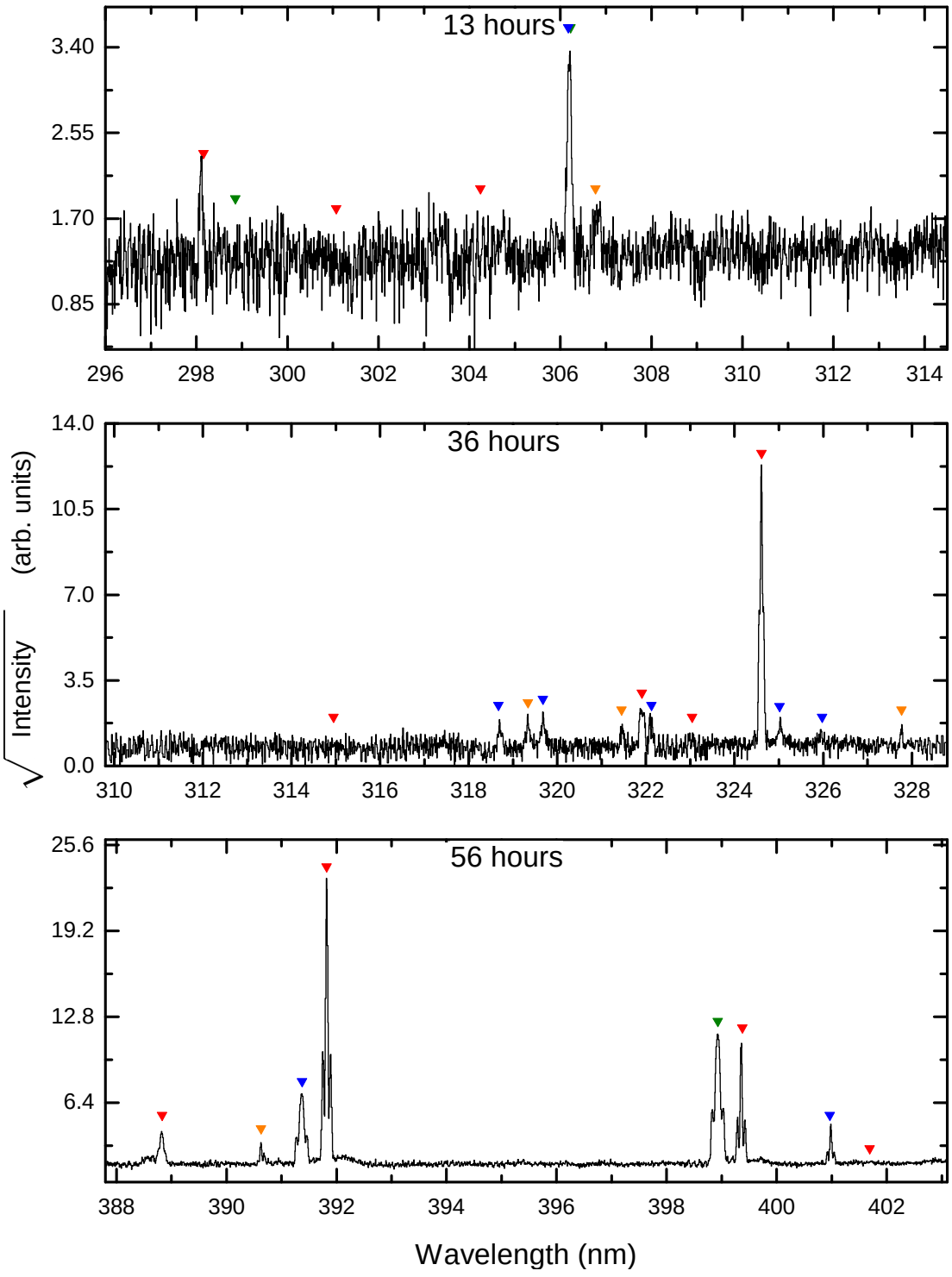

Fig. 6.4 Overview spectra taken at consecutive spectral ranges. The intensity offset was subtracted and the square-root of the intensity is taken to emphasize weak lines. The cumulative acquisition time is indicated at the top of each spectrum. The position of lines are indicated by triangles that are colored according to their charge state assignment Ir^{16+} (green), Ir^{17+} (red), Ir^{18+} (blue), unknown (orange).

Table 6.1 List of spectral lines of Ir^{17+} . The wavelengths are given in air, the energies were calculated using equation (5.5). Wavelengths set in bold face belong to lines with a double peak; wavelengths marked with a † belong to lines of which the charge state identification was ambiguous. Previously identified lines are marked in the corresponding column. For completeness, lines reported only in the work of Windberger *et al.* are also included in this list and marked in the Source column [34]. The column named Prev. obs. indicates that a line was also found in earlier work.

Wavelength (nm)	Energy (eV)	Identified	Source	Prev. obs.
226.63(2)	5.4691(5)	yes	[34]	yes
229.827(5)	5.3930(1)			
231.876(5)	5.3454(1)			
232.775(3)	5.32471(6)			
235.582(3)	**5.26127(6)**			
236.324(2)	5.24475(4)			
238.45(2)†	5.1980(4)			yes
240.098(1)	5.16233(2)			yes
243.476(2)	5.09071(4)			
244.261(4)	5.07435(8)			
248.077(2)	**4.99630(4)**			yes
252.306(1)	4.91256(2)			
255.8684(3)	**4.844170(6)**			yes
256.553(3)	4.83124(5)			
256.767(3)	**4.82722(6)**			
258.9831(5)	4.785915(9)			
271.6909(2)	4.562076(3)			yes
280.87(2)	4.4130(3)			yes
289.49(1)	4.2816(2)			yes
292.634(4)	**4.23559(5)**			yes
298.142(1)	4.15735(2)			yes
301.07(2)	4.1169(3)		[34]	yes

(Continued on next page).

Table 6.1 (Continued from previous page) List of spectral lines of Ir^{17+} .

Wavelength (nm)	Energy (eV)	Identified	Source	Prev. obs.
304.24(2)	4.0740(3)		[34]	yes
306.82(1)	4.0398(1)			
314.95(2)	3.9355(2)		[34]	yes
319.342(2)	3.88137(3)			
321.464(5)	3.85574(5)			
321.913(3)	3.85037(3)			yes
323.022(7)	**3.83715(8)**			yes
324.6099(4)	3.818381(5)	yes		yes
327.771(2)	3.78156(3)			
329.3025(4)	3.763971(5)	yes	[34]	yes
365.0318(10)	3.395564(9)	yes	[34]	yes
386.655(5)	**3.20567(4)**			yes
388.824(1)	3.18779(1)			yes
390.630(1)	3.17306(1)			yes
391.8237(4)	3.163389(4)	yes		yes
399.3577(6)	3.103712(4)			yes
401.69(2)	3.0857(2)		[34]	yes
422.8950(3)	2.930971(2)	yes	[34]	yes
431.6044(3)	2.871827(2)	yes	[34]	yes
435.6348(5)	2.845258(3)	yes	[34]	yes
445.7057(9)	2.78097(6)	yes	[34]	yes
482.7039(7)	2.567818(4)	yes	[34]	yes
503.283(2)	2.46282(1)	yes		yes
545.83(2)	2.27085(8)		[34]	yes
577.57(2)†	**2.14606(7)**		[34]	yes
597.65(2)	2.07395(7)	yes	[34]	yes

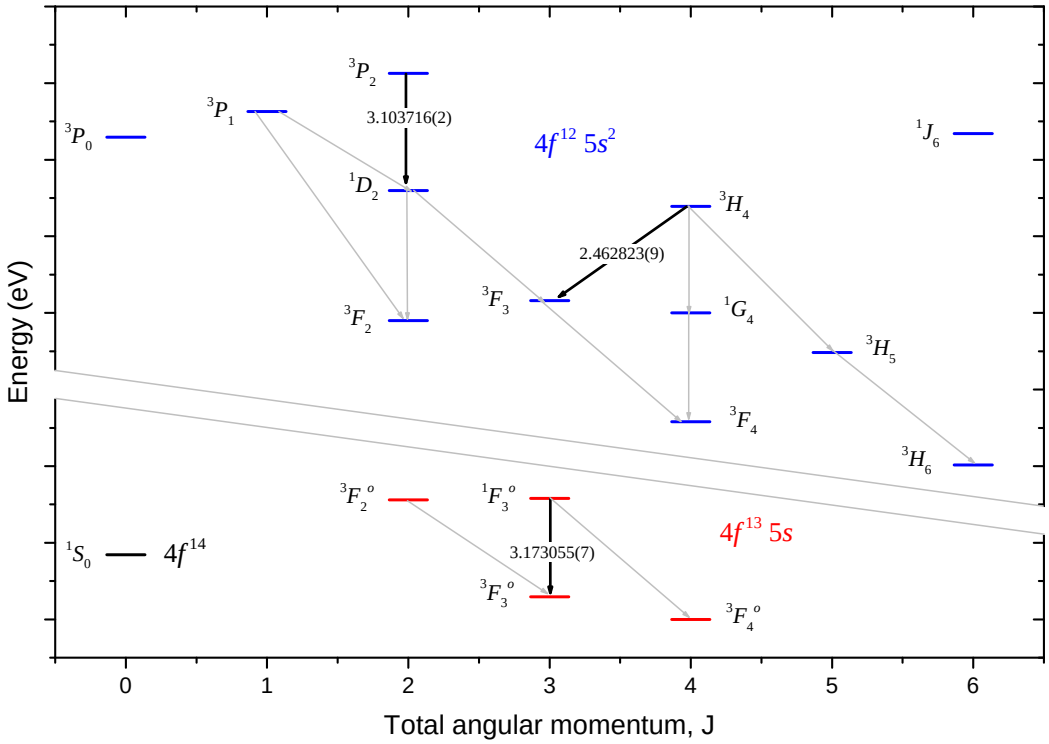

Fig. 6.5 Grotrian level diagram of Ir^{17+} with all the optical M1 transitions indicated. The black arrows indicate those that were measured in this work, the gray arrows the ones that were measured in the work of Windberger *et al.* [34].

6.2 Identification of missing M1 lines

Several optical M1 transitions had not been measured yet. In this section, the proven accuracy of the FSCC method is used to guide the search for them. One of the key transitions missing in earlier work is the $^1F_3^o$ - $^3F_3^o$ transition. Its importance arises from the fact that it completes our understanding of the fine structure of the $4f^{13}5s^1$ configuration. Additionally, the $^3H_4$–$^3F_3$ and $^3P_2$ - $^1D_2$ transitions were predicted to be in the optical range, but were not found in earlier work. In Fig. 6.5 an overview of the optical M1 transitions is shown. Identification of them helps to search for E1 lines because additional possibilities for Rydberg-Ritz combinations with known transitions are obtained.

6.2.1 Identification of the $^1F_3^o$–$^3F_3^o$ transition

The hitherto unidentified $^1F_3^o$–$^3F_3^o$ transition was predicted to be at 391.6(3.4) nm based on calculations performed using the FSCC method. Since the FAC calculations predict the transition rate to be 9 s^{-1}, the spectral line is expected to be weak. Therefore, approximately 56 hours of data were taken in the region around 395 nm, see Fig. 6.4. Two previously

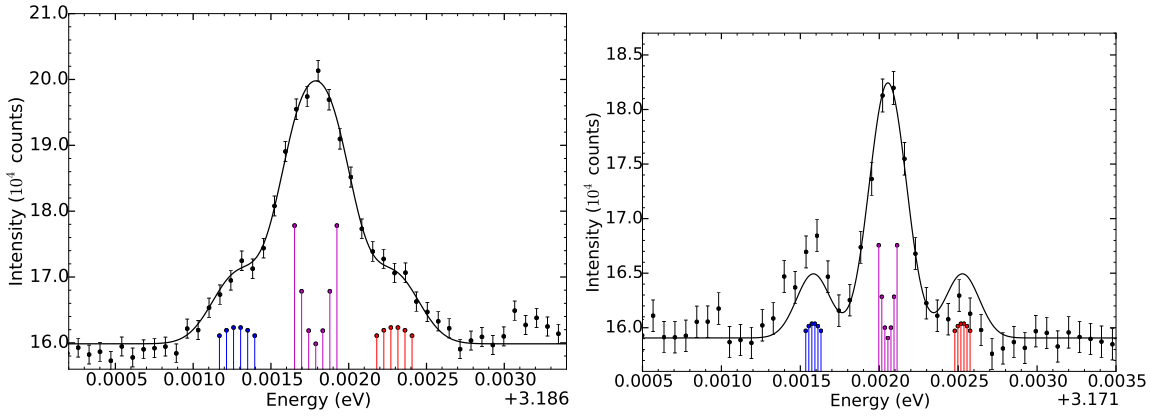

(a) 388.9349(9) nm (b) 390.7408(9) nm

Fig. 6.6 Fit of the Zeeman model for the $^1F_3^o$–$^3F_3^o$ transition to two candidates. Blue, magenta, and red circles indicate the positions of the individual Zeeman components $\Delta m = +1$, $\Delta m = 0$, $\Delta m = -1$ respectively. Further fit details are given in table 6.2.

unidentified lines at approximately 388.9 nm and 390.7 nm were both candidates for this transition. The Zeeman model for the $^1F_3^o$ – $^3F_3^o$ transition was fitted to both lines, see Fig. 6.6 and table 6.2 for the fit results.

Both lines have similar structures, with a strong central peak and two weaker neighboring peaks. However, due to minor differences between the peaks, the fits yield slightly different results. The values found for the g_j-factors and for the line widths of the 390.7 nm line are in much better agreement with the expected values than those of the 388.9 nm line. Additionally, the reduced χ^2 for the line near 390.7 nm is slightly better, but that is mainly due to the higher relative uncertainty of those data points. The energies of both lines are within 1-σ of the predicted value. However, the line near 390.7 nm is nearest to it; because of this and the good agreement of the g_j-factors, this line is tentatively identified as the $^1F_3^o$–$^3F_3^o$ transition.

6.2.2 Identification of the $^3P_2$ - $^1D_2$ transition

The strong Ir^{17+} line at approximately 399.4 nm was not identified thus far. Based on the FSCC calculations, it is likely that this line corresponds to the $^3P_2$ - $^1D_2$ transition, which is predicted to be at 398.9(3.4) nm. The FAC results for the transition rate are 214 s^{-1}. Another candidate for this transition was found at 401.69(2) nm in earlier work [130]. However, it does not appear in the spectra recorded during this work, refer to Fig. 6.4. Possibly, the line at 401.69(2) nm was previously misattributed to Ir^{17+} . The possibility that the line was due to a weak Ir^{17+} transitions seems unlikely, since the duration of the measurements performed in this work was much increased compared to earlier work.

Table 6.2 Fit results for the $^1F_3^o$–$^3F_3^o$ transition.

Property	Measured		Expected
	388.9 nm	390.7 nm	
Line center	3.187 788(7) eV	3.173 055(7) eV	3.166(30) eV
Line widths	14.4(2.0)·10^{-5} eV	10.3(2.0)·10^{-5} eV	9.2(3) · 10^{-5} eV
A_0 / $A_{\pm1}$	4.9(7)	4(1)	
g_j initial	1.16(4)	1.00(4)	1.051
g_j final	1.02(4)	1.04(4)	1.032
Offset	15 985(21) counts	15 906(25) counts	
Reduced χ^2	1.40	1.18	

Several fits of the Zeeman model for the $^3P_2$ - $^1D_2$ transition were made to the line near 399.4 nm, see Fig. 6.7. The Zeeman model with all its parameters free gave the best reduced χ^2 of 1.1. However, because the resolving power of the spectrometer was not good enough, a reliable value for the g_f-factors could not be found. Namely, both g_j-factors were found to have a value of 1.1(5.5). As discussed in sections 2.1.5 and 5.3.4, the differences between the g_j-factors describes the splitting between the line components in a Δm group. If the difference is zero, only the splitting between the different Δm groups remains. In that case the model effectively describes only three wide Gaussian peaks. Other examples of this can be seen in Fig. 6.11 (a) and (c) of the forthcoming section 6.4.

The next Zeeman model fit that was performed had g_j-factors fixed at the values calculated by Berengut; results are shown in Fig. 6.7 and table 6.3. Although the line has the structure as expected from the Zeeman model, the shape is not reproduced very well, as indicated by the poor reduced χ^2. A fit with fixed g_j-factors as calculated by Oreshkina gave a worse reduced χ^2 of 9.2. Subsequently, a fit with free g_j-factors but fixed line widths was performed, see Fig. 6.7 and table 6.3. The found g_j-factors both deviate by approximately 4% from the calculated values, which is not particularly excessive compared to some of the deviations found in previous work [130]. Combined with the acceptable reduced χ^2; the predicted transition rate of 214 s^{-1} and the fact that no other lines are present in the range predicted by the FSCC calculations, it can be concluded that the $^3P_2$ - $^1D_2$ transition was identified.

6.2.3 Identification of the $^3H_4$–$^3F_3$ transition

The $^3H_4$–$^3F_3$ transition could be used to test the accuracy of the measurements compared to previous work [34]. Its energy can be deduced from the previously measured $^3H_4$–$^1G_4$,

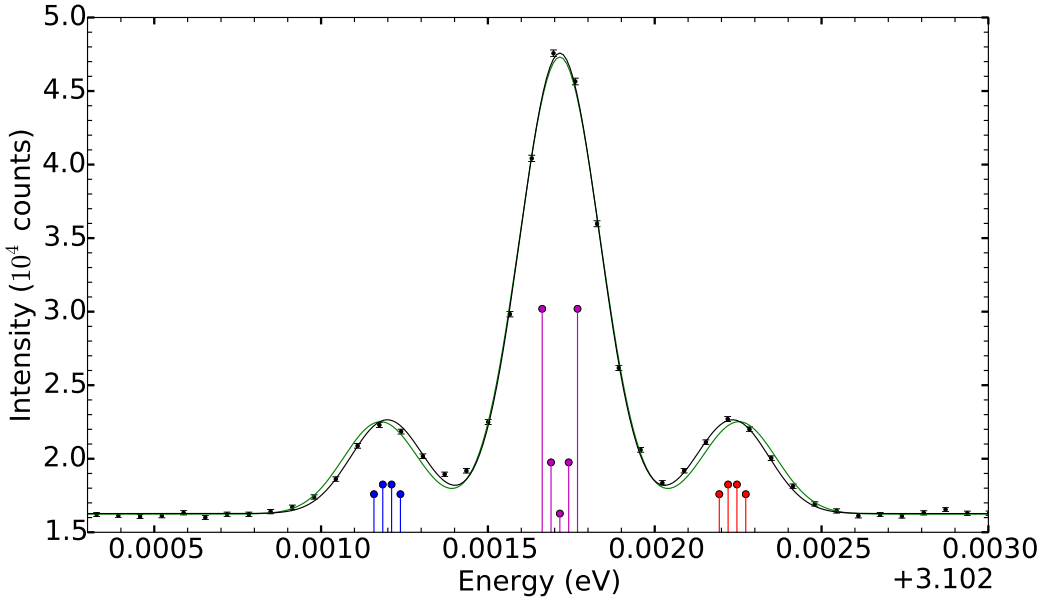

Fig. 6.7 Results for the measurement (black squares) of the line at approximately 399.4702(3) nm. The Zeeman model fit with fixed line widths gave the best fit result (black line). The fit based on the Zeeman model with fixed g_j-factors as calculated by Berengut is also shown (green line). Blue, magenta, and red circles indicate the positions of the individual Zeeman components $\Delta m = +1$, $\Delta m = 0$, $\Delta m = -1$ respectively. Further fit details are given in table 6.3.

Table 6.3 Results for two types of fits of the $^3P_2$ - $^1D_2$ transition, see text. The * indicate which parameters were kept fixed during the fitting process.

Property	Measured		Expected
	Fixed g_j-factors	Fixed width	
Line center	3.103 716(2) eV	3.103 716(2) eV	3.108(30) eV
Line widths	$10.9(1)\cdot10^{-5}$ eV	$9.2\cdot10^{-5}$ eV*	$9.2(3)\cdot10^{-5}$ eV
A_0 / $A_{\pm1}$	5.3(2)	5.3(1)	
g_j initial	1.188*	1.146(5)	1.188
g_j final	1.132*	1.089(5)	1.132
Offset	16237(55) counts	16273(35) counts	
Reduced χ^2	4.48	1.9	

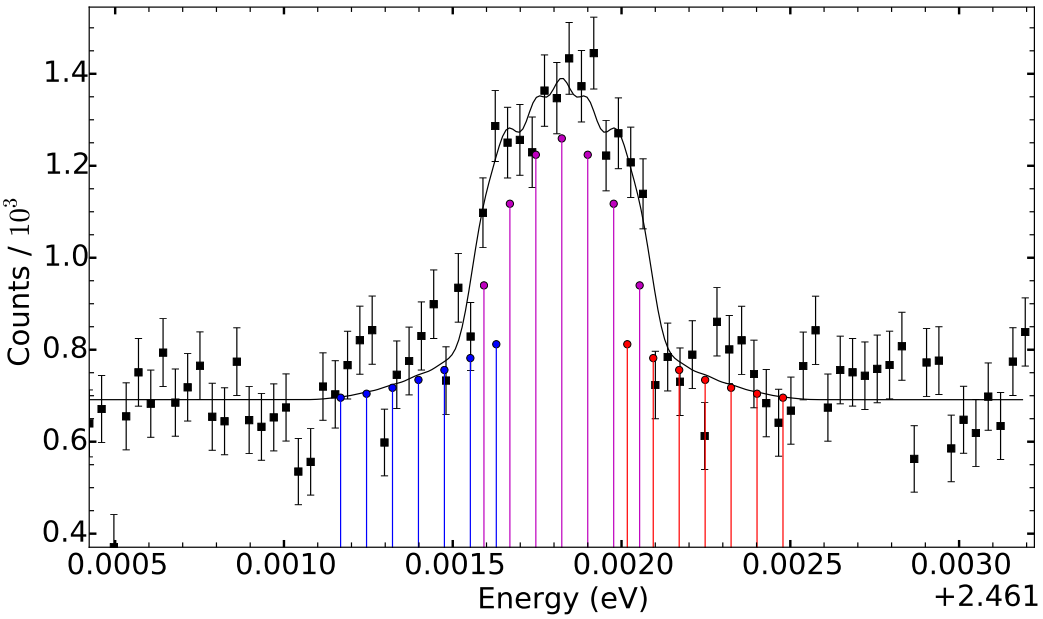

Fig. 6.8 Results for the measurement of the $^3H_4$ - $^3F_3$ transition. The black squares show the results of 55.5 hours of measurement at 503.423(2) nm. The fit of the Zeeman model for the $^3H_4$ - $^3F_3$ transition (black line) has a reduced $\chi^2 = 1.52$. Blue, magenta, and red circles indicate the positions of the individual Zeeman components $\Delta m = +1$, $\Delta m = 0$, $\Delta m = -1$ respectively. Further fit details are given in table 6.4

$^1G_4$–$^3F_4$, and $^3F_3$–$^3F_4$ transitions, with which it forms a Rydberg-Ritz combination. This transition at approximately 503 nm has a predicted rate of 11 s^{-1}. This value is an order of magnitude lower than one of the weakest lines ($^3H_4$–$^1G_4$ wit a predicted rate of 105 s^{-1}) identified in the work of Windberger *et al.*. In total 111 spectra were obtained in the region around 503 nm at an electron beam current of 40 mA, refer to Fig. 6.8 for the results.

At the expected wavelength, a weak line appears above the noise. The Zeeman model for the $^3H_4$ - $^3F_3$ transition was fitted to the line, see table 6.4 for the results. The statistics were insufficient to determine the g_j-factors with the fit, thus they were kept fixed at the values calculated by Berengut [149]. The obtained line width is consistent with previous experiences. The central energy of the line could be determined with a precision of 3.7 ppm, and is in excellent agreement with the prediction based on the work by Windberger *et al.*.

6.3 Search for interconfiguration E1 lines

So far, all the M1 transitions in the $4f^{13}5s^1$ and $4f^{12}5s^2$ configurations that are predicted by FSCC calculations to be in the optical range were measured. This leaves 34 of the lines

Table 6.4 Fit results for the $^3H_4$–$^3F_3$ transition.

Property	Measured	Expected
Line center	2.462 823(9) eV	2.462 825(7) eV
Line width	$3.7(1.0)\cdot10^{-5}$ eV	$5.2(3)\cdot10^{-5}$ eV
A_0 / $A_{\pm1}$	8(4)	
Offset	690(10) counts	
Reduced χ^2	1.52	

listed in table 6.1 unidentified. In this section, an attempt to identify these lines is made, with the goal of finding interconfiguration E1 transitions.

6.3.1 Exclusion of E2 transitions

Before attempting to identify any of the lines as E1 transitions, a search for higher order multipole transitions was made. The selection rules for higher order multipole transitions differ from those for E1 and M1 transitions. For example, electric quadrupole (E2) transitions require no parity change and allow for $\Delta J = \pm 2$ [49]. Generally, the rates for optical transitions other than E1 and M1 are thought to be too low to be observed in an EBIT. However, to fully exclude the existence of such transitions in the measured spectra, a search for these type of transitions was performed. Almost all the energy differences between two fine-structure levels within the same configuration could be inferred from the previous identifications of M1 lines. These values were compared to the unidentified lines, no matches were found.

Another possible source of lines in the optical spectrum of Ir^{17+} are transitions taking place within, or between, the $4f^{12}5s^15p^1$ and $4f^{13}5p^1$ configurations. In section 4.6, transitions from these more energetic configurations to the here investigated $4f^{13}5s^1$ and $4f^{12}5s^2$ configurations were identified. However, the identified EUV transitions are so strong that optical transitions from the corresponding upper levels are suppressed. Hence, the energies of optical transitions in the $4f^{13}5s^1$ and $4f^{12}5s^2$ configurations could not be inferred.

6.3.2 Ryberg-Ritz principle for E1 lines

As is show in Fig. 6.1, the predictions for the energy difference between the $4f^{13}5s^1$ and $4f^{12}5s^2$ configurations disagree by several eV. In table 6.5 a more complete overview of the available predictions for interconfiguration lines is shown. In total there are 24 possible E1 transitions between the $4f^{13}5s^1$ and $4f^{12}5s^2$ configurations. Depending on the energy

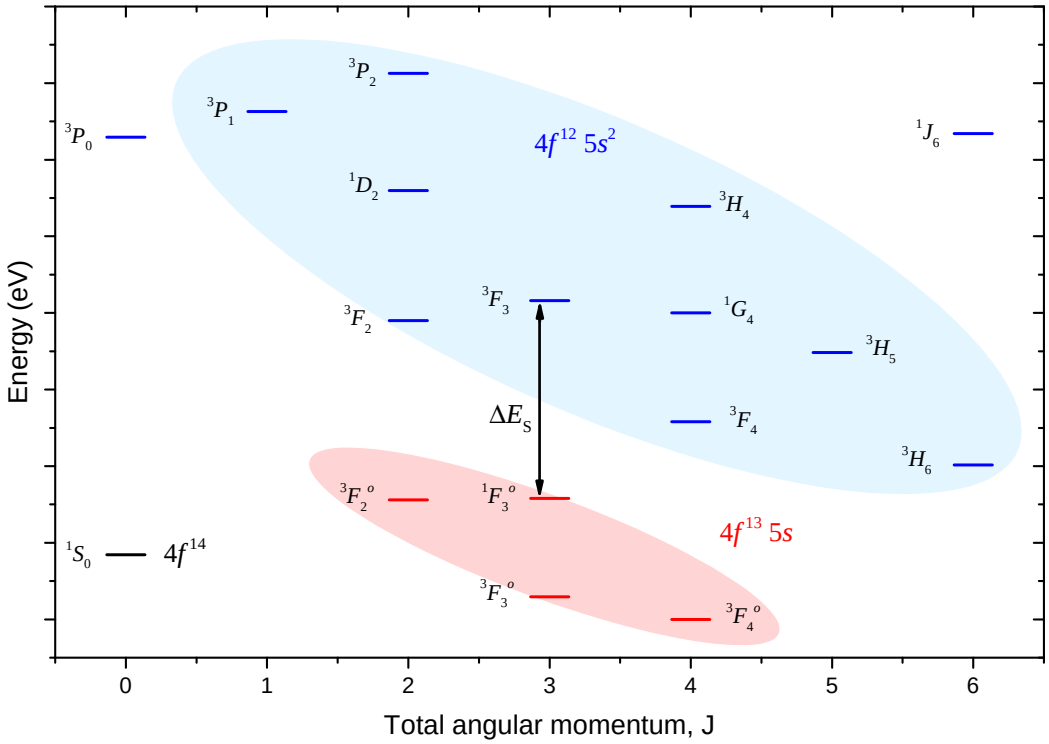

Fig. 6.9 Grotrian level scheme illustrating the scan of the energy splitting ΔE_S between the $4f^{13}5s^1$ and $4f^{12}5s^2$ configurations. The levels in the blue ellipse were shifted relative to levels in the red ellipse. The possible E1 transitions were compared to the measured lines, when two or more agreements were found, the corresponding ΔE_S value was added to table 6.6.

splitting between the configurations, only some can be in the optical range. Based on predictions made with CRM, there are always two or more relatively strong optical transitions to be expected, refer to section 6.5 for an example. This can be exploited to determine which of the unidentified lines are E1 candidates. Namely, for a line to be a candidate, there needs to be at least one more candidate that is consistent with the first candidate. Based on this premise, an automated search for E1 candidates was performed.

The process starts with defining the energy splitting between the $4f^{13}5s^1$ and $4f^{12}5s^2$ configurations, see Fig. 6.9. The $^3F_3$–$^1F_3^o$ transition was arbitrarily chosen to represent this. All the fine-structure level energies of the $4f^{13}5s^1$ configuration are known with respect to the $^1F_3^o$ level. This is not completely the case for the $4f^{12}5s^2$ configuration and its $^3F_3$ level. However, the energies of those levels that can decay by means of E1 transitions are all known with respect to the $^3F_3$ level. The energy splitting $\Delta E_S = E(^3F_3) - E(^1F_3^o)$ was varied from 0.0 eV to 7.5 eV in steps of $1.5 \cdot 10^{-6}$ eV, which is half of the smallest uncertainty of a measured line. At each step the energies of the 24 possible E1 transitions were calculated

Table 6.5 Examples of interconfiguration E1 transitions and their predicted transition energies given in eV. The top row of FAC results were found to give relatively good results for the intraconfiguration M1 transitions, but showed strong discrepancies with the in this work identified EUV transitions. The bottom row of FAC results were obtained in this work, and showed agreement at the 1%-level with the measured EUV transitions. In this chapter, optical spectra in the range from approximately 3.76 eV to 5.21 eV were measured.

Source	$^3F_2$–$^3F_2^o$	ΔE_S	$^3F_3$–$^3F_3^o$	$^3F_4$–$^3F_4^o$
FAC [34]	9.750	9.597	12.819	10.043
CI [27]	5.241	5.012	8.317	5.606
COWAN [34]	4.665	4.762	8.033	5.249
CIDFS [34]	4.374	4.128	7.312	4.748
FSCC [34]	3.701	3.547	6.713	4.159
FAC	3.455	3.243	6.616	3.881

and compared to the list of unidentified lines. If the difference between a predicted line and a measured line was less then 4 σ it was considered as being in agreement. When two or more agreements were found at the same ΔE_S, the corresponding spectral lines were marked as E1 candidates. The results of the scan are listed in table 6.6. A set of three or more candidates was not found, so only pairs of candidates are shown. Employing a similar technique for a smaller set of lines, Windberger *et al.* found two pairs of candidates [34]. The one that belongs to the Rydberg-Ritz combination $^3F_3 - ^1F_3^o - ^3F_4^o - ^3F_4$ with the E1 candidates at 271.6909(2) nm and 240.098(1) nm as could be excluded as a result of the increased precision obtained in this work.

For each pair of candidates, the combined uncertainty σ was calculated by taking the square root of the sum of squares of the individual uncertainties. Calculation of the rates of the transitions with FAC for each ΔE_S was computationally too time consuming. Therefore, the rates were only calculated at $\Delta E_S = 5.5$ eV. Using equation (2.18), i.e., the scaling of rates with the cube of the transition energy E_0^3, the rates were corrected at each ΔE_S.

Now that a list of E1 candidates was available, additional criteria were introduced. In section 6.2 it was shown that transitions with a predicted rate of approximately $10\,\mathrm{s}^{-1}$ are at the threshold of detectability with the employed setup. In the ultra-violet range, where most of the E1 candidates are, the efficiency of the spectrometer is reduced, refer to Fig. 5.2. Therefore, the candidates with a product of rates lower than $100\,\mathrm{s}^{-2}$ could safely be discarded. The main criterion for candidates is that the measured line shapes should correspond to the the predicted line shapes. An overview of the predicted line shapes is given in appendix A. By

Table 6.6 Overview of candidates with a combined uncertainty $\sigma < 4$ for interconfiguration E1 transitions. The energy difference between the $4f^{13}5s^1$ and $4f^{12}5s^2$ configurations ΔE_S, and the transition energies, are given in eV. The * indicates candidates that are known as Case 2 in the work of Windberger *et al.* [34]. Bold faced identifications (Id.) and energies indicate lines that have a double peak structure, c.f. table 6.1 and appendix A. The product of rates was based on FAC calculations and the scaling with E^3 of these rates.

ΔE_S	Transition 1		Transition 2		σ	Prod. of rates
(eV)	Id.	Energy (eV)	Id.	Energy (eV)		s^{-2}
5.1623*	$^1G_4$-$^1F_3^o$	**4.844170(6)**	$^3F_3$-$^1F_3^o$	5.16233(2)	0.57	23
4.5989	$\boldsymbol{^3F_4}$-$\boldsymbol{^3F_4^o}$	5.1980(4)	$^3F_2$-$^1F_3^o$	4.0740(3)	1.44	5255
4.2261	$^3F_4$-$^3F_3^o$	**4.23559(5)**	$^3F_3$-$^3F_2^o$	4.83124(5)	1.84	566
1.9893*	$^1G_4$-$^3F_3^o$	**4.844170(6)**	$^3F_3$-$^3F_3^o$	5.16233(2)	0.57	2061
1.9724	$^1G_4$-$^3F_3^o$	**4.82722(6)**	$^1D_2$-$^1F_3^o$	**4.844170(6)**	3.77	2436
1.6659	$^3H_5$-$^3F_4^o$	4.0740(3)	$^3F_3$-$^3F_2^o$	2.27085(8)	0.74	0
1.6544	$^3F_3$-$^3F_3^o$	**4.82722(6)**	$^3H_4$-$^1F_3^o$	4.1169(3)	0.39	1319
1.5411	$^3F_3$-$^3F_2^o$	**2.14606(7)**	$^1D_2$-$^1F_3^o$	4.4130(3)	1.60	88
1.4731	$^3H_5$-$^3F_4^o$	3.88137(3)	$^3H_4$-$^1F_3^o$	3.9355(2)	1.83	1
1.3984*	$\boldsymbol{^1G_4}$-$\boldsymbol{^3F_4^o}$	**4.844170(6)**	$^3F_3$-$^3F_4^o$	5.16233(2)	0.57	16199
1.0635	$^3F_3$-$^3F_4^o$	**4.82722(6)**	$^1D_2$-$^1F_3^o$	3.9355(2)	2.93	1857
0.6774	$^3H_5$-$^3F_4^o$	3.0857(2)	$^3F_3$-$^3F_3^o$	3.85037(3)	2.07	0

applying these two criteria to the candidates of table 6.6, only the pair at $\Delta E_S = 1.3984$ eV remains.

An additional argument to discard all the candidates except for the lines at 4.844 170(6) eV and 5.162 33(2) eV concerns the confidence in the classification of Ir^{17+} lines. The aforementioned contaminants of the ion sample were shown to contribute lines to the spectra. The only E1 candidates that were observed in both this work and the work of Windberger *et al.* are the lines at 4.844 170(6) eV and 5.162 33(2) eV. Considering all the arguments, the lines at 4.844 170(6) eV and 5.162 33(2) eV were subjected to further investigation.

6.4 Zeeman fits of the E1 candidates

The fits that were used to determine the wavelengths of the lines for table 6.1 were based on single or double Gaussian functions. Based on the new, tentative identifications of the lines at 4.844 170(6) eV and 5.162 33(2) eV, the corresponding Zeeman models can be fitted to the lines. As a test of the robustness and reliability of the Zeeman model fits, the lines were fitted with the Zeeman model for all three possible identifications of the lines, namely, for the most likely identification at $\Delta E_S = 1.3984$ eV, and for the two identifications at $\Delta E_S = 1.9893$ eV and $\Delta E_S = 5.1623$ eV. The results for all the fits are shown in Fig. 6.11.

Experience for the fits of the M1 transitions showed that sometimes, a Zeeman model fit with all the parameters left free did not give proper results. Therefore, all the fits were performed three times. Once with all the parameters of the model left free, once with fixed g_j-factors as calculated by Berengut, and once with the line widths fixed. In all cases, the fit with all the parameters left free yielded a satisfactory reduced χ^2, as the black lines in Fig. 6.11 illustrate. However, in the first two cases, where $\Delta E_S = 1.9893$ eV and $\Delta E_S = 5.1623$ eV, the results for the g_j-factors, the line widths, and the intensity ratios do not agree with the expected values. This can be seen from the individual Zeeman components. In the left upper and middle plots of Fig. 6.11, the Zeeman components in each Δm group exactly coincide. As explained in section 6.2.2, this can occur when the features of a line are not resolved well enough. However, in that case, the fit with fixed g_j-factors still resulted in a reasonably good fit. In the cases discussed here, the fits with fixed g_j-factors do not reproduce the data well, as the green lines in Fig. 6.11 demonstrate. The fits with the line widths fixed also did not yield a satisfactory reduced χ^2, as the orange lines imply. In the right upper and middle plots of Fig. 6.11 the g_j-factors as found by the Zeeman fit with all the parameters free are also nearly equal, as can be seen from the limited spread of the Zeeman components. Moreover, near zero values for the intensity of the central components A_0 were found. Although the efficiency of the setup for the linear polarizations is not known exactly, a full attenuation of

Table 6.7 Results for the fits of the Zeeman models corresponding to the $^1G_4$–$^3F_4^o$ and $^3F_3$–$^3F_4^o$ transition to the lines at 5.162 333(9) eV and 4.844 170(5) eV. These results were obtained for the Zeeman models with all the parameters left free.

Property	$^1G_4$–$^3F_4^o$		$^3F_3$–$^3F_4^o$	
	Measured	Expected	Measured	Expected
Line center	5.162 333(9) eV		4.844 170(5) eV	
Line widths	$24(3)\cdot10^{-5}$ eV	$30.8(5)\cdot10^{-5}$ eV	$22(2)\cdot10^{-5}$ eV	$26.3(3)\cdot10^{-5}$ eV
A_0 / $A_{\pm1}$	1.7(3)		0.9(3)	
g_j initial	1.10(20)	1.083	0.98(2)	0.995
g_j final	1.26(12)	1.250	1.31(2)	1.250
Offset	1958(9) counts		1349(7)	
Reduced χ^2	1.09		0.85	

one of the components is not expected. Furthermore, the fits with either the g_j-factors or the line widths fixed did not yield satisfactory reduced χ^2's.

The Zeeman model fits for the identifications at $\Delta E_S = 1.3984$ eV (bottom row of Fig. 6.11) consistently produced good results. The results of the fits for the Zeeman models with all the parameters left free are summarized in table 6.7. Except for the slight deviation of the g_j-factor of the $^3F_4^o$ state, the found g_j-factors are in excellent agreement with the values as predicted by Berengut.

Based on the good results for the Zeeman model fits and the fitting of the Rydberg-Ritz combination, the two lines at 4.844 170(5) eV and 5.162 333(9) eV could be tentatively identified. Since discrepancies with theory for the corresponding energy splitting ΔE_s between the $4f^{13}5s^1$ and $4f^{12}5s^2$ configurations is at the level of a few eV, additional investigation are required to obtain more confidence in the identifications. Based on the present ones, an overview of the Ir^{17+} level structure is given in Fig. 6.12. As shown, the sought-after energy of the ultra-narrow M2/E3 $4f^{12}5s^2\ ^3H_6$–$4f^{13}5s^1\ ^3F_4^o$ transition can be inferred to be at 1415.662(15) nm.

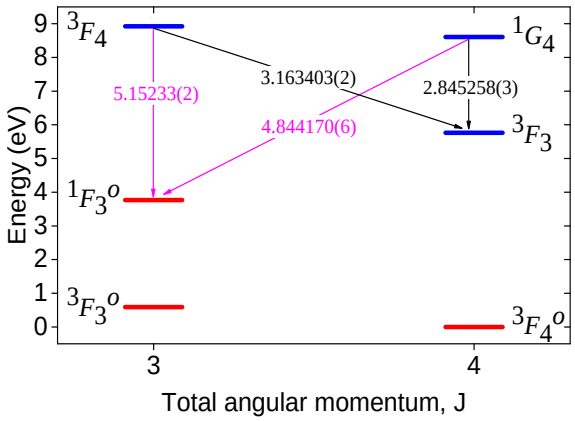

(a) $\Delta E_S = 5.1623$ eV

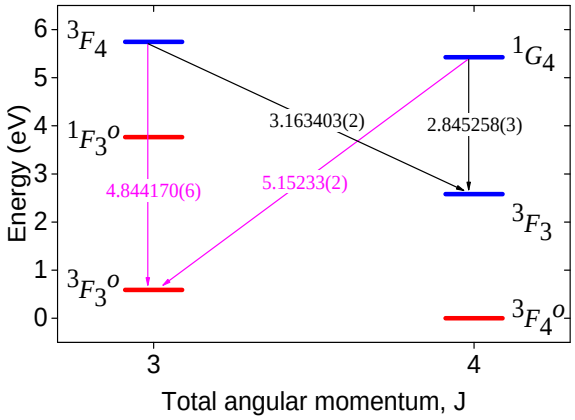

(b) $\Delta E_S = 1.9893$ eV

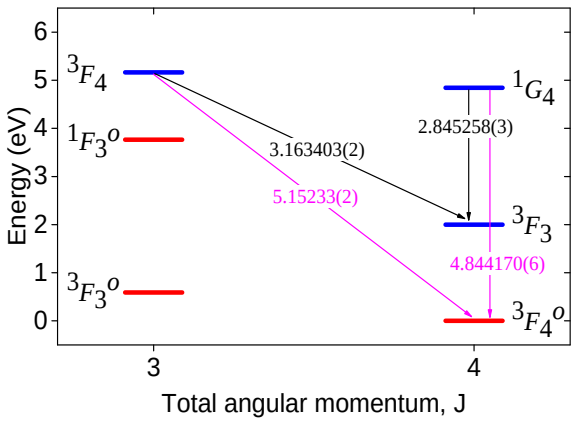

(c) $\Delta E_S = 1.9893$ eV

Fig. 6.10 Grotrian level schemes for the three Rydberg-Ritz combinations that can be made with the lines at 4.844 170(6) eV, 5.162 33(2) eV, 3.163 403(2) eV, and 2.845 258(3) eV for different values of ΔE_S. The corresponding Zeeman fits of the E1 candidates at 4.844 170(6) eV and 5.162 33(2) eV are shown at the right page.

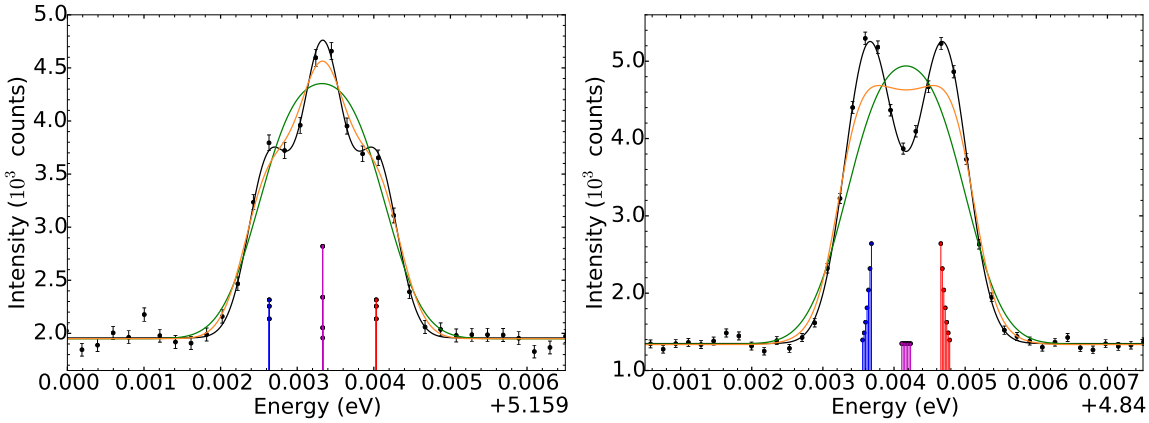

(a) $^1G_4$-$^1F_3^o$ (b) $^3F_3$-$^1F_3^o$

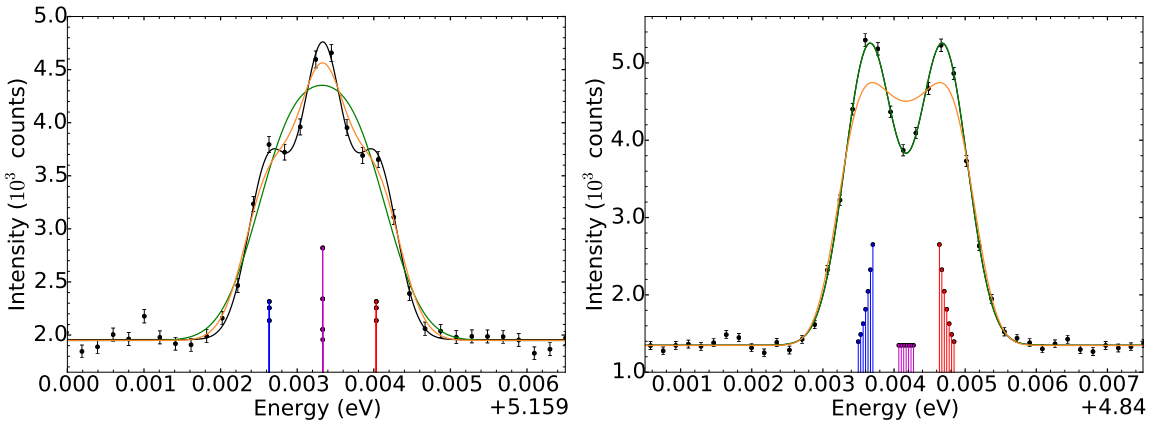

(c) $^1G_4$-$^3F_3^o$ (d) $^3F_3$-$^3F_3^o$

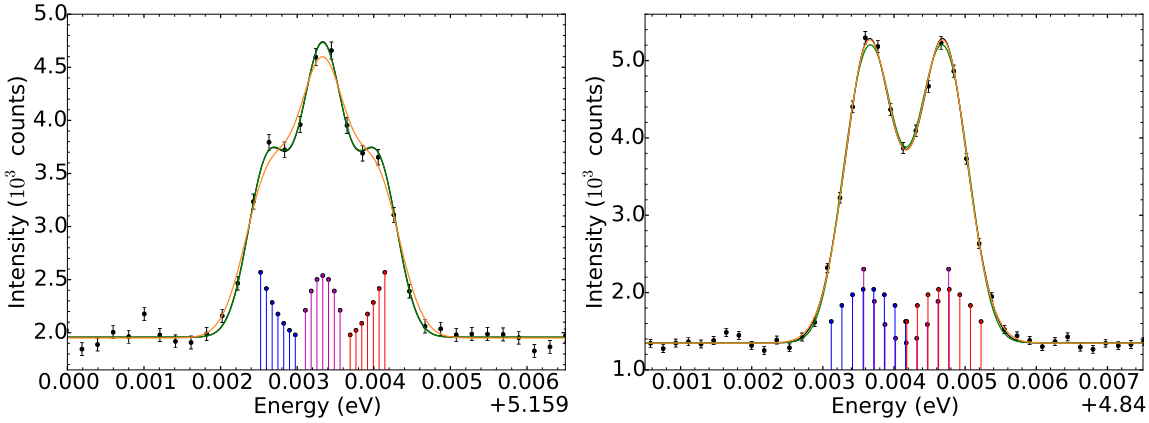

(e) $^1G_4$-$^3F_4^o$ (f) $^3F_3$-$^3F_4^o$

Fig. 6.11 Fits for the proposed identifications of the lines at approximately 5.162 33(2) eV (left) and 4.844 170(6) eV (right). Each spectral line was fitted with the Zeeman model where all the parameters were kept free (black line), with a fixed width (orange), and with fixed g_j-factors (green). The individual Zeeman components $\Delta m = +1$ (blue), $\Delta m = 0$ (magenta), and $\Delta m = -1$ (red) are shown for the black fit. Detailed fit results are given in table 6.7.

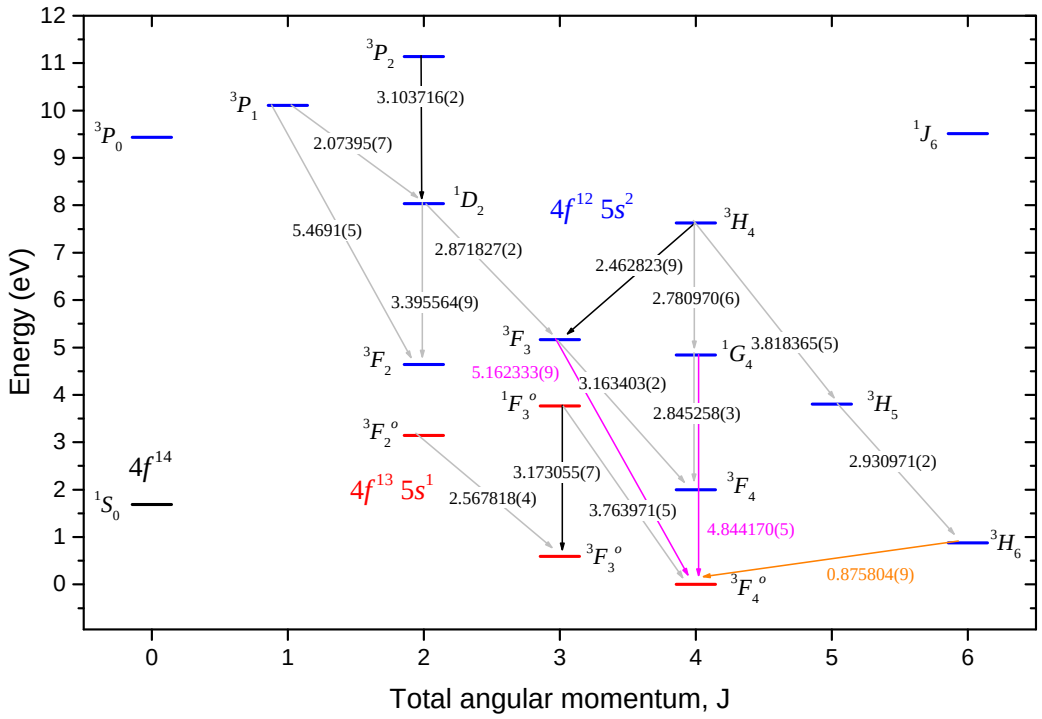

Fig. 6.12 Grotrian level diagram of the $4f^{14}$, $4f^{13}5s^1$ and $4f^{12}5s^2$ configurations of Ir^{17+} based on our current understanding of this HCI. The black arrows indicate M1 transitions that were identified; magenta arrows indicate tentatively identified E1 lines, and the orange arrow indicates the inferred M2/E3 clock transition. Gray arrows indicate transitions previously identified in the work of Windberger *et al.* All the transition energies are indicate in eV. The positions of unconnected fine-structure levels such as $^1J_6$ are based on FSCC calculations.

6.5 CRM predictions

Comparison of the tentative identification of the E1 lines to table 6.5 shows that the FAC predictions for the E1 lines differ by approximately 2 eV. Hence, those results for the energies of the fine-structure levels can not be used for CRM calculations of transitions between the $4f^{13}5s^1$ and $4f^{12}5s^2$ configurations. However, FAC provides the possibility to modify the calculated energies with user-defined values. Thus, all the energies of the levels connected by identified transitions were adapted to correspond to the measurements. The energies of levels of the $4f^{14}$ and $4f^{12}5s^2$ configurations that were not known were adjusted to the values predicted by FSCC calculations. For the $4f^{13}5p^1$, $4f^{12}5s^15p^1$, and $4f^{11}5s^25p^1$ configurations the energies as calculated with FAC were kept. Based on these energies for the fine-structure levels, the transition rates and electron impact excitation cross sections were calculated. The CRM calculations were performed as described in section 4.6. The results for the predicted line strengths of the transitions in the three configurations are illustrated in Fig. 6.13. According to the predictions, the two brightest optical E1 lines are those that were tentatively identified in the previous section. The next brightest line is predicted to be the $^1G_4 - {}^3F_3^o$ transition at approximately 290.6 nm with half the strength of the brightest E1 lines. No matching line was measured, so that the identifications remain tentative. Stronger transitions between the $4f^{13}5s^1$ and $4f^{12}5s^2$ configurations are predicted to take place for wavelengths between 100 and 200 nm. Unfortunately, during this work, a spectrometer for that range was not available.

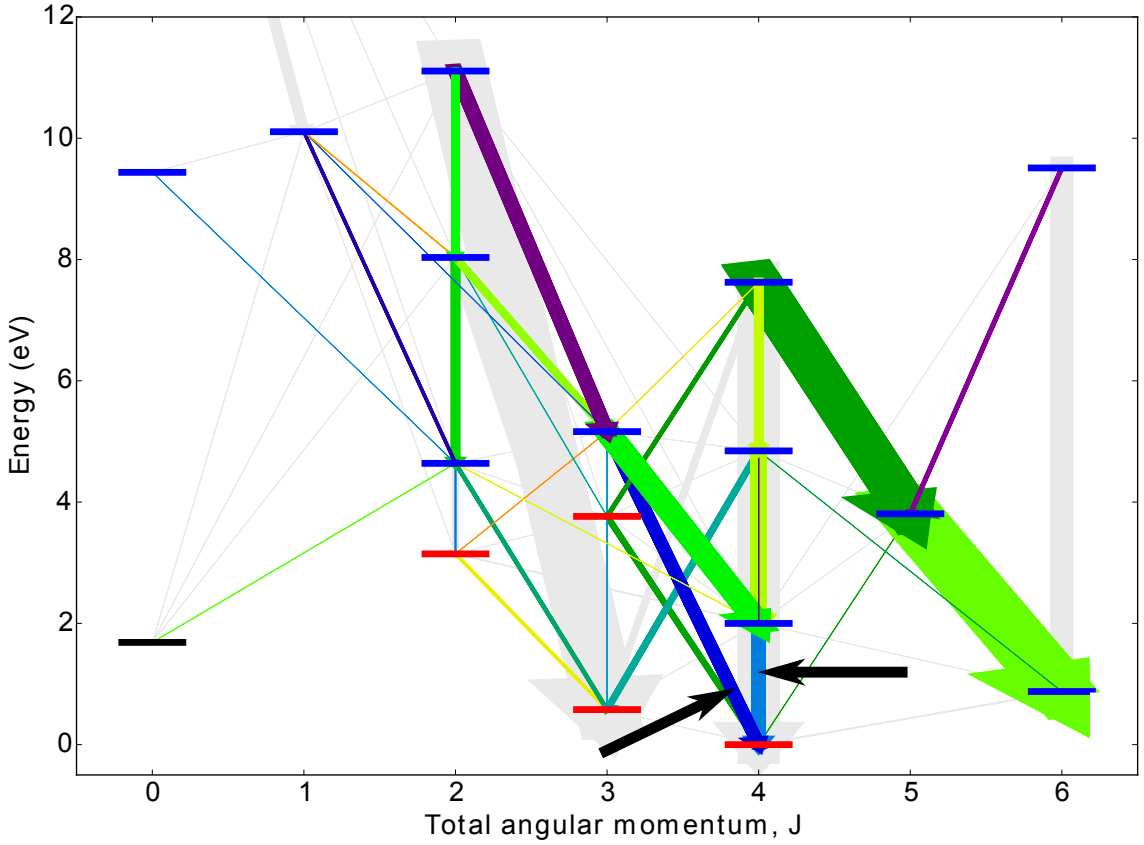

Fig. 6.13 Grotrian level diagram of Ir^{17+} highlighting the transitions (colored arrows) of the $4f^{14}$, $4f^{13}5s^1$, and $4f^{12}5s^2$ configurations. The colors of the arrows are based on the mapping of the optical spectrum to the range of 200 nm to 700 nm, transitions outside this range are shown in gray. The thickness of each arrow indicates the strength of the line as predicted by CRM calculations. The black arrows indicate the two strongest E1 transitions. The strongest transitions have Einstein coefficients for spontaneous emission in the order of$A_{fi} \backsimeq 500\text{s}^{-1}$. Level designations are as in Fig. 6.12.

Chapter 7

Summary and outlook

Currently, the most advanced frequency standards (clocks) based on a single ion reach fractional uncertainties at the level of $\Delta\nu/\nu_0 \approx 10^{-17}$. A large part of the uncertainty of these devices is due to the sensitivity of the energy levels of ions to external electric and magnetic fields. Therefore, it was proposed to use transitions of highly charged ions (HCI) in frequency standards. Due to their compact size, the sensitivity of HCI to external perturbations is highly suppressed [35]. An abundance of suitable HCI has been proposed during recent years. In almost all of these, the required optical transitions exist as a result of level crossings of two or more configurations [27, 36, 40]. The accuracy of predictions for the electronic structure of these HCI is limited due to the intricate electron-electron correlations inherent to these complex many-electron systems. On the experimental side, measurements of the spectra of HCI near level crossings are lacking. Thus, the wavelengths of the HCI clock transitions are not known to high enough precision for laser spectroscopy, a prerequisite for the implementation as a frequency standard.

A prime application of frequency standards is the search for variations of fundamental constants. The single most stringent laboratory test of variation of constants up to date was performed on the fine-structure constant α. By measuring the ratio of the wavelengths of two transitions with different sensitivities to the variation of α several times over the course of approximately a year, the variation was determined to be $\Delta\alpha = -1.6(2.3)10^{-17}/\mathrm{yr}$. Due to increased relativistic effects, fine-structure energy levels of HCI can have an increased sensitivity to $\Delta\alpha$. For electrons in nearly filled orbitals, such as near the $4f$–$5s$ level crossing, these effects can be even more enhanced [27]. Hence, Nd-like Ir^{17+} has transitions that belong to the most $\Delta\alpha$-sensitive transitions predicted. Until recently, no spectroscopic data was available for Ir^{17+} . The work by Windberger *et al.* changed that, 11 optical transitions of Ir^{17+} were identified [34]. These were all magnetic dipole (M1) transitions, taking place within a given configuration. Several of the measured yet unidentified lines

were suggested to be electric dipole (E1) transitions that take place between the $4f^{13}5s^1$ and $4f^{12}5s^2$ configurations. These have the highest known sensitivity to $\Delta\alpha$ in a stable atomic system, hence, knowledge of their wavelengths is imperative for the use of Ir^{17+} as a detector of $\Delta\alpha$. Unfortunately, the uncertainties of the measured wavelengths precluded an ultimate identification of the suggested lines.

Already in the year 1980, Curtis and Ellis made a theoretical study of the $4f$–$5s$ level crossing [46]. They predicted that for Pm-like ions with atomic numbers $Z \geq 74$ the electronic structure is alkalilike, i.e. it consists of a single valence electron above closed shells. These systems feature $5s$–$5p$ transitions in the extreme ultraviolet (EUV) range that were predicted to be prominent enough to be useful for plasma diagnostics. Despite considerable effort from several experimental groups to measure the predicted $5s$–$5p$ transitions, no definitive identifications had been made [119, 121, 122]. Many of the identifications were impeded by the dense spectra and the uncertainties of predictions at the level of 1%.

In this work, Re, Os, Ir, and Pt ($Z = 75 - 78$) ions of the Pr-like, Nd-like, and Pm-like charge states were experimentally investigated in the optical and EUV range. The HCI were produced and trapped in the Heidelberg electron beam ion trap (HD-EBIT). In an EBIT, the mono-energetic electron beam ionizes atoms sequentially to the desired charge state, hence a well-defined charge-state distribution of the ions can be obtained. The electron beam excites the trapped HCI by electron impact. The subsequent fluorescence light was recorded by two spectrometers. With the EUV spectrometer spectra of Pr-like, Nd-like, and Pm-like Re, Os, Ir, and Pt were obtained. For the optical spectrometer procedures were developed to measure weak lines. These were applied to search and measure candidates for interconfiguration transitions of Ir^{17+} .

Despite the predicted abundance of strong near-ground-state transitions of the Pm-like ions in the EUV regime, the measured spectra contained relatively few lines. To interpret the EUV spectra, modeling of the electron-ion interactions in the EBIT proved necessary. The employed collisional radiative model (CRM) accounted for electron impact excitation and de-excitation, and for spontaneous decay of the fine-structure levels. By solving the quasi-stationary-state rate equations, the populations of the levels, and the line strengths at the prevailing experimental conditions could be predicted. It was concluded that the spectrum was dominated by $4f^{13}5s^15p^1 - 4f^{13}5s^2$ transitions, leading to the identification of several of these lines. The $4f^{12}5p^1_{3/2} - 4f^{12}5s^1$ transitions, although appearing weak, could be identified in Re^{14+}, Os^{15+}, Ir^{16+}, and Pt^{17+}. Comparison to several predictions based on advanced configuration interaction and relativistic many-body perturbation calculations showed discrepancies at the level of 1% [123, 72]. Considering the low strength of the $5s$–$5p$

line, the transition seems unsuitable for diagnostics of plasmas at the conditions prevailing during the performed measurements.

The interpretation of the EUV spectrum of Nd-like Ir^{17+} was also guided by CRM calculations. Transitions from the $4f^{13}5p^1$ to the $4f^{13}5s^1$ configurations and from the $4f^{12}5s^15p^1$ to the $4f^{12}5s^2$ configurations were identified. Predictions based on Fock-space coupled cluster calculations showed an average discrepancy of 0.5%, which is relatively large compared to the 0.1% agreement that was obtained for optical Ir^{17+} transitions [34]. However, those transitions were within a given configuration, while the here identified EUV lines take place between different configurations. The results indicate that the theoretical uncertainties of the energies of interconfiguration transitions is rather large.

Several regions of interest in the optical spectrum of Ir^{17+} were selected for intensive study. The two regions around approximately 503 nm and 395 nm were studied with the aim of measuring previously unidentified M1 transitions. The wavelength of the $^3H_4$–$^3F_3$ transition in the $4f^{12}5s^2$ configuration could actually directly be inferred from the identifications made in the work by Windberger *et al.*. However, it was previously not observed due to its low transition rate, which was calculated to be approximately 11 s^{-1}. In the new data, a weak line with a transition energy of 2.462 823(9) eV was measured, which is in excellent agreement with the inferred value. In the work of Windberger *et al.* it was shown that the FSCC predictions for the M1 lines on average deviated only 0.03 eV from the measurements. These predictions were used as a guide for finding the remaining optical M1 lines. The $^1F_3^o - {}^3F_3^o$ transition was identified by its characteristic line shape caused by the Zeeman splitting of the fine-structure levels in the 8.00 T magnetic field of the EBIT. The measured transition energy of 3.173 055(7) eV is in excellent agreement with the FSCC predictions considering the theoretical uncertainty. The identification of this transition fixes the energy of all the fine-structure levels of the $4f^{13}5s^1$ ground-state configuration with respect to each other. The $^3P_2 - {}^1D_2$ transition was also measured to be in excellent agreement with FSCC predictions at 3.103 716(2) eV. With this, all the M1 transitions of the three lowest energy configurations in Ir^{17+} that were predicted to be in the optical range were finally identified.

The significant uncertainties of predictions for the energy splitting ΔE between the $4f^{13}5s^1$ and $4f^{12}5s^2$ configurations precluded a targeted search for individual interconfiguration transitions. Of 24 possible interconfiguration E1 transitions, only a small subset can be in the optical range. Which transitions those are depends on ΔE. However, for a broad range of ΔE, the strongest transitions were predicted to be in the ultraviolet range. Therefore, the region from approximately 230 nm to 330 nm was investigated for weak lines. This region also contained the lines that were previously suggested as E1 candidates by Windberger *et al.*. Based on the combined new and old data, a list of wavelengths of yet unidentified lines

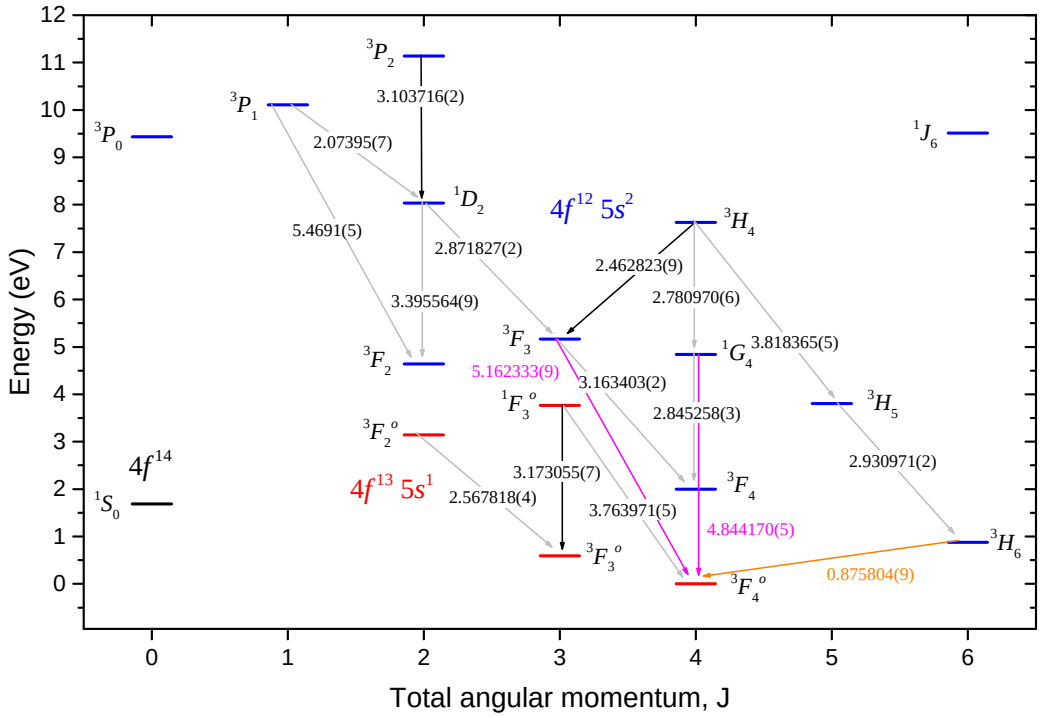

Fig. 7.1 Grotrian level diagram of the $4f^{14}$, $4f^{13}5s^1$ and $4f^{12}5s^2$ configurations of Ir^{17+} based on our current understanding of this HCI. The black arrows indicate M1 transitions that were identified; magenta arrows indicate tentatively identified E1 lines, and the orange arrow indicates the inferred M2/E3 clock transition. Gray arrows indicate transitions previously identified in the work of Windberger *et al.* All the transition energies are indicate in eV. The positions of unconnected fine-structure levels such as $^1J_6$ are based on FSCC calculations.

was produced. This was compared to predicted E1 transition energies over a ΔE range of 7.5 eV. In this manner, a number of identifications of lines were suggested. Each suggestion was checked against two criteria: the predicted strength of the line had to be sufficient to be observable with the employed setup, and the line shape had to correspond to a model based on the Zeeman splitting of the involved levels. Ultimately, the $4f^{12}5s^2\ ^1G_4$–$4f^{13}5s^1\ ^3F_4^o$ and $4f^{12}5s^2\ ^3F_3$–$4f^{13}5s^1\ ^3F_4^o$ transitions at respectively 5.162 333(9) eV and 4.844 170(5) eV could be tentatively identified. Due to discrepancies of approximately 2 to 3.5 eV between the measurements and the available predictions for ΔE, a definitive identification is not claimed in this work. However, based on the tentative identifications, the sought-after energy of the M2/E3 $4f^{12}5s^2\ ^3H_6$–$4f^{13}5s^1\ ^3F_4^o$ transition can be inferred to be 0.875 804(9) eV. An overview of the optical Ir^{17+} transitions identified in this work is shown in Fig. 7.1.

To improve our knowledge of the Ir^{17+} electronic configuration, several follow-up measurements can be performed. For example, the lifetimes and branching ratios of the $4f^{12}5s^2\ ^3F_3$ and $4f^{12}5s^2\ ^1G_4$ levels can be measurement in a similar fashion as was done

for the $1s^2 2s^2 2p^2 P^o_{3/2}$ level of Ar^{13+} [92]. This information would be valuable for state preparation in direct laser spectroscopy experiments. Furthermore, a spectrometer sensitive in the 20–200 nm range can be employed to search for the predicted strong $4f^{12}5s^2 - 4f^{13}5s^1$ transitions, so that the tentative identifications of the E1 transitions made in this work can be confirmed or refuted. The recent demonstration of trapping and cooling of Ar^{13+} in a cryogenic Paul trap paves the way for future precision laser spectroscopy of HCI [150]. The Ar^{13+} ions were trapped and sympathetically cooled with Be^+, so that the Ar^{13+} ions reached temperatures well below 300 mK. Co-trapping of an Ir^{17+} ion with a Be^+ ion would lend itself perfectly for quantum logic spectroscopy [151]. The Be^+ ion would serve as the so-called logic ion for the cooling, state preparation, and state detection of the Ir^{17+} ion. With such a scheme, a frequency standard with a fractional uncertainty of potentially 10^{-19} and a high sensitivity to α variation is conceivable.

Acknowledgements

My decision to do my PhD work at the Max-Planck-Institut für Kernphysik (MPIK) was not only based on the excellent physics programs and the exciting laboratories, but also on its members. The kindness of the people that I met on my first visit in 2012 set the tone for the following years. First and foremost I would like to thank José and Klaus for welcoming me to the MPIK, taking the time for me if necessary, and for the great working environment. I'm also very thankful for the responsibilities and freedoms that I was given during the past years. The day to day life in the laboratory was brightened thanks to José's unstoppable passion, wealth of knowledge, and Spanish congeniality.

It was Oscar who first suggested that I go to Heidelberg for a PhD, an idea which I'm still thankful for. Together with Alex we spend hours upon hours at the HD-EBIT, discussing results and how to obtain even better ones. Despite the tensions inherent to these discussions and the stress induced by malfunctioning equipment, we always managed to keep things civilized; if necessary, by going for a drink or two. In this way, I learned a lot from you about optics, atomic physics, statistics, and more. Thank you for the great time, both at work and outside of work.

The past and present EBIT group members that I've worked with are too numerous to each thank by name. From the outside the EBIT group may seem like a dysfunctional family, but the amount of camaraderie and knowledge in the group is amazing. Big projects and problems were made manageable thanks to inventive ideas and selfless lending of hands. These qualities make you more than just colleagues to me. A special thanks to all the bachelor and master students with whom I have worked. Their relentless questions kept me on my toes, and their enthusiasm made dull jobs exciting.

Working with people outside the EBIT group broadened my horizon. The Penning trappers were always willing to explain the finer details of mass spectrometry and g-factor measurements. Their interest in my work made me feel appreciated and their questions helped me improve my presentations. Hopefully soon, we will be able to work together more closely at Pentatrap and Alphatrap. My experience in physics was further expanded by participating in experiments of Nina Rohringer, Stanislav Taschenov, and Elias Sideras-Haddad.

Implementing improvements to the setups and performing repairs when necessary was greatly accelerated thanks to the skilled MPIK technical staff. Whether it involved machining of complex parts, re-organizing electrical systems, software issues, radiation safety, and the list goes on; there was always someone with the skills to help out. Mutual respect and interest in each others work greatly enhanced the working climate.

As the saying goes, all work and no play makes Jack a dull boy. I was fortunate enough to work in an environment where the line between work and play is thin. However, to occasionally truly disconnect from work, I was lucky to find good friends in Heidelberg. Without them, I would not have seen so much of Heidelberg and its beautiful surroundings. Without them I would not have learned so much about the German language, culture, and history. And without them I would have probably spend way more time than is good for me in the laboratory.

I also want to thank all my friends and family in the Netherlands. My parents for encouraging me to move abroad, for accepting my sometimes lacking communication, and for their wonderful visits. Thanks to Doaitse and Agnes for giving me the laptop on which I have done almost all of the data analysis, and on which I have written this thesis. Thanks to all the friends who have kept in touch and who still open their doors to me on the rare occasions that I'm back near Groningen.

And finally, my thanks to Alex, Chintan, José, Sven, and Zoltán for proof reading this thesis and making suggestions where necessary.

With the hopes of continuing in the same phenomenal way, I thank you all,

Hendrik

Heidelberg, April 2016

References

[1] J. C. Dean *Popular Astronomy*, vol. 19, p. 21, 1911.

[2] ATLAS Collaboration, "Observation of a new boson at a mass of 125 gev with the cms experiment at the lhc," *Physics Letters B*, vol. 716, no. 1, pp. 30 – 61, 2012.

[3] CMS Collaboration, "Observation of a new particle in the search for the standard model higgs boson with the atlas detector at the lhc," *Physics Letters B*, vol. 716, no. 1, pp. 1 – 29, 2012.

[4] R. Oerter, *The Theory of Almost Everything: The Standard Model, the Unsung Triumph of Modern Physics*. Penguin Publishing Group, 2006.

[5] P. A. M. Dirac, "The Cosmological Constants.,"

[6] E. Teller, "On the change of physical constants," *Phys. Rev.*, vol. 73, pp. 801–802, Apr 1948.

[7] G. Gamow, "Electricity, gravity, and cosmology," *Phys. Rev. Lett.*, vol. 19, pp. 759–761, Sep 1967.

[8] J.-P. Uzan, "The fundamental constants and their variation: observational and theoretical status," *Rev. Mod. Phys.*, vol. 75, pp. 403–455, Apr 2003.

[9] J. Barrow, "Varying constants," *Philosophical Transactions of the Royal Society of London A: Mathematical, Physical and Engineering Sciences*, vol. 363, no. 1834, pp. 2139–2153, 2005.

[10] C. J. A. P. Martins, "Fundamental cosmology in the e-elt era: the status and future role of tests of fundamental coupling stability," *General Relativity and Gravitation*, vol. 47, no. 1, pp. 1–19, 2014.

[11] Wikpedia, MissMJ. https://en.wikipedia.org/wiki/File:Standard_Model_of_Elementary_Particles.svg. [Retrieved on 13-03-2016].

[12] A. Sommerfeld, "Zur quantentheorie der spektrallinien," *Annalen der Physik*, vol. 356, no. 17, pp. 1–94, 1916.

[13] B. N. T. Peter J. Mohr, David B. Newell, "CODATA Recommended Values of the Fundamental Physical Constants: 2014," 2014.

[14] B. Bloom, T. Nicholson, J. Williams, S. Campbell, M. Bishof, X. Zhang, W. Zhang, S. Bromley, and J. Ye, "An optical lattice clock with accuracy and stability at the 10-18 level," *Nature*, vol. 506, no. 7486, pp. 71–75, 2014.

[15] N. Huntemann, B. Lipphardt, C. Tamm, V. Gerginov, S. Weyers, and E. Peik, "Improved limit on a temporal variation of m_p/m_e from comparisons of yb^+ and cs atomic clocks," *Phys. Rev. Lett.*, vol. 113, p. 210802, Nov 2014.

[16] A. D. Ludlow, M. M. Boyd, J. Ye, E. Peik, and P. O. Schmidt, "Optical atomic clocks," *Rev. Mod. Phys.*, vol. 87, pp. 637–701, Jun 2015.

[17] T. Rosenband, D. B. Hume, P. O. Schmidt, C. W. Chou, A. Brusch, L. Lorini, W. H. Oskay, R. E. Drullinger, T. M. Fortier, J. E. Stalnaker, S. A. Diddams, W. C. Swann, N. R. Newbury, W. M. Itano, D. J. Wineland, and J. C. Bergquist, "Frequency ratio of al+ and hg+ single-ion optical clocks; metrology at the 17th decimal place," *Science*, vol. 319, no. 5871, pp. 1808–1812, 2008.

[18] J. C. Berengut, V. A. Dzuba, V. V. Flambaum, and A. Ong, "Optical Transitions in Highly Charged Californium Ions with High Sensitivity to Variation of the Fine-Structure Constant," *Phys. Rev. Lett.*, vol. 109, p. 070802, Aug 2012.

[19] C. Tamm, N. Huntemann, B. Lipphardt, V. Gerginov, N. Nemitz, M. Kazda, S. Weyers, and E. Peik, "Cs-based optical frequency measurement using cross-linked optical and microwave oscillators," *Phys. Rev. A*, vol. 89, p. 023820, Feb 2014.

[20] R. Le Targat, L. Lorini, Y. Le Coq, M. Zawada, J. Guéna, M. Abgrall, M. Gurov, P. Rosenbusch, D. Rovera, B. Nagórny, *et al.*, "Experimental realization of an optical second with strontium lattice clocks," *Nature communications*, vol. 4, 2013.

[21] T. M. Fortier, N. Ashby, J. C. Bergquist, M. J. Delaney, S. A. Diddams, T. P. Heavner, L. Hollberg, W. M. Itano, S. R. Jefferts, K. Kim, F. Levi, L. Lorini, W. H. Oskay, T. E. Parker, J. Shirley, and J. E. Stalnaker, "Precision atomic spectroscopy for improved limits on variation of the fine structure constant and local position invariance," *Phys. Rev. Lett.*, vol. 98, p. 070801, Feb 2007.

[22] N. Leefer, C. T. M. Weber, A. Cingöz, J. R. Torgerson, and D. Budker, "New limits on variation of the fine-structure constant using atomic dysprosium," *Phys. Rev. Lett.*, vol. 111, p. 060801, Aug 2013.

[23] J. K. Webb, V. V. Flambaum, C. W. Churchill, M. J. Drinkwater, and J. D. Barrow, "Search for time variation of the fine structure constant," *Physical Review Letters*, vol. 82, no. 5, p. 884, 1999.

[24] J. K. Webb, M. Murphy, V. Flambaum, V. Dzuba, J. Barrow, C. Churchill, J. Prochaska, and A. Wolfe, "Further evidence for cosmological evolution of the fine structure constant," *Physical Review Letters*, vol. 87, no. 9, p. 091301, 2001.

[25] J. Webb, J. King, M. Murphy, V. Flambaum, R. Carswell, and M. Bainbridge, "Indications of a spatial variation of the fine structure constant," *Physical Review Letters*, vol. 107, no. 19, p. 191101, 2011.

[26] J. A. King, J. K. Webb, M. T. Murphy, V. V. Flambaum, R. F. Carswell, M. B. Bainbridge, M. R. Wilczynska, and F. E. Koch, "Spatial variation in the fine-structure constant – new results from VLT/UVES," *Monthly Notices of the Royal Astronomical Society*, vol. 422, no. 4, pp. 3370–3414, 2012.

[27] J. C. Berengut, V. A. Dzuba, V. V. Flambaum, and A. Ong, "Electron-Hole Transitions in Multiply Charged Ions for Precision Laser Spectroscopy and Searching for Variations in α," *Phys. Rev. Lett.*, vol. 106, p. 210802, May 2011.

[28] J. B. Whitmore and M. T. Murphy, "Impact of instrumental systematic errors on fine-structure constant measurements with quasar spectra," *Monthly Notices of the Royal Astronomical Society*, vol. 447, no. 1, pp. 446–462, 2015.

[29] A. Pinho and C. Martins, "Updated constraints on spatial variations of the fine-structure constant," *Physics Letters B*, vol. 756, pp. 121 – 125, 2016.

[30] J.-P. Uzan, "Varying constants, gravitation and cosmology," *Living Rev. Relativity*, vol. 14, no. 2, 2011.

[31] International Bureau of Weights and Measures. http://www.bipm.org/en/publications/si-brochure/second.html. [Retrieved on 14-03-2016].

[32] P. Gill, "Optical frequency standards," *Metrologia*, vol. 42, no. 3, p. S125, 2005.

[33] J. Ye and S. Cundiff, *Femtosecond Optical Frequency Comb: Principle, Operation and Applications*. Springer US, 2006.

[34] A. Windberger, J. R. Crespo López-Urrutia, H. Bekker, N. S. Oreshkina, J. C. Berengut, V. Bock, A. Borschevsky, V. A. Dzuba, E. Eliav, Z. Harman, U. Kaldor, S. Kaul, U. I. Safronova, V. V. Flambaum, C. H. Keitel, P. O. Schmidt, J. Ullrich, and O. O. Versolato, "Identification of the Predicted $5s$-$4f$ Level Crossing Optical Lines with Applications to Metrology and Searches for the Variation of Fundamental Constants," *Phys. Rev. Lett.*, vol. 114, p. 150801, Apr 2015.

[35] S. Schiller, "Hydrogenlike Highly Charged Ions for Tests of the Time Independence of Fundamental Constants," *Phys. Rev. Lett.*, vol. 98, p. 180801, Apr 2007.

[36] M. S. Safronova, V. A. Dzuba, V. V. Flambaum, U. I. Safronova, S. G. Porsev, and M. G. Kozlov, "Highly Charged Ions for Atomic Clocks, Quantum Information, and Search for α variation," *Phys. Rev. Lett.*, vol. 113, p. 030801, Jul 2014.

[37] A. Derevianko, V. A. Dzuba, and V. V. Flambaum, "Highly Charged Ions as a Basis of Optical Atomic Clockwork of Exceptional Accuracy," *Phys. Rev. Lett.*, vol. 109, p. 180801, Oct 2012.

[38] V. A. Dzuba, A. Derevianko, and V. V. Flambaum, "Ion clock and search for the variation of the fine-structure constant using optical transitions in Nd^{13+} and Sm^{15+}," *Phys. Rev. A*, vol. 86, p. 054502, Nov 2012.

[39] A. Kramida, Yu. Ralchenko, J. Reader, and and NIST ASD Team. NIST Atomic Spectra Database (ver. 5.3), [Online]. Available:`http://physics.nist.gov/asd` .National Institute of Standards and Technology,Gaithersburg, MD. [Retrieved on 15-02-2016].

[40] V. A. Dzuba and V. V. Flambaum, "Highly charged ions for atomic clocks and search for variation of the fine structure constant," *Hyperfine Interactions*, vol. 236, no. 1, pp. 79–86, 2015.

[41] V. A. Dzuba, V. V. Flambaum, and J. K. Webb, "Calculations of the relativistic effects in many-electron atoms and space-time variation of fundamental constants," *Phys. Rev. A*, vol. 59, pp. 230–237, Jan 1999.

[42] J. C. Berengut, V. A. Dzuba, and V. V. Flambaum, "Enhanced laboratory sensitivity to variation of the fine-structure constant using highly charged ions," *Phys. Rev. Lett.*, vol. 105, p. 120801, Sep 2010.

[43] P. Beiersdorfer, E. Träbert, G. V. Brown, J. Clementson, D. B. Thorn, M. H. Chen, K. T. Cheng, and J. Sapirstein, "Hyperfine Splitting of the $2s_{1/2}$ and $2p_{1/2}$ Levels in Li- and Be-like Ions of $^{141}_{59}$Pr," *Phys. Rev. Lett.*, vol. 112, p. 233003, Jun 2014.

[44] J. D. Gillaspy, D. Osin, Y. Ralchenko, J. Reader, and S. A. Blundell, "Transition energies of the *D* lines in Na-like ions," *Phys. Rev. A*, vol. 87, p. 062503, Jun 2013.

[45] D. Kilbane, G. O'Sullivan, J. D. Gillaspy, Y. Ralchenko, and J. Reader, "EUV spectra of Rb-like to Cu-like gadolinium ions in an electron-beam ion trap," *Phys. Rev. A*, vol. 86, p. 042503, Oct 2012.

[46] L. J. Curtis and D. G. Ellis, "Alkalilike Spectra in the Promethium Isoelectronic Sequence," *Phys. Rev. Lett.*, vol. 45, pp. 2099–2102, Dec 1980.

[47] C. Foot, *Atomic physics*. Oxford master series in physics, Oxford University Press, 2005.

[48] R. Liboff, *Introductory Quantum Mechanics*. Addison-Wesley, 2003.

[49] A. Corney, *Atomic and Laser Spectroscopy*. Oxford Classic Texts in the Physical Sciences, Oxford University Press, 2006.

[50] J. Bjorken and S. Drell, *Relativistic quantum mechanics*. International series in pure and applied physics, McGraw-Hill, 1964.

[51] P. A. M. Dirac, "The Quantum Theory of the Electron," *Proceedings of the Royal Society of London A: Mathematical, Physical and Engineering Sciences*, vol. 117, no. 778, pp. 610–624, 1928.

[52] J. R. Crespo López-Urrutia, P. Beiersdorfer, K. Widmann, B. B. Birkett, A.-M. Mårtensson-Pendrill, and M. G. H. Gustavsson, "Nuclear magnetization distribution radii determined by hyperfine transitions in the 1*s* level of H-like ions ^{185}Re^{74+} and ^{187}Re^{74+}," *Phys. Rev. A*, vol. 57, pp. 879–887, Feb 1998.

[53] S. Kebrich, "Feinstruktur, Hyperfeinstuktur und Zeeman-Aufspaltung des titanartigen Re^{53+} im optischen Bereich," Bachelor's Thesis, Ruprecht-Karls-Universität Heidelberg, 2015.

[54] J. Emsley, *The Elements*. Oxford chemistry guides, Clarendon Press, 1998.

[55] K. A. Olive *et al.*, "Review of Particle Physics," *Chin. Phys.*, vol. C38, p. 090001, 2014.

[56] P. Zeeman, "The Effect of Magnetisation on the Nature of Light Emitted by a Substance," *Nature*, vol. 55, p. 347, Feb. 1897.

[57] J. D, *Classical Electrodynamics*. John Wiley, 1975.

[58] W. Lotz, "An empirical formula for the electron-impact ionization cross-section," *Zeitschrift für Physik*, vol. 206, no. 2, pp. 205–211.

[59] K. L. Wong, M. J. May, P. Beiersdorfer, K. B. Fournier, B. Wilson, G. V. Brown, P. Springer, P. A. Neill, and C. L. Harris, "Determination of the charge state distribution of a highly ionized coronal au plasma," *Phys. Rev. Lett.*, vol. 90, p. 235001, Jun 2003.

[60] H. Beyer and V. Shevelko, *Introduction to the Physics of Highly Charged Ions*. Series in Atomic Molecular Physics, Taylor & Francis, 2002.

[61] W. Quint and M. Vogel, *Fundamental Physics in Particle Traps*. Springer Tracts in Modern Physics, Springer Berlin Heidelberg, 2014.

[62] H. van Regemorter, "Rate of Collisional Excitation in Stellar Atmospheres,"

[63] S. W. Epp, J. R. C. López-Urrutia, G. Brenner, V. Mäckel, P. H. Mokler, R. Treusch, M. Kuhlmann, M. V. Yurkov, J. Feldhaus, J. R. Schneider, M. Wellhöfer, M. Martins, W. Wurth, and J. Ullrich, "Soft X-Ray Laser Spectroscopy on Trapped Highly Charged Ions at FLASH," *Phys. Rev. Lett.*, vol. 98, p. 183001, May 2007.

[64] P. Beiersdorfer, "Laboratory x-ray astrophysics," *Annual Review of Astronomy and Astrophysics*, vol. 41, no. 1, pp. 343–390, 2003.

[65] D. Hollain, "Vermessung vom hochgeladenen Iridium mithilfe eines neuen Kontrollsystems," Master's Thesis, Ruprecht-Karls-Universität Heidelberg, 2014.

[66] M. F. Gu, "The flexible atomic code," *Canadian Journal of Physics*, vol. 86, no. 5, pp. 675–689, 2008.

[67] S. B. Hansen, K. B. Fournier, A. Y. Faenov, A. I. Magunov, T. A. Pikuz, I. Y. Skobelev, Y. Fukuda, Y. Akahane, M. Aoyama, N. Inoue, H. Ueda, and K. Yamakawa, "Measurement of $2l$-nl' x-ray transitions from ≈ 1 μm Kr clusters irradiated by high-intensity femtosecond laser pulses," *Phys. Rev. E*, vol. 71, p. 016408, Jan 2005.

[68] M. F. Gu, P. Beiersdorfer, G. V. Brown, H. Chen, D. B. Thorn, and S. M. Kahn, "Wavelength Measurements of Ni L-Shell Lines between 9 and 15 Å," *The Astrophysical Journal*, vol. 657, no. 2, p. 1172, 2007.

[69] G. Breit, "Dirac's Equation and the Spin-Spin Interactions of Two Electrons," *Phys. Rev.*, vol. 39, pp. 616–624, Feb 1932.

[70] I. I. Tupitsyn, V. M. Shabaev, J. R. Crespo López-Urrutia, I. Draganić, R. Soria Orts, and J. Ullrich, "Relativistic calculations of isotope shifts in highly charged ions," *Phys. Rev. A*, vol. 68, p. 022511, 2003.

[71] I. I. Tupitsyn, A. V. Volotka, D. A. Glazov, V. M. Shabaev, G. Plunien, J. R. Crespo López-Urrutia, A. Lapierre, and J. Ullrich, "Magnetic-dipole transition probabilities in B-like and Be-like ions," *Phys. Rev. A*, vol. 72, p. 062503, Dec 2005.

[72] N. S. Oreshkina. Private communication, May 2014.

[73] R. J. Bartlett and M. Musiał, "Coupled-cluster theory in quantum chemistry," *Rev. Mod. Phys.*, vol. 79, pp. 291–352, Feb 2007.

[74] E. Eliav, U. Kaldor, and Y. Ishikawa, "Open-shell relativistic coupled-cluster method with dirac-fock-breit wave functions: Energies of the gold atom and its cation," *Phys. Rev. A*, vol. 49, pp. 1724–1729, Mar 1994.

[75] Y. Ishikawa, H. M. Quiney, and G. L. Malli, "Dirac-fock-breit self-consistent-field method: Gaussian basis-set calculations on many-electron atoms," *Phys. Rev. A*, vol. 43, pp. 3270–3278, Apr 1991.

[76] D. R. Bates, A. E. Kingston, and R. W. P. McWhirter, "Recombination between electrons and atomic ions. i. optically thin plasmas," *Proceedings of the Royal Society of London A: Mathematical, Physical and Engineering Sciences*, vol. 267, no. 1330, pp. 297–312, 1962.

[77] R. K. Smith, N. S. Brickhouse, D. A. Liedahl, and J. C. Raymond, "Collisional Plasma Models with APEC/APED: Emission-Line Diagnostics of Hydrogen-like and Helium-like Ions," *The Astrophysical Journal Letters*, vol. 556, no. 2, p. L91, 2001.

[78] M. J. May, K. B. Fournier, P. Beiersdorfer, H. Chen, and K. L. Wong, "X-ray spectral measurements and collisional radiative modeling of Ni- to Kr-like Au ions in electron beam ion trap plasmas," *Phys. Rev. E*, vol. 68, p. 036402, Sep 2003.

[79] Y. Kobayashi, D. Kato, H. A. Sakaue, I. Murakami, and N. Nakamura, "Spectroscopic study of promethiumlike bismuth with an electron-beam ion trap: Search for alkali-metal-like resonance lines," *Phys. Rev. A*, vol. 89, p. 010501, Jan 2014.

[80] M. F. Gu, "Indirect X-Ray Line-Formation Processes in Iron L-Shell Ions," *The Astrophysical Journal*, vol. 582, no. 2, p. 1241, 2003.

[81] A. Einstein, "Zur Quantentheorie der Strahlung," *Physikalische Zeitschrift*, vol. 18, 1917.

[82] Y. Ralchenko, *Modern Methods in Collisional-Radiative Modeling of Plasmas*. Springer Series on Atomic, Optical, and Plasma Physics, Springer International Publishing, 2016.

[83] M. A. Levine, R. E. Marrs, J. R. Henderson, D. A. Knapp, and M. B. Schneider, "The Electron Beam Ion Trap: A New Instrument for Atomic Physics Measurements," *Physica Scripta*, vol. 1988, no. T22, p. 157, 1988.

[84] V. Smirnov, "Tokamak foundation in USSR/Russia 1950–1990," *Nuclear Fusion*, vol. 50, no. 1, p. 014003, 2010.

[85] L. Spitzer, "The Stellarator Concept," *Physics of Fluids*, vol. 1, no. 4, 1958.

[86] W. Quint, J. Dilling, S. Djekic, H. Häffner, N. Hermanspahn, H.-J. Kluge, G. Marx, R. Moore, D. Rodriguez, J. Schönfelder, G. Sikler, T. Valenzuela, J. Verdú, C. Weber, and G. Werth, "HITRAP: A Facility for Experiments with Trapped Highly Charged Ions," *Hyperfine Interactions*, vol. 132, no. 1, pp. 453–457.

[87] R. Geller, "Highly charged ECR ion sources: Summary and comments (invited)," *Review of Scientific Instruments*, vol. 61, no. 1, 1990.

[88] H. Postma, "Multiply charged heavy ions produced by energetic plasmas," *Physics Letters A*, vol. 31, no. 4, pp. 196 – 197, 1970.

[89] J. R. Crespo López-Urrutia, A. Dorn, R. Moshammer, and J. Ullrich, "The Freiburg Electron Beam Ion Trap/Source Project FreEBIT," *Physica Scripta*, vol. 1999, no. T80B, p. 502, 1999.

[90] J. R. Crespo López-Urrutia, J. Braun, G. Brenner, H. Bruhns, C. Dimopoulou, I. N. Draganić, D. Fischer, A. J. González Martínez, A. Lapierre, V. Mironov, R. Moshammer, R. Soria Orts, H. Tawara, M. Trinczek, and J. Ullrich, "Progress at the Heidelberg EBIT," *Journal of Physics: Conference Series*, vol. 2, no. 1, p. 42, 2004.

[91] A. J. González Martínez, J. R. Crespo López-Urrutia, D. Fischer, R. Soria Orts, and J. Ullrich, "The Heidelberg EBIT: Present Results and Future Perspectives," *Journal of Physics: Conference Series*, vol. 72, no. 1, p. 012001, 2007.

[92] A. Lapierre, U. D. Jentschura, J. R. Crespo López-Urrutia, J. Braun, G. Brenner, H. Bruhns, D. Fischer, A. J. González Martínez, Z. Harman, W. R. Johnson, C. H. Keitel, V. Mironov, C. J. Osborne, G. Sikler, R. Soria Orts, V. Shabaev, H. Tawara, I. I. Tupitsyn, J. Ullrich, and A. Volotka, "Relativistic electron correlation, quantum electrodynamics, and the lifetime of the $1s^2 2s^2 2p\ ^2p^o_{3/2}$ level in boronlike argon," *Phys. Rev. Lett.*, vol. 95, p. 183001, Oct 2005.

[93] J. Cronin, "Modern dispenser cathodes," *Solid-State and Electron Devices, IEE Proceedings I*, vol. 128, pp. 19–32, February 1981.

[94] D. Meeker. http://www.femm.info/wiki/HomePage. [Retrieved on 16-03-2016].

[95] J. R. Pierce, "Rectilinear Electron Flow in Beams," *Journal of Applied Physics*, vol. 11, no. 8, 1940.

[96] G. Herrmann, "Optical theory of thermal velocity effects in cylindrical electron beams," *Journal of Applied Physics*, vol. 29, no. 2, 1958.

[97] D. Knapp, R. Marrs, S. Elliott, E. Magee, and R. Zasadzinski, ""a high-energy electron beam ion trap for production of high-charge high-z ions"," *Nuclear Instruments and Methods in Physics Research Section A: Accelerators, Spectrometers, Detectors and Associated Equipment*, vol. 334, no. 2, pp. 305 – 312, 1993.

[98] S. Utter, P. Beiersdorfer, J. R. Crespo López-Urrutia, and K. Widmann, "Position and size of the electron beam in the high-energy electron beam ion trap," *Nuclear Instruments and Methods in Physics Research Section A: Accelerators, Spectrometers, Detectors and Associated Equipment*, vol. 428, no. 2, pp. 276–283, 1999.

[99] J. Gillaspy, Y. Aglitskiy, E. Bell, C. Brown, C. Chantler, R. Deslattes, U. Feldman, L. Hudson, J. Laming, E. Meyer, *et al.*, "Overview of the electron beam ion trap program at nist," *Physica Scripta*, vol. 1995, no. T59, p. 392, 1995.

[100] G. Y. Liang, J. R. Crespo López-Urrutia, T. M. Baumann, S. W. Epp, A. Gonchar, A. Lapierre, P. H. Mokler, M. C. Simon, H. Tawara, V. Mäckel, K. Yao, G. Zhao, Y. Zou, and J. Ullrich, "Experimental Investigations of Ion Charge Distributions, Effective Electron Densities, and Electron-Ion Cloud Overlap in Electron Beam Ion Trap Plasma Using Extreme-Ultraviolet Spectroscopy," *The Astrophysical Journal*, vol. 702, no. 2, p. 838, 2009.

[101] S. W. Epp, *Röntgen-Laserspektroskopie hochgeladener Ionen in einer EBIT am Freie-Elektronen-Laser FLASH*. PhD thesis, Ruprecht-Karls-Universität Heidelberg, 2005.

[102] R. E. Marrs, S. R. Elliott, and D. A. Knapp, "Production and trapping of hydrogenlike and bare uranium ions in an electron beam ion trap," *Phys. Rev. Lett.*, vol. 72, pp. 4082–4085, Jun 1994.

[103] P. Beiersdorfer, V. Decaux, S. R. Elliott, K. Widmann, and K. Wong, "Temperature of the ions produced and trapped in an electron-beam ion trap," *Review of Scientific Instruments*, vol. 66, no. 1, 1995.

[104] V. Mäckel, R. Klawitter, G. Brenner, J. R. Crespo López-Urrutia, and J. Ullrich, "Laser Spectroscopy on Forbidden Transitions in Trapped Highly Charged Ar^{13+} Ions," *Phys. Rev. Lett.*, vol. 107, p. 143002, Sep 2011.

[105] C. Yamada, K. Nagata, N. Nakamura, S. Ohtani, S. Takahashi, T. Tobiyama, M. Tona, H. Watanabe, N. Yoshiyasu, M. Sakurai, A. P. Kavanagh, and F. J. Currell, "Injection of metallic elements into an electron-beam ion trap using a Knudsen cell," *Review of Scientific Instruments*, vol. 77, no. 6, 2006.

[106] G. E. Holland, C. N. Boyer, J. F. Seely, J. Tan, J. Pomeroy, and J. Gillaspy, "Low jitter metal vapor vacuum arc ion source for electron beam ion trap injections," *Review of scientific instruments*, vol. 76, no. 7, p. 073304, 2005.

[107] M. Trinczek, A. Werdich, V. Mironov, P. Guo, A. J. González Martínez, J. Braun, J. R. Crespo López-Urrutia, and J. Ullrich, "A laser ion source for an electron beam ion trap," *Nuclear Instruments and Methods in Physics Research Section B: Beam Interactions with Materials and Atoms*, vol. 251, no. 1, pp. 289–296, 2006.

[108] S. Elliott and R. Marrs, "A wire probe as an ion source for an electron beam ion trap," *Nuclear Instruments and Methods in Physics Research Section B: Beam Interactions with Materials and Atoms*, vol. 100, no. 4, pp. 529–535, 1995.

[109] Strem Chemicals, Inc., "Volatile Organometallics." http://www.strem.com/catalog/family/Volatile+Organometallics+for+CVD+%26+ALD/. [Retrieved on 08-02-2016].

[110] K. Kromer, "Rekombinationsprozesse in hochgeladenem Bismut uns Praseodym," Bachelor's Thesis, Ruprecht-Karls-Universität Heidelberg, 2015.

[111] E. Hecht, *Optics*. Addison-Wesley, 2002.

[112] W. S. Boyle and G. E. Smith, "Charge coupled semiconductor devices," *Bell System Technical Journal*, vol. 49, no. 4, pp. 587–593, 1970.

[113] "Nobel prize in Physics 2009." http://www.nobelprize.org/nobel_prizes/physics/laureates/2009/press.html. [Retrieved on 06-02-2016].

[114] R. Aymar, P. Barabaschi, and Y. Shimomura, "The ITER design," *Plasma Physics and Controlled Fusion*, vol. 44, no. 5, p. 519, 2002.

[115] T. Klinger, C. Baylard, C. Beidler, J. Boscary, H. Bosch, A. Dinklage, D. Hartmann, P. Helander, H. Maßberg, A. Peacock, T. Pedersen, T. Rummel, F. Schauer, L. Wegener, and R. Wolf, "Towards assembly completion and preparation of experimental campaigns of Wendelstein 7-X in the perspective of a path to a stellarator fusion power plant," *Fusion Engineering and Design*, vol. 88, no. 6–8, pp. 461 – 465, 2013. Proceedings of the 27th Symposium On Fusion Technology (SOFT-27); Liège, Belgium, September 24-28, 2012.

[116] I. Hutchinson, *Principles of Plasma Diagnostics*. Cambridge University Press, 2002.

[117] R. Isler, R. Neidigh, and R. Cowan, "Tungsten radiation from tokamak-produced plasmas," *Physics Letters A*, vol. 63, no. 3, pp. 295 – 297, 1977.

[118] C. Biedermann, R. Radtke, R. Seidel, and T. Pütterich, "Spectroscopy of highly charged tungsten ions relevant to fusion plasmas," *Physica Scripta*, vol. 2009, no. T134, p. 014026, 2009.

[119] E. Träbert and P. Heckmann, "Tentative identification of the 5s-5p transitions in Pm I-like Au XIX," *Zeitschrift für Physik D Atoms, Molecules and Clusters*, vol. 1, no. 4, pp. 381–383, 1986.

[120] K. B. Fournier, M. Finkenthal, S. Lippmann, C. P. Holmes, H. W. Moos, W. H. Goldstein, and A. L. Osterheld, "$n = 5$ to $n = 5$ soft-x-ray emission of uranium in a high-temperature low-density tokamak plasma," *Phys. Rev. A*, vol. 50, pp. 3727–3733, Nov 1994.

[121] R. Hutton, Y. Zou, J. R. Almandos, C. Biedermann, R. Radtke, A. Greier, and R. Neu, "EBIT spectroscopy of Pm-like tungsten," *Nuclear Instruments and Methods in Physics Research Section B: Beam Interactions with Materials and Atoms*, vol. 205, no. 0, pp. 114 – 118, 2003. 11th International Conference on the Physics of Highly Charged Ions.

[122] M. J. Vilkas, Y. Ishikawa, and E. Träbert, "Electric-dipole $5s$-$5p$ transitions in promethiumlike ions," *Phys. Rev. A*, vol. 77, p. 042510, Apr 2008.

[123] U. I. Safronova, A. S. Safronova, and P. Beiersdorfer, "Contribution of the $4f$-core-excited states in determination of atomic properties in the promethium isoelectronic sequence," *Phys. Rev. A*, vol. 88, p. 032512, Sep 2013.

[124] U. I. Safronova, V. V. Flambaum, and M. S. Safronova, "Transitions between the $4f$-core-excited states in Ir^{16+}, Ir^{17+}, and Ir^{18+} ions for clock applications," vol. 92, p. 022501, Aug. 2015.

[125] T. M. Baumann, "Entwicklung eines Gitterspektrometers zur Untersuchung vakuumultravioletter Strahlung von hochgeladenen Ionen," Diplomarbeit, Ruprecht-Karls-Universität Heidelberg, 2008.

[126] J. A. R. Samson, *Techniques of Vacuum Ultraviolet Spectroscopy*. Lincoln, Nebraska: Pied Publications, 1967.

[127] T. Harada and T. Kita, "Mechanically ruled aberration-corrected concave gratings," *Appl. Opt.*, vol. 19, pp. 3987–3993, Dec 1980.

[128] T. Harada, K. Takahashi, H. Sakuma, and A. Osyczka, "Optimum design of a grazing-incidence flat-field spectrograph with a spherical varied-line-space grating," *Appl. Opt.*, vol. 38, pp. 2743–2748, May 1999.

[129] D. L. Windt, W. C. Cash, M. Scott, P. Arendt, B. Newnam, R. F. Fisher, and A. B. Swartzlander, "Optical constants for thin films of Ti, Zr, Nb, Mo, Ru, Rh, Pd, Ag, Hf, Ta, W, Re, Ir, Os, Pt, and Au from 24 Å to 1216 Å," *Appl. Opt.*, vol. 27, pp. 246–278, Jan 1988.

[130] A. Windberger, *Identification of optical transitions in complex highly charged ions for applications in metrology and tests of fundamental constants*. PhD thesis, Ruprecht-Karls-Universität Heidelberg, 2015.

[131] R. Schupp, "Spektroskopische Untersuchung von Ir^{17+}," Bachelor's Thesis, Ruprecht-Karls-Universität Heidelberg, 2008.

[132] O. Jitrik and C. F. Bunge, "Transition Probabilities for Hydrogen-Like Atoms," *J. Phys. Chem. Ref. Data*, vol. 33, p. 1059, 2004.

[133] J. Scofield, "Ionisation Energies," *LLNL internal report*, 1975.

[134] T. A. Carlson, C. N. Jr., N. Wasserman, and J. Mcdowell, "Calculated ionization potentials for multiply charged ions," *Atomic Data and Nuclear Data Tables*, vol. 2, no. 0, pp. 63 – 99, 1970.

[135] LIGO Scientific Collaboration and Virgo Collaboration, "Observation of Gravitational Waves from a Binary Black Hole Merger," *Phys. Rev. Lett.*, vol. 116, p. 061102, Feb 2016.

[136] R. Soria Orts, *Isotopic effect in B-like and Be-like argon ions*. PhD thesis, Ruprecht-Karls-Universität Heidelberg, 2005.

[137] R. Klawitter, "Resonant laser spectroscopy of a visible magnetic dipole transition in Ar^{13+}," Diplomarbeit, Ruprecht-Karls-Universität Heidelberg, 2009.

[138] M. A. Blessenohl, "Optische Spektroskopie an hochgeladenen Bismut-Ionen und Konstruktion eines hochauflösenden VUV-Gitterspektrometers," Master's thesis, Ruprecht-Karls-Universität Heidelberg, 2015.

[139] M. Czerny and A. F. Turner, "Über den Astigmatismus bei Spiegelspektrometern," *Zeitschrift für Physik*, vol. 61, no. 11, p. 792–797.

[140] Princeton Instruments, "Spectroscopy Cameras." http://www.princetoninstruments.com/products/speccam/pixis/dsheet.aspx. [Retrieved on 17-01-2016].

[141] Horiba Scientific, "Blazed Holographic Plane Gratings." http://www.horiba.com/us/en/scientific/products/diffraction-gratings/for-industrial-applications/blazed-holographic-plane-gratings/grating-list/. [Retrieved on 24-01-2016].

[142] W. Pych, "A Fast Algorithm for Cosmic-Ray Removal from Single Images," *Publications of the Astronomical Society of the Pacific*, vol. 116, no. 816, pp. 148–153, 2004.

[143] A. Z. Bonanos, K. Z. Stanek, R. P. Kudritzki, L. M. Macri, D. D. Sasselov, J. Kaluzny, P. B. Stetson, D. Bersier, F. Bresolin, T. Matheson, B. J. Mochejska, N. Przybilla, A. H. Szentgyorgyi, J. Tonry, and G. Torres, "The First DIRECT Distance Determination to a Detached Eclipsing Binary in M33," *The Astrophysical Journal*, vol. 652, no. 1, p. 313, 2006.

[144] W. Whaling, W. Anderson, M. Carle, J. Brault, and H. Zarem, "Argon ion linelist and level energies in the hollow-cathode discharge," *Journal of Quantitative Spectroscopy and Radiative Transfer*, vol. 53, no. 1, pp. 1 – 22, 1995.

[145] I. G. Nave, S. Johansson, R. C. M. Learner, A. P. Thorne, and J. W. Brault, "A New Multiplet Table for Fe," 1994.

[146] B. Edlén, "The refractive index of air," *Metrologia*, vol. 2, no. 2, p. 71, 1966.

[147] E. R. Peck and K. Reeder, "Dispersion of air," *J. Opt. Soc. Am.*, vol. 62, pp. 958–962, Aug 1972.

[148] N. S. Oreshkina. Private communication, November 2015.

[149] J. C. Berengut. Private communication, December 2014.

[150] L. Schmöger, O. O. Versolato, M. Schwarz, M. Kohnen, A. Windberger, B. Piest, S. Feuchtenbeiner, J. Pedregosa-Gutierrez, T. Leopold, P. Micke, A. K. Hansen, T. M. Baumann, M. Drewsen, J. Ullrich, P. O. Schmidt, and J. R. Crespo López-Urrutia, "Coulomb crystallization of highly charged ions," *Science*, vol. 347, no. 6227, pp. 1233–1236, 2015.

[151] P. O. Schmidt, T. Rosenband, C. Langer, W. M. Itano, J. C. Bergquist, and D. J. Wineland, "Spectroscopy using quantum logic," *Science*, vol. 309, no. 5735, pp. 749–752, 2005.

Appendix A

Predicted E1 line shapes

There are 24 possibly optical E1 transitions between the $4f^{13}5s^1$ and $4f^{12}5s^2$ configurations. Due to the 8.00 T magnetic field strength at the trap center, the line shapes of the transitions is determined mainly by the Zeeman splitting of lines, refer to chapter 2. In this appendix, the predicted line shapes of the 24 E1 transitions are shown. The predictions were based on the g_j-factors as calculated by Berengut [34, 149]. The lines were assumed to have a width of $25 \cdot 10^{-5}$ eV, which corresponds to the resolving power of the employed optical spectrometer at approximately 260 nm, 4.75 eV.

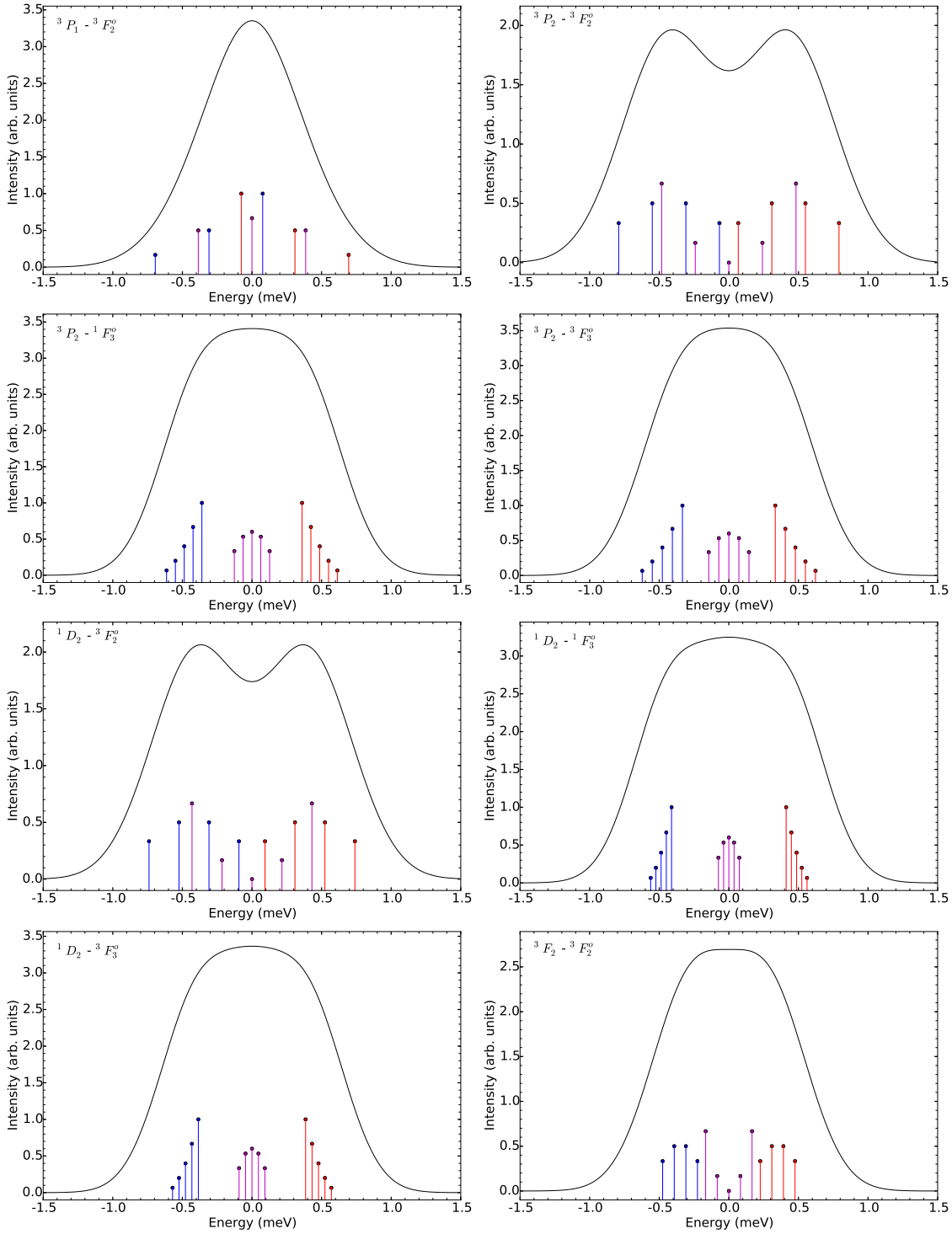

Fig. A.1 Refer to the introduction of this appendix for details.

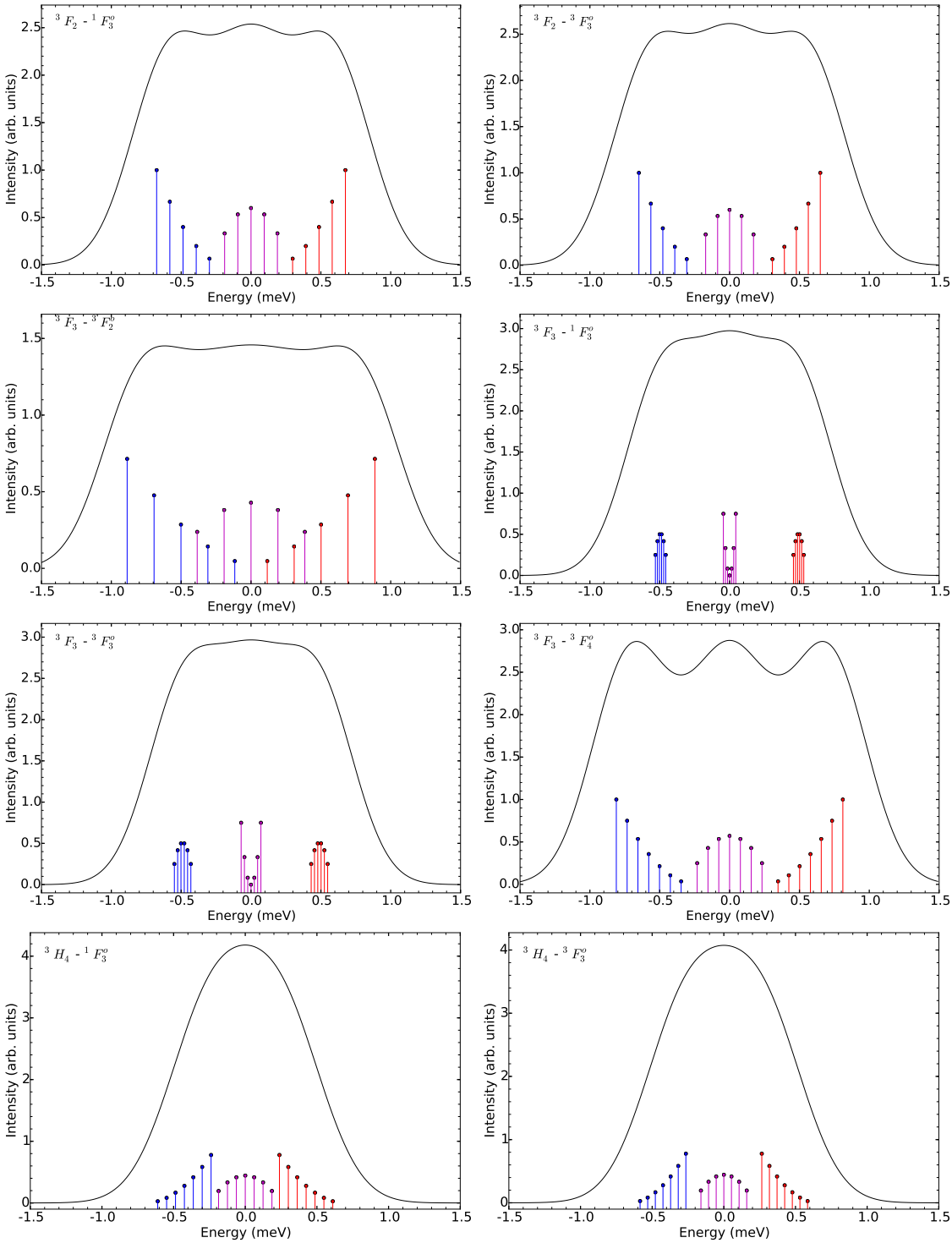

Fig. A.2 Refer to the introduction of this appendix for details.

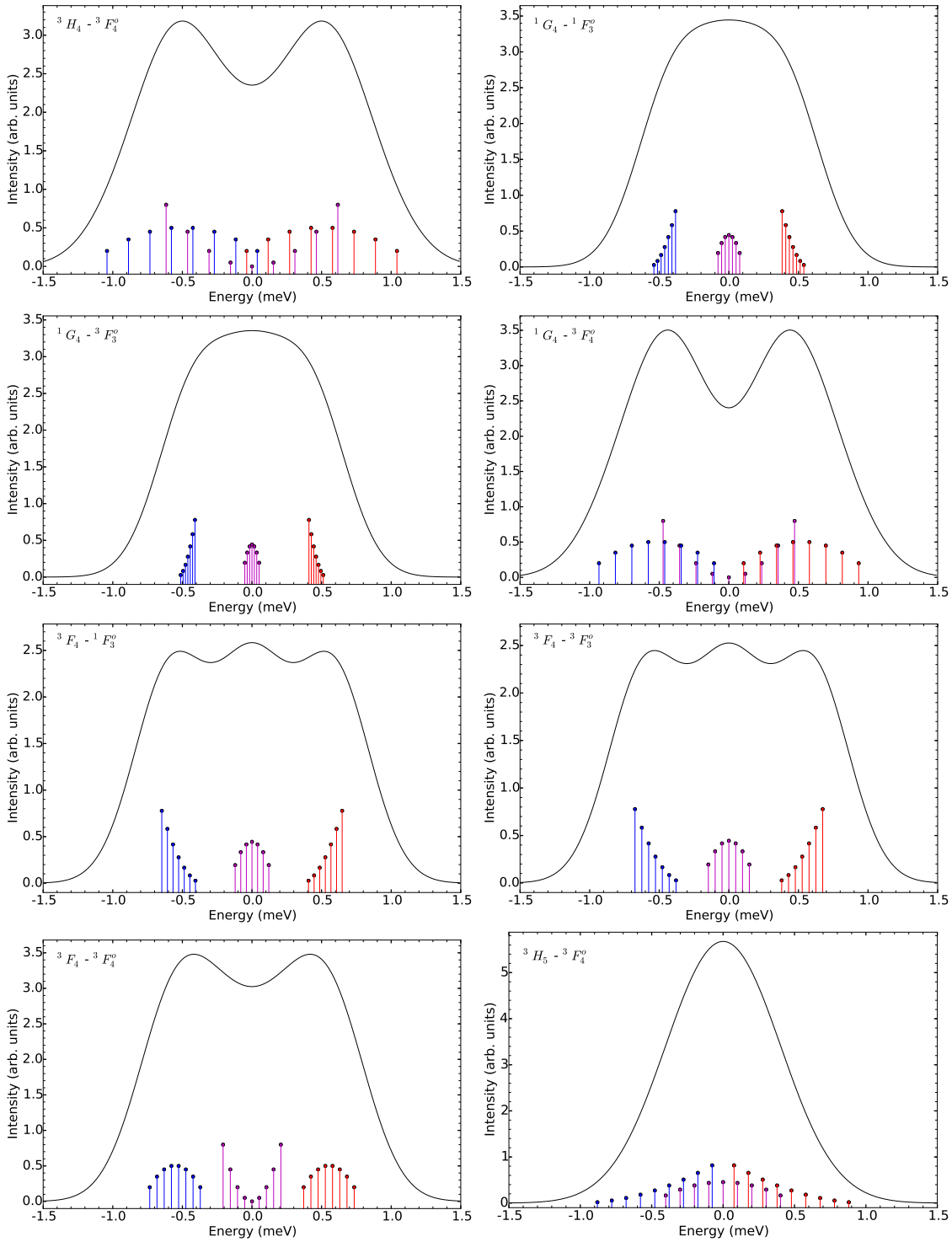

Fig. A.3 Refer to the introduction of this appendix for details.

Appendix B

FAC and CRM example scripts

The following three scripts can be employed to produce a synthetic spectrum of Ir^{17+} in the EUV range. In the first script the atomic structure calculations are performed using the flexible atomic code (FAC) libraries [66]. The second script uses the collisional radiative model (CRM) to solve the rate equations. The third and final script takes the resulting data and produces the synthetic spectrum.

B.1 Calculation of energy levels, tranition rates, and excitation cross-sections

```
from pfac import fac

# Select the chemical element, and thereby nuclear charge of
    ↪ the particle
fac.SetAtom('Ir')
# Define which shells are closed, i.e. inactive
fac.Closed('1s', '2s', '2p', '3s', '3p', '3d', '4s', '4p', '
    ↪ 4d')

# Variable to help loop over all the possible transitions
maxn = 6

# Define active configurations
fac.Config('n1', '4f13 5s1')
fac.Config('n2', '4f14')
```

```
fac.Config('n3', '4f13 5p1')
fac.Config('n4', '4f12 5s2')
fac.Config('n5', '4f12 5s1 5p1')
fac.Config('n6', '4f11 5s2 5p1')

# Determine the optimal radial potential
fac.ConfigEnergy(0)
fac.OptimizeRadial('n1')
fac.ConfigEnergy(1)

# To fix the energy of levels, uncomment the following line
    ↪ and provide a suitable list of corrections
# fac.CorrectEnergy('corrections2b', 0)

# Calculate and save the fine-structure level energies
fac.Structure('Ir17plus_bin.en', ['n1', 'n2', 'n3','n4','n5'
    ↪ ,'n6'])
fac.MemENTable('Ir17plus_bin.en')
fac.PrintTable('Ir17plus_bin.en', 'Ir17plus.en')

# Calculate and save the transition rates
for n in range(1, maxn):
  for m in range(n, maxn):
    # With the -1 the multipole type is selcted, E1 in this
        ↪ case
    fac.TRTable('Ir17plus_bin.tr', ['n' + str(n)], ['n' +
        ↪ str(m)], -1)
fac.PrintTable('Ir17plus_bin.tr', 'Ir17plus.tr')

# Calculate and save the electron impact cross sections
for n in range(1, maxn):
  for m in range(n, maxn):
    fac.CETable('Ir17plus_bin.ce', ['n' + str(n)],['n' + str
        ↪ (m)])
fac.PrintTable('Ir17plus_bin.ce', 'Ir17plus.ce')
```

B.2 Collisional radiative model

```
from pfac import fac
from pfac.crm import *

# Select which ions are included in the CRM calculation
AddIon(60, 1.0, 'Ir17plus_bin')

# 1: if <0 only transition within 17+ are connected, 2: data filenames (default extension automatically added)
SetBlocks(-1, 'Ir17plus_bin')
Print('blocks set')

# Set properties of the electron beam
# 1: gaussian electron energy distribution, 2: electron beam energy in eV, 3: energy spread in eV, 4 and 5: Emin and Emax
SetEleDist(1, 440, 5, 435, 445)

# Photon rates. 0 means: take only pontaneous decay into acount
SetTRRates(0)

# Collisional transition rates. If 1: include both collisional excitation and de- excitation. If 0: only excitation
SetCERates(1)

# Set the electron density in units of 1e10 cm^-3
SetEleDensity(100)

# Solve the coupled differential equations
InitBlocks()
SetIteration(1e-6, 0.5, 2048)

# Determine the level populations and save the data
```

```
LevelPopulation()
SpecTable('Ir17plus_bin.sp', 0)
PrintTable('Ir17plus_bin.sp', 'Ir17plus.sp')
```

B.3 Generation of a synthetic spectrum

```
from pfac.crm import *
from pfac import fac
import sys, os

# Make sure that the files for saving the data are removed
os.system('rm Ir17plus.pl')
os.system('rm Ir17plus.ln')

# Set the line type, 0 means all the lines are included
t = 0

# Set the spectral range in eV
emin = 40
emax = 120

# Set the intensity threshold for lines to be included
eps = 1e-6

# Creates synthetic spectrum by convolving lines with
    ↪ gaussians of width 0.1 eV
PlotSpec('Ir17plus_bin.sp', 'Ir17plus.pl', 60, t, emin, emax
    ↪ , 0.1, eps)

# Save a list with information on the lines in the spectral
    ↪ range
SelectLines('Ir17plus_bin.sp', 'Ir17plus.ln', 60, 0, emin,
    ↪ emax)
```

Appendix C

EUV lines of Nd-like and Pr-like Re, Os, Ir, and Pt

Table C.1 Catalog of the measured EUV lines in the Nd-like charge state, the wavelengths λ are given in nm. The uncertainty on the wavelengths were determined by the square-root of the sum of squares of the fit uncertainty and the calibrations uncertainty. The relative intensities (I) have been corrected for the theoretical efficiency of the spectrometer and are estimated to be accurate at the 10%-level. Note though that the Re spectra were taken at a lower electron beam current, see table 4.2. The upper part of the table shows characteristic lines that appear in the spectra of multiple elements. The lower part of the table shows lines that were fitted, but could not be identified. The superscript ^{b} denotes that the line might be blended with another line that could have influenced the wavelength and intensity determination.

Rhenium (15+)		Osmium (16+)		Iridium (17+)		Platinum (18+)	
λ	I	λ	I	λ	I	λ	I
21.8806(14)	10	20.4908(6)	50	19.2222(12)^b	72	18.0577(12)	25
21.9791(14)	7	20.5784(12)	18	19.3077(11)	14	18.1260(19)	4
22.1233(15)	6	20.7049(8)	28	19.4073(10)	43	18.2158(13)	10
22.1881(15)	7	20.7747(8)	25	19.4833(10)	23	18.2926(17)^b	4
22.2842(16)	7	20.8641(13)	18	19.5715(10)^b	28	18.3760(15)^b	7
22.3383(14)	10	20.9150(7)	51	19.6169(8)^b	76	18.4202(11)^b	27
22.4355(14)	11	20.9842(7)	40	19.6644(9)^b	54	18.4587(12)^b	20
23.8470(13)	3	22.2555(6)	18	20.7598(10)^b	35	19.4388(11)	15
19.5132(9)	4	20.3205(7)^b	5	19.7126(12)^b	24	17.4065(35)^b	2
20.2455(12)	2	22.0679(7)	8	19.97271(11)^b	3	17.4480(21)^b	2
21.5208(16)^b	3	20.1619(6)	11	20.02634(9)^b	5	17.8016(15)	5
21.8173(14)	2			20.14692(9)^b	6	18.5065(18)^b	5
23.4568(13)	5			20.36168(17)^b	6	19.2595(10)	6
24.1822(14)	1			20.48496(8)^b	7	19.4855(92)^b	4
24.2392(14)	1			20.56433(7)^b	15	19.5187(27)	4
25.3592(14)	4			20.65508(13)	3	20.3559(13)	2
				20.80929(30)^b	35	20.4566(13)	2
				20.84504(23)	8		
				20.94853(17)	12		
				21.02527(10)	1		
				21.08258(10)	3		
				21.14316(15)^b	4		
				21.5879(8)	2		
				21.7671(8)	6		
				21.8674(9)	5		

Table C.2 Line catalog of the measured EUV lines in the Pr-like charge state. The units, experimental parameters, and superscripts are as in the previous table, table C.1

Rhenium (16+)		Osmium (17+)		Iridium (18+)		Platinum (19+)	
λ	I	λ	I	λ	I	λ	I
21.2100(14)	3	19.8872(57)	5	18.6139(12)	5		
21.3748(49)	3	20.0099(6)	19	18.7721(11)	19	17.7004(18)	3
21.4356(16)	5	20.0881(13)	9	18.8464(17)	10	17.7647(19)^b	3
21.5352(14)	6	20.1960(12)^b	21	18.9727(10)	24	17.8359(16)	5
23.2713(15)	1					19.0457(14)^b	4
23.3687(44)^b	1	21.5673(7)	7	20.1944(10)	9	18.9278(11)^b	3
20.9267(13)	1	19.8534(33)	5	18.3031(16)	5	17.3203(19)	3
21.1162(17)	1	21.2194(8)	5	18.4125(13)	6	17.4185(20)^b	3
21.2810(32)	2	21.4400(6)	23	18.7040(25)	5	17.9683(25)^b	2
21.3390(86)^b	3			18.9209(13)	16	18.5767(14)^b	3
21.6463(100)^b	1			19.0634(27)	5	18.6587(14)	2
21.6782(17)	1			19.1202(21)	7	18.8364(9)	14
21.7282(15)	2			19.8957(14)	9	19.9889(24)	1
21.7710(15)^b	1			20.0852(10)	32		
22.9315(14)	2						
22.9866(14)	1						
23.1143(17)^b	1						

Erklärung:

Ich versichere, dass ich diese Arbeit selbstständig verfasst und keine anderen als die angegebenen Quellen und Hilfsmittel benutzt habe.

Heidelberg, den ....

Hendrik Bekker